A New Measurement of the Fusion Reaction $^{14}N(p,\gamma)^{15}O$ and Its Impact On Hydrogen Burning, Globular Clusters, and the Age of the Universe

by

Robert Charles Runkle

A dissertation submitted to the faculty of the University of North Carolina at Chapel Hill in partial fulfillment of the requirements for the degree of Doctor of Philosophy in the Department of Physics & Astronomy.

Chapel Hill

2003

Approved by:

Advisor: A. Champagne

Reader: C. Iliadis

Reader: H. Karwowski

ABSTRACT

A New Measurement of the Fusion Reaction $^{14}N(p,\gamma)^{15}O$ and Its Impact On Hydrogen Burning, Globular Cluster Ages, and the Age of the Universe

(Under the Direction of Professor Art Champagne)

Stars create the light we observe from energy liberated by nuclear fusion reactions. For most of their lives, stars exist as main-sequence objects quiescently burning hydrogen. At temperatures present in stars slightly larger than the Sun, the CN cycle dominates hydrogen burning and thus a star's macroscopic properties such as luminosity and main sequence turn-off. Because it is the slowest step in the CN cycle, the $^{14}N(p,\gamma)^{15}O$ reaction dictates the rate of hydrogen burning. This fact mandates a good understanding of the $^{14}N(p,\gamma)^{15}O$ reaction rate. Although this reaction is well understood at high energies, there are large uncertainties at astrophysically relevant energies. We conducted a new measurement of the $^{14}N(p,\gamma)^{15}O$ low energy cross section that extends very close to temperatures present in massive stars. The previous uncertainty in the reaction rate resulted from the possible contribution of a sub-threshold resonance in the ground state transition. Our measurement suggests that this resonance does not contribute significantly. We conclude that the 6793 keV state in ^{15}O dominates the low energy cross section. Indirect measurements support our extrapolation of this state to very low energies, which results in a factor of two reduction in the reaction rate for temperature below 10^8 K. This new result has a significant impact on the theory of the evolution of massive stars. It significantly increases the predicted age of the oldest globular clusters and helps provide a better constraint on cosmological parameters that determine the present age of the Universe.

ACKNOWLEDGMENTS

I have many people to thank. This project was, at almost every step, a team effort and in many ways it began before I stepped through the doors of LENA. To me, there is no obvious ranking of who assisted more or less, so I will start at the nucleus of this project and work my way outward. (Yes, that was a pun.)

LENA would not exist without the foresight and technical effort of Art Champagne. As my advisor, he led me through the process of constructing a laboratory. I had no prior experience and made innumerable mistakes. He demonstrated remarkable patience. But more important than supporting me in any work at LENA, he supported me during conflicts with the powers that be. This showed confidence in me and my decision making abilities, which I greatly appreciated.

Christian Iliadis was a great teacher throughout this project and supplied perpetual sarcasm. Much of my theoretical knowledge results from his direction and "little white booklets" that anyone in our group knows well. His total skepticism was proven true once or twice.

Chris "Dr. Fox" Fox and the boy Johannes "Turbo" Pollanen were instrumental contributors. They made this project the dog's bollocks. Sitting for long periods of time in a room with no windows, they masterfully operated the accelerator during the day, at night, and sometimes overnight while I slept. I owe a special bit of thanks to Johannes who sought a complete understanding of the UNC Ion Implanter where we spent many a day making targets (and he also partially earned his name). Both of these devoted young lads frequently worked long hours, e.g. the Friday before my first run when we spent 11 hours chasing down a broken BNC cable.

Moving outward brings me to Richard O'Quinn and Chris Westerfeldt who imparted enormous amounts of good advice. Additionally, Richard taught me how to do a job right and the idiosyncrasies of southern life. Chris always provided a quick fix so that Art would not notice broken instruments. Almost surpassing Art's patience, Bret Carlin repeatedly controlled his temper after fried, shocked or otherwise destructively treated electronics equipment was brought to the shop at five o'clock on Friday afternoon. Captain Paul Carter, John Dunham,

Patrick Mulkey and the infamous LENA technician, Scott Williamson, also contributed during LENA's "damn Yankee" phase.

My other group members, including Ryan Fitzgerald, Rich "Junior" Longland, Carrie Rowland and Andreas Stephan, also helped out constructing and running the accelerator. They provided much good advice.

The always-calm-in-the-face-of-a-time-crunch machine shop guys were awesome. They kept me, and especially my designs, down to Earth. LENA and I owe many thanks to Bernie Jelinek, Phil Lewis, Bill Peterson and Robert Timberlake.

Leaving the professional realm, Lauren Caslin, my soul mate, my trouble and strife, kept the machine well oiled. Although she played a behind-the-scenes role, everyone previously mentioned knows how difficult it is to spend an hour or two a lab with me. She has spent six years. She brought me back to reality, e.g. on the evening after I spent 11 hours chasing down a broken BNC cable, and never let me forget what is really important. She filled me with confidence.

On par with Lauren, Philip Hartlieb understood my laboratory successes and failures. He was an indispensable buddy during the graduate school experience. Joseph Caslin, dog, dutifully stood by, endlessly licked my hand and supplied inspiration for the control system design. For the most part, Lauren, Phil and especially Joe remained positive through my entire experience and participated in retreats to the Blue Ridge Mountains that were refreshing for us all. Near the home stretch, Aleshanee Runkle, puppy, entered the picture. She kept me focused while not allowing me to lose perspective during the doldrums days spent in front of my laptop writing. She did this by biting my hand.

Last, but surely not least of all, my family instilled me with enormous self-confidence. They ceaselessly believed in my abilities. Their contribution started many years ago and, without it, I would not have finished this thesis. I also would probably not make strange noises.

TO MY FAMILY

Lauren, Joe, Aleshanee, Philip, Mom, Dad, Jenée, Dan, Scoochers

Be aware of your connection to the earth,
Of the openness of your heart
And the expansiveness of your mind.

NAMASTE

[I honor that place in you
where the whole universe resides.
And when I am in that place in me
And you are in that place in you,
there is only one of us.]

TABLE OF CONTENTS

LIST OF FIGURES

LIST OF TABLES

Number *Page*

Chapter 1:

Why I Sat In A Room With No Windows And A Brief Introduction To Stars

1.1 Why

The Laboratory for Experimental Nuclear Astrophysics (LENA), where almost all of the work presented here took place, is located in the basement of the Duke University physics building. It is relatively small as laboratories go and, due to its previous use as a cyclotron vault, it is surrounded by six feet of concrete. With its absence of windows, it is totally isolated from the outside world aside from internet connections and telephone lines. The research discussed in this thesis and all planned research at LENA serves little to no practical purpose but is solely in pursuit of basic scientific knowledge. This raises the question, "Why would a sane person spend four years in a lab with no windows, sometimes not seeing the light of day, studying something with no practical application?" The answer is that stars are really cool and, in my opinion, the most important objective of a thesis is justifying its existence. In that spirit, it was my goal to write this first chapter on a level that my mother, who has no scientific background, could understand. So here we go…

1.2 Nuclear Astrophysics

Observers have tried to understand the night sky for thousands of years. Ancient civilizations mapped the sky into constellations. The Egyptians hypothesized that a bowl covered the world and holes in it let the light from heaven shine onto Earth. Our understanding has progressed rapidly since then and we now know that the specks of light mapping the constellations are stars. But until the advent of modern telescopes, astronomers did not realize how vastly far away stars reside from us and from one another. At these incredible distances (light-years), stars must produce an enormous amount of light to be visible

here on Earth, but the source of this light remained a mystery. Until the 1900s, scientists understood almost nothing about the inner workings of stars, their extreme numbers or their incredible diversity. Recent advances in technology allow telescopes, such as the Hubble Space Telescope, to bring the incredible cosmos down to Earth and pique public interest. Hubble is merely the first of many telescopes that will observe objects that both further and challenge our understanding of the night sky. Despite the enormous diversity of stars, they all share the property of being interstellar candles. Understanding the source of their light is a quest that has led to profound discoveries about the Universe. At the heart of stars are nuclear reactions which not only make the Sun shine, but also, in previous generations of stars, manufactured the elements necessary for life itself.

The Sun's rays fuel life here on Earth, but the amount of the Sun's energy that Earth actually receives is a negligible fraction of its total energy output, or luminosity. In searching for the source of this enormous amount of energy, perhaps the most obvious place to look are sources we use on Earth everyday. Chemical reactions, e.g. photosynthesis and combustion, power almost everything on Earth, but these processes cannot produce the immense amount of energy that makes our Sun or any star shine. For example, fuel cells burn hydrogen (H) and oxygen (O) gas into water vapor (H_2O):

$$2 \cdot H_2 + O_2 = 2 \cdot H_2O \qquad \text{Equation 1-1}$$

This process releases 3 x 10^7 joules of energy for each kg of hydrogen and oxygen burned. If the Sun were made entirely of these elements, it could only shine as brightly as it does today for approximately 5000 years. This is far too short; from the fossil record and radioactive nuclides, we know that our solar system is on the order of billions of years old! Another potential source is the energy liberated from gravitational contraction of matter, like billions of apples falling from trees. A contracting cloud of the Sun's mass and radius could maintain the Sun's luminosity for around 30 million years. This value is much closer to the age of the Sun, but not nearly large enough. Explaining the Sun's enormous and prolonged energy production requires something far more intrinsically energetic.

The blueprints of our Sun were not laid out until the 1920s by Arthur Eddington and later by Hans Bethe and colleagues [Bet38]. After observing nuclear reactions in the Cavendish

laboratory, Eddington correctly postulated that nuclei may be the source of stellar energy. He made this prediction because the energy stored in nuclei is immense. The average nuclear process exchanges a million times more energy than the average chemical process. The nuclear reactions that Eddington postulated were fusion reactions in which lighter nuclei fuse into heavier nuclei. For example, the vast majority of stars use one particular process: four protons (hydrogen nuclei) fusing into one helium nucleus. This process is called hydrogen burning. The energy liberated derives from the fact that four protons located far away from one another weigh more than four protons bound together in a helium atom. A scale and Einstein's famous mass-energy equivalence principle, $E = mc^2$, explain why hydrogen burning produces energy. Since protons are really, really tiny, let's put 4 billion billion billion protons on one side of the scale and 1 billion billion billion helium nuclei one the other side:

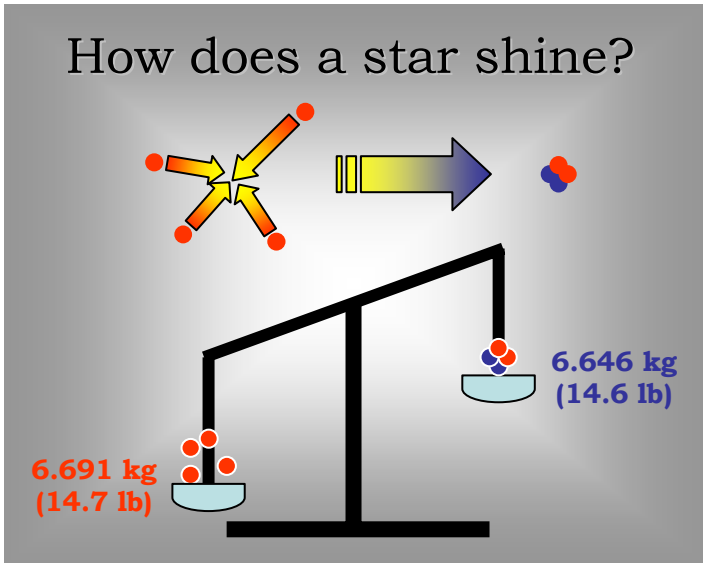

Figure 1-1: Mass of 4×10^{27} protons vs. 1×10^{27} helium nuclei

This figure demonstrates that one helium nucleus is lighter than four protons. The reason for this is that some of what we measure as the mass of protons results from binding energy. Energy is always conserved, and energy and mass are equivalent. The "missing mass" of the protons is converted into energy during fusion. This makes the Sun shine and life on Earth possible!

The mass of the helium nuclei is 0.045 kg lighter than that of the protons. This mass is converted into energy; that's where the mass went! This is enough energy to power a 100 Watt light bulb for more than a million years and that's from just 7 kg (15 lb) of hydrogen. Our Sun

has a mass of approximately 2 thousand billion billion billion kg and is primarily made of hydrogen. By knowing the distance to the Sun and measuring the energy received on Earth, we can calculate the Sun's rate of energy production (or luminosity). It turns out this number is huge: 0.386 billion billion billion watts. Now that's a lot of light bulbs!

Today, the best evidence supporting fusion reactions as the Sun's source of energy comes from studying the tiniest particles: neutrinos. Converting four protons into helium not only releases energy but also two neutrinos. These tiny particles rarely interact with ordinary matter and there are billions traveling through our bodies each second. The source of all these neutrinos is directed towards the Sun. Furthermore, we can accurately predict the flux of neutrinos observed on Earth.

Fusion reactions are quite foreign to the average human experience because they do not naturally occur on Earth. This is because they require enormous temperatures. Protons possess a positive electric charge, and, as a result, they repel one another at large distances through the electromagnetic force[1]. This repulsion is called the Coulomb barrier. However, when protons get very close to one another they stick together. This results from the attractive nuclear force, which is much stronger than the Coulomb force, but only at very short distances - around one million billionth of a meter. So, in order for a fusion reaction to occur, a proton must get past the Coulomb barrier and into the domain of the nuclear force. This is why fusion reactions occur in the Sun but not on Earth. The difference between the Sun and Earth is temperature. Deep down in the center of the Sun, the temperature is approximately 15 million Kelvin. At the center of Earth, it is only 7000 Kelvin. At temperatures around a few million Kelvin, protons are moving very fast and many of them have enough energy to barrel through the Coulomb barrier (as opposed to going over it) and fuse together with another proton[2]. The difference in core temperature between the Sun and Earth results from their vastly different masses of ~ 10^{30} and 10^{22} kg, respectively. In general, more mass means hotter core temperatures.

When a star initially forms, it primarily contains hydrogen and helium, which are remnants

[1] Protons exist on the sub-microscopic scale. In this case, large distance implies 10^{-13} m.

[2] For the physicist reader, this is quantum-mechanical tunneling.

from the formation of the Universe – the Big Bang. As a star evolves, it converts hydrogen into helium through hydrogen burning. Every star passes through this stage where most of its life is spent. But at some point in its lifetime, a star will run out of hydrogen fuel and, if it is large enough, it will burn the helium it created. When three helium nuclei are fused (helium burning), even more energy is released than in hydrogen burning. After the helium fuel is exhausted, the star can fuse carbon nuclei (carbon burning) forming neon, sodium and magnesium. These elements can also be burned, and the burning process can continue to form nuclei all the way up to uranium [Bur57]. Each step in this process requires higher and higher temperatures because larger nuclei have more protons and thus larger Coulomb barriers. In this way, just about all of the nuclei heavier than hydrogen and helium, that we find on Earth (and in the Universe), were formed in stars. All the elements of carbon, nitrogen, oxygen, calcium and iron in our bodies came from the ashes of stars. "We are made of star stuff," Carl Sagan once said. The creation of nuclei, called nucleosynthesis, is the story of how the Universe evolved from simply containing hydrogen and helium, along with a few other light elements, to today's diverse Universe that contains heavy elements.

Energy production and nucleosynthesis are both the result of nuclear reactions in stars. Understanding these two stellar processes is the goal of nuclear astrophysics. This is not a simple task. The example of fusing four protons into hydrogen is, even in its simplest form, a very complex process. It involves at least six different nuclear reactions and can be accomplished in a variety of different ways. Ideally, we would build a model star, throw some nuclei in and see what happens. Unfortunately, this is not possible because igniting nuclear fusion requires enormous temperatures (millions of Kelvin) and enormous amounts of mass (thousands of Earths). This is the fundamental problem in studying stars, which separates this discipline, and astrophysics as whole, from most of physics (and most of the physical sciences). We cannot construct such massive objects in the laboratory. Since we cannot build real models to test our theories, the night sky is the only laboratory – over which we exert no control. Therefore, the only models we can construct are mathematical ones. Using the known laws of physics and the properties of stars that can be observed, we can take a guess at the internal workings and create a model. Assuming a star of a particular mass, stellar models use the probability of nuclear reactions (nuclear physics input) and the conditions inside the

star (thermodynamic input) to predict what happens next. These models predict various stellar features (temperature, luminosity, chemical composition, etc.) that can be checked against observations. The result is a continuous cycle of comparing increasingly accurate models to better and better observations.

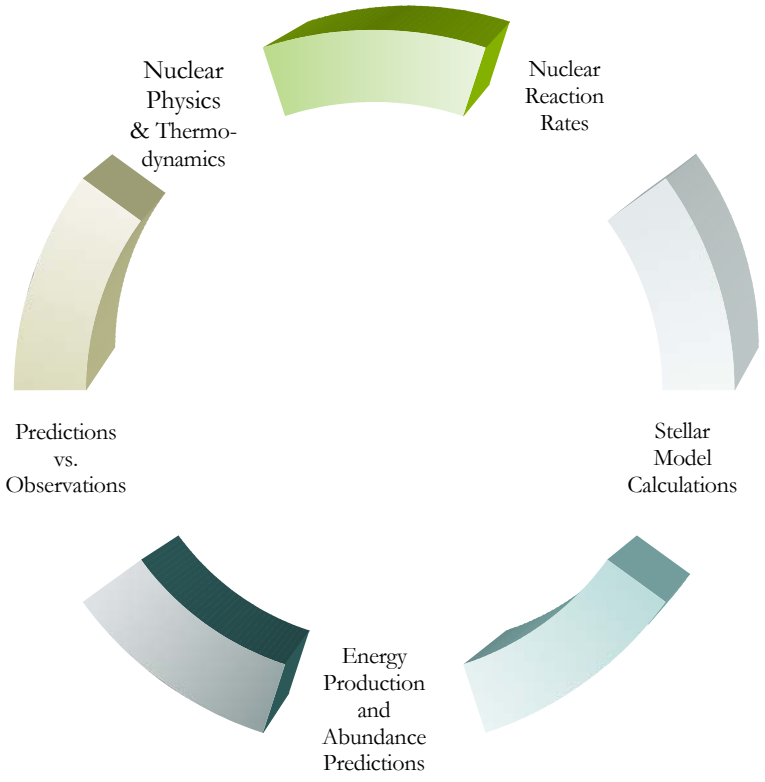

Figure 1-2: Iterative cycle of comparing stellar models to observations

The field of Nuclear Astrophysics provides the nuclear physics input into these models. The nuclear physics input required by stellar models is the probability that each fusion reaction will occur. If one wants to know how often four protons will fuse into a helium nucleus then they need to know the probability of the six reactions that make up this process. Unfortunately, nuclear physics theory is not able to simply calculate the six individual probabilities; they must be measured or inferred from indirect evidence. Without measuring these six and many other nuclear reactions, we would know very little about the inner workings of stars. Fortunately, the last fifty years produced a vast array of nuclear reaction measurements forming the basis for a theory of nucleosynthesis. First generation experiments

made gross estimates of nuclear reaction probabilities but stellar models are now more accurate and precise. These steadily improving models demand new measurements with higher precision and greater accuracy. Measuring the probability of a nuclear reaction occurring inside a star involves replicating the star's high temperature environment. We accomplish this by accelerating nuclei to high velocities and smashing them together. The number that sticks together versus the number that bounces off each other determines the probability of fusion. In the case of this thesis, the reaction of interest is the fusion of a proton and nitrogen; enter a lab with no windows. But before getting into the details of measuring nuclear reactions, let's take a step back and look at the life cycle of stars to understand when hydrogen burning is important in a star's lifetime, and why one reaction, the fusion of a proton and nitrogen nuclei, is crucial to the hydrogen burning process.

1.3 Stellar Evolution

If one looks at all the stars in the sky with a particular set of tools, a distinct pattern emerges. Although it is not obvious, it becomes clear in the famous Hertzprung-Russel (H-R) diagram (figure 1-3), which categorizes stars under two criteria: their surface temperature and luminosity. A graph of luminosity versus surface temperature divides the stars into three principle categories. The vast majority of stars are main-sequence stars, red-giant stars or white dwarves. These groups are so named because they each contain stars at different parts of their life cycles, each having very different internal and external characteristics, which explain their luminosity and surface temperature. The theory of how stars change with time is called stellar evolution, which started with the observations of Hertzprung and Russell. Astrophysicists have worked backwards from the groupings of stars and learned a substantial amount about their life cycles. The present day understanding of stellar evolution, though incomplete, explains a great deal of qualitative and quantitative observations[3].

Stellar models predict that our Sun began hydrogen burning approximately five billion years ago[4]. At that time it formed much like any other star. The formation of a star begins with the condensation of gas and dust in the interstellar medium. The interstellar medium

[3] Good summaries of the basic principles of stellar evolution are given by [Has94] and [Fre00].

[4] This age agrees with well established radioactive age dates from meteorites [Dal91].

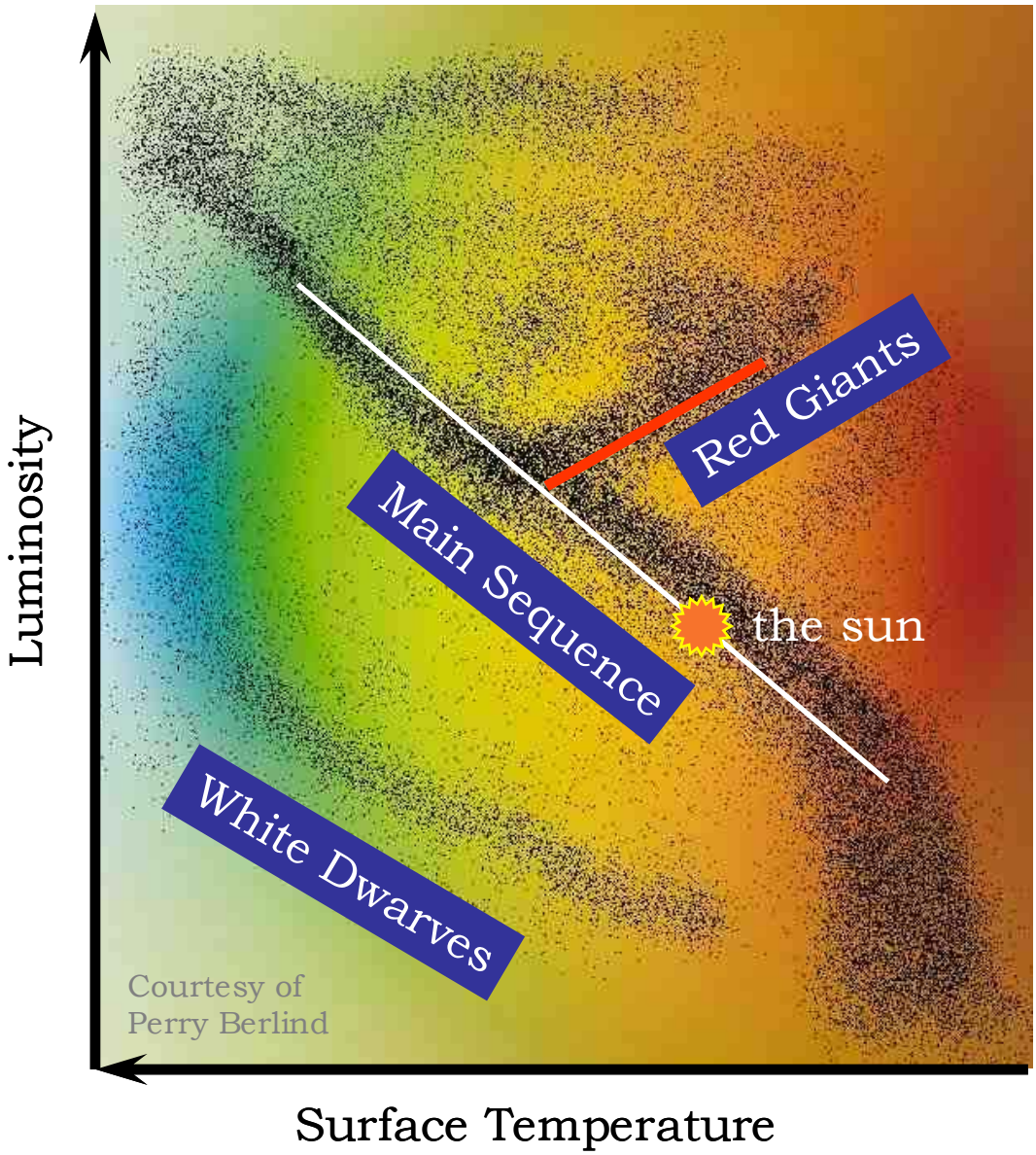

Figure 1-3: Hertzprung-Russell diagram

The H-R diagram is the principle tool that reveals the life cycles of stars and helps test our present day understanding of stellar evolution.

consists mainly of hydrogen and helium with a small fraction of heavier elements. As the cloud condenses under the force of gravity, the heavier elements fall to the center of the star and form an inert core. During this collapse, the energy released from the gravitational contraction warms the proto-star and it begins to shine quite brightly (figure 1-4). However, the contracting sphere is not yet a star.

Figure 1-4: A stellar nursery in the constellation Orion

Embryonic stars shine brightly with the energy released during their gravitational contraction. However, this process can't fuel a star's tremendous energy production for very long.

As the proto-star continues to contract and heat up, the core reaches the critical temperature of a few million Kelvin. Hydrogen burning begins in and around the hot helium core. The proto-star is now a full-fledged member of the main sequence where it will exhibit stable hydrogen burning for billions of years[5]. This is a period of incredible stability where stars spend their time turning hydrogen into helium and slowly building a larger, denser and hotter core. A star will remain on the main sequence for as long as there is hydrogen fuel in its core. When the star burns a significant fraction of its core hydrogen, the nuclear reactions effectively pause.

With the ending of stable hydrogen burning, the helium core contracts further, becoming even hotter. Due to the increasing temperatures, hydrogen in the shell surrounding the core becomes hot enough to ignite and initiates what is called shell hydrogen burning. With the onset of shell hydrogen burning, the star is no longer a main-sequence object. As the helium

[5] In reality, there is a short period of time when a star burns its deuterium. The average lifetime of deuterium is on the order of seconds.

core continues to contract and heat up, shell hydrogen burning moves farther and farther out into the surrounding shell, with the increasing core temperatures forcing this expansion. As the shell temperature rises, so does its pressure, which forces the shell to expand and become much more luminous. The star's radius may grow to many times its original amount and, as the gas cloud expands, it cools, producing a reddish glow. The surface is now cooler, yet more luminous, and the star moves up and to the right on the H-R diagram. It is now a red giant. The Charioteer in the constellation Auriga harbors numerous red-giant stars visible from Earth (figure 1-5). About five billion years from now, there will be a much more famous red giant when our Sun moves off the main sequence onto the red-giant branch!

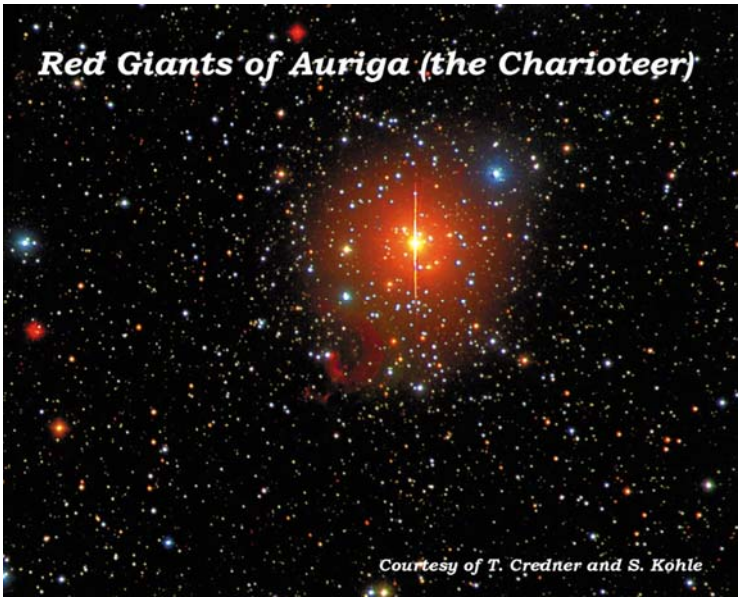

Figure 1-5: Red giant stars

The distinctive color of red-giant stars makes them attractive to photographers. As stars that have just left the main sequence, they are relatively large in volume and, as a result, cool in temperature. But they won't be for long, soon they will move on to the horizontal branch.

The length of time a star remains on the main-sequence depends on its mass. The more mass a star has, the larger its tank of hydrogen fuel. At the same time, more mass means a stronger gravitational attraction and higher temperatures. Since nuclear reaction rates increase quickly with increasing temperature, the more massive a star, the *faster* it exhausts its hydrogen fuel. This implies that the more massive a star, the sooner it evolves off the main-sequence.

In fact, the most massive stars (> 200 M_{sun}, i.e. 200 times the mass of the Sun) barely remain on the main-sequence at all. Our Sun will be a main-sequence star for approximately ten billion years. The length of time (τ_{MS}) required for a star of mass M to exhaust its core hydrogen fuel, the main-sequence lifetime, is strongly mass dependent:

$$\tau_{MS} \cong \left(\frac{2.5 \cdot M_{sun}}{M} \right)^{2.5} \text{billion years} \qquad \text{Equation 1-2}$$

On the H-R diagram, the more massive stars are located towards the upper left because they are very hot and quickly burn their hydrogen fuel, which results in a large luminosity. The mass decreases moving down and to the right along the main-sequence, as the rate of energy production slows, reducing both the luminosity and surface temperature.

Once a star moves off the main sequence, its evolution rapidly progresses. Post main-sequence evolution also strongly depends on stellar mass. After the core temperature reaches approximately 100 million Kelvin, a star begins helium burning. Lower mass stars ($< 3 \cdot M_{sun}$) like our Sun have dense cores and experience a brief flash of helium burning. This flash releases enormous amounts of energy ($10^{11} \cdot L_{sun}$) and marks the onset of the helium burning stage. After helium flashing, a star actually becomes less luminous because the helium core expands, reducing the temperature and thus the rate of hydrogen shell burning. The shell burning region still provides most of the star's luminosity, and when the temperature, and in turn the energy production decrease, so does the luminosity. Decreasing temperatures in the outer layer allow the star to contract and heat up. This moves the star slightly down and to the right on the H-R diagram, onto the "horizontal branch". A stable period of helium burning lasts less than a billion years (a small fraction of its main-sequence lifetime) until the star converts most of its core helium into carbon and oxygen. During this period, high surface temperatures give the horizontal-branch stars their characteristic blue color. These are the blue stars in figure 1-6. Similar to the end of hydrogen burning, the core contracts and heats up until helium surrounding the core ignites. This period of shell helium burning once again cools and expands the star forming a second red-giant phase. The star moves further up and to the right on the H-R diagram becoming an asymptotic-giant-branch (AGB) star. About eight billion years from now, our Sun will enter the AGB and evaporate the Earth!

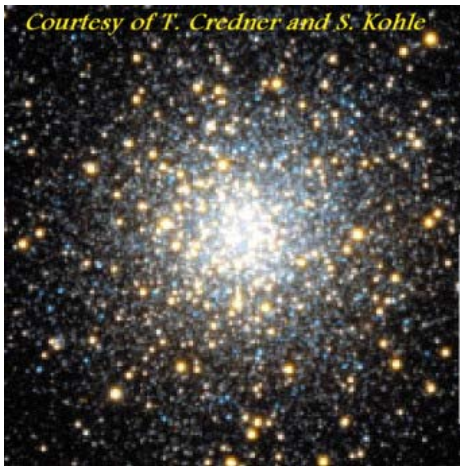

Figure 1-6: Blue horizontal branch stars in Ophiuchus.

The blue horizontal stars have very hot surfaces evident from their blue color.

The star is now reaching the final stage of its life cycle. As the star burns its shell helium, it experiences various thermal pulses that eject about half of its mass into the interstellar medium. Only the inert carbon-oxygen core remains, since the core is not hot enough to initiate carbon burning. Ultraviolet radiation from the core excites the ejected shell material and makes it glow. Many of these poorly named "planetary nebulae" are observable from Earth (see figure 1-7). In the absence of nuclear reactions, the star is officially dead and the sweltering core slowly cools and fades away. This is the fate of our Sun, which will eventually evolve into a white dwarf the size of Earth.

The evolution of massive stars is more exciting. The most massive stars, with hotter and less dense cores, do not experience a helium flash but gradually enter a period of stable helium burning. They then follow a path similar to lower mass stars, but the hotter cores of massive stars are capable of igniting carbon burning after helium burning ceases. Carbon burning produces the elements neon, magnesium and sodium which can then be burned to form heavier and heavier elements. This process continues up to silicon burning. Throughout this time, the star experiences several red-giant phases as it expands and contracts from the exhaustion of one fuel, and the subsequent burning of the next element. The duration of each period is smaller and smaller as the core becomes hotter and hotter. For very massive stars, the period between helium burning and the end of silicon burning may last only a few million

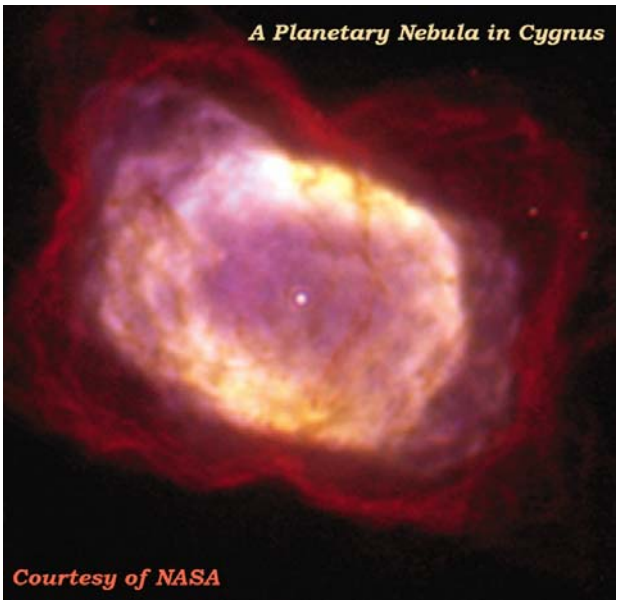

Figure 1-7: A planetary nebula

This planetary nebula formed when a star (center) ejected most of its mass. The star is now a white dwarf and will slowly fade away.

years. Silicon burning results in an iron core and ends the burning process. For nuclei lighter than iron, a star can release energy by fusing nuclei together, but fusing nuclei heavier than iron *requires* energy. (This is why a fission reaction releases energy and produces electricity!)

At this point, stars below 8 solar masses eject their shells as planetary nebulae and become white dwarves, but more massive stars continue to evolve. Since a star can no longer produce energy by fusion after building an iron core, the only source of energy is gravitational contraction. At these masses, the gravitational contraction is so immense that it results in the breakdown of the iron core into a sea of neutrons, protons and helium nuclei[6]. (Neutrons are similar to protons but have no electric charge and do not electrically repel one another as nuclei do.) With the formation of a neutron core, the star no longer contracts[7]. The neutron core becomes rigid and emits a powerful shockwave into the surrounding shells. This is the final stage of evolution; the star ejects an enormous amount of energy and mass into the interstellar medium, becoming a supernova. This event is perhaps the most impressive event

[6] Prior to this point, electron degeneracy supported the gravitational attraction. Electron-capture forms neutrons and removes the electron degeneracy.

[7] At very large densities, the nuclear force becomes repulsive.

in the Universe, which astronomers most recently observed in 1987. SN1987A, as it is called, had a luminosity of 10^8 L_{sun} at its peak! Figure 1-8 shows a picture of SN1987A soon after its peak; notice how much brighter it is than all the surrounding stars and even than the large object in the upper left corner of the photograph – and it's just one star!

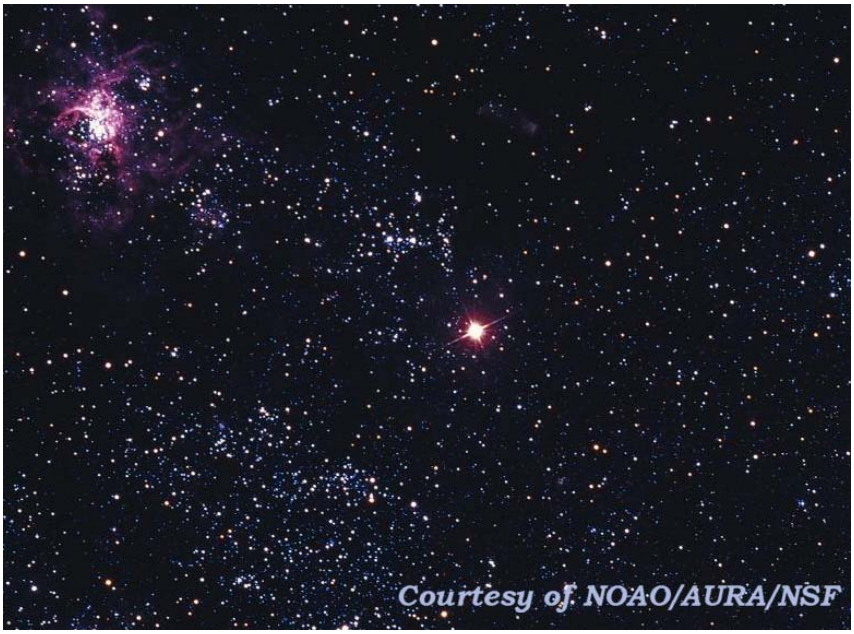

Figure 1-8: SN1987A

SN1987A was a spectacular event. It was easily visible with the naked eye. At its peak, it shined 10^8 times brighter than the Sun. In this picture, it is brighter than all the other stars combined. It is even brighter than the planetary nebulae located in the upper left hand corner.

After a supernova, the residual core forms a neutron star. These are some of the most fascinating stellar objects because of their bizarre properties. Neutron stars with intense magnetic fields produce pulsars. But the most intriguing of all stellar objects are black holes, which result from neutron stars greater than 2 to 3 solar masses. Because of their incredible density, they cannot counter their mutual gravitational attraction and collapse in on themselves. They are the subject of much theoretical research and are the basis for speculation about the existence of multiple universes and wormholes. Numerous galaxies and star clusters are known to harbor black holes at their center, including the Milky Way galaxy. Figure 1-9 shows two.

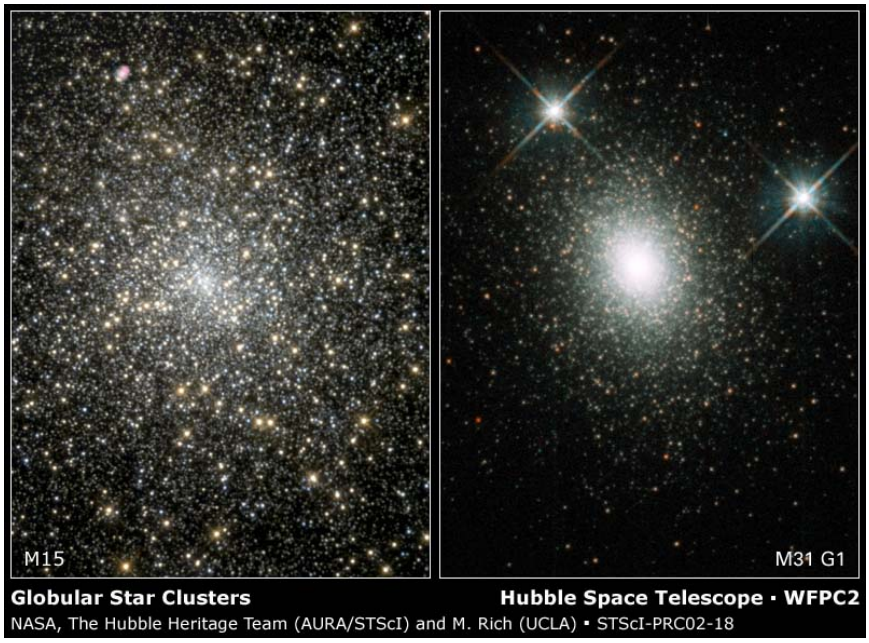

Figure 1-9: Black holes surrounded by star clusters

We believe that most galaxies orbit black holes, including the Milky Way. Who knows what's inside of them?

Stellar evolution describes how nuclear reactions dictate the macroscopic properties of stars. Throughout a star's lifetime, hundreds of different nuclear reactions occur, but for the vast majority of this time a star simply burns hydrogen on the main-sequence. Core hydrogen burning produces a star's main-sequence luminosity. Even during the red-giant phase, shell hydrogen burning makes a star luminous. Therefore, since the vast majority of stars reside on the main-sequence or red-giant branch, hydrogen burning is really what lights up the night sky. Understanding hydrogen burning therefore forms the basis of understanding stars.

1.4 Globular Clusters & the Age of the Universe

Stellar evolution explains the evolutionary track for a star of a particular mass and how it moves around the H-R diagram. If these principles are extended to groups of stars with varying masses, we can explain their cumulative H-R diagram. One important star group is globular clusters (see figure 1-10), which are tightly packed clusters usually containing between thousands and hundreds of thousands of stars. Figure 1-11 shows the H-R diagram for the globular cluster M55. It looks similar to the H-R diagram in figure 1-3 except that the more massive stars on the top half of the main sequence are gone! This results from the heavier

stars evolving off the main sequence onto the red-giant and horizontal branches.

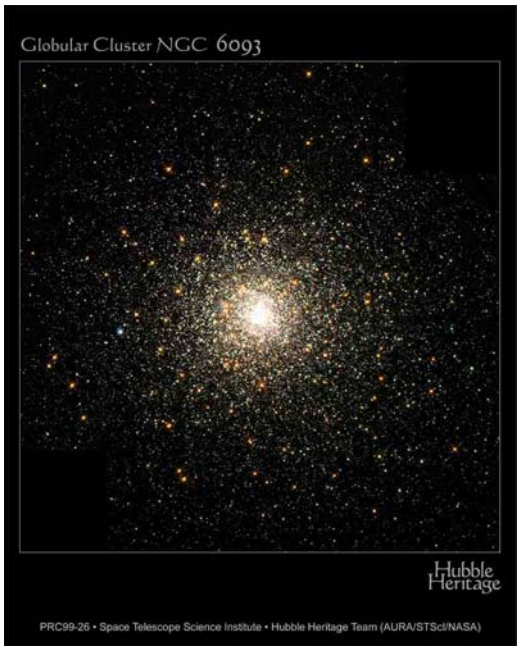

Figure 1-10: Globular cluster NGC 6093

This is one of the oldest globular clusters and, in fact, one of the oldest objects astronomers have observed. The oldest globular clusters provide a lower limit on the age of the Universe.

Since the rate of evolution and time spent on the main sequence are a function of stellar mass, this provides a framework for determining the age of a globular cluster. The most massive stars, ~100 M_{sun}, quickly move off the main sequence onto the red-giant and horizontal branches. A few billion years later, 10 M_{sun} stars follow them. After about 10 billion years, stars like our Sun move off the main sequence. As time goes on, lower and lower mass stars continue to follow this process. For each globular cluster, there is a particular mass which resides on the border of the main-sequence and the red-giant branch. We call this the main sequence turn-off point (MSTO). By determining the mass of stars at the MSTO, one can determine the age of the globular cluster. Using this technique, we have concluded that globular clusters are some of the oldest objects in the Universe. Some globular clusters contain only small concentrations of elements other than hydrogen and helium, indicating that they formed mainly from the remnants of the Big Bang. This implies that they formed soon after the formation of the Universe (otherwise they would contain recycled material from

previous generation stars like our Sun, which contains many heavy elements including a large iron core). The age of globular clusters, or any object, provides a constraint on the age of the Universe.

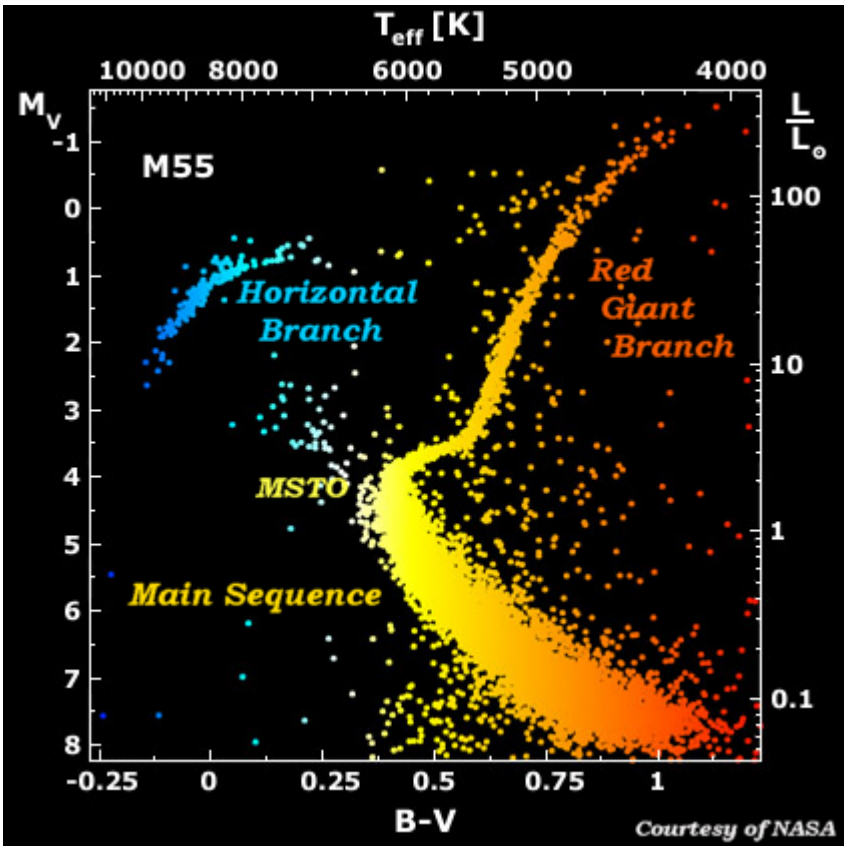

Figure 1-11: HR diagram for the globular cluster M55

This H-R diagram looks very different from the one in figure 1-3. That's because the stars shown here all populate the same cluster, M55. They all formed at approximately the same time. Notice that the upper half of the main-sequence is missing. These stars have evolved onto the red-giant and horizontal branches. The most important characteristic in determining the ages of globular clusters is the mass of stars at the main-sequence turn off point (MSTO).

Cosmology describes the formation, and subsequent expansion, of the Universe. In our Universe, large scale objects, e.g. galaxies, are all moving away from one another. This expansion implies that the farther away objects reside, the faster they are moving away from us[8]. By measuring the velocities and distances of different objects in the Universe,

[8] This is not obvious but can easily be demonstrated, see [Fre02].

astronomers can calculate the Hubble constant, which relates the distance between two objects to the velocity between them. The present value of the Hubble constant is 71(7) km/sec/Mpc [Fre00]. (In other words, a galaxy that is at a distance of 1 Megaparsec [3.26 x 10^6 light-years] from Earth is moving 71 km per second away from us.) Depending on one's model of the Universe, the elapsed time since the Big Bang is proportional to the Hubble constant. For the traditional model of the Universe, in which gravity slows a perpetual expansion, the age of the Universe (τ) is [Free00][9]

$$\tau = \frac{2}{3} H_0 \sim 9\, billion\ years \qquad \text{Equation 1-3}$$

The formation of globular clusters must have occurred after the Big Bang. This means that dating globular clusters provides a *lower limit* on the time elapsed since the Big Bang, and thus the age of the Universe. Since globular clusters couldn't have formed before the Universe itself, they must be *younger* than 9 billion years in order to be consistent with a flat Universe, i.e. a Universe with a large scale geometry similar to Earth. Assuming a conservative estimate for the time between the Big Bang and initial star formation of 1 billion years, globular clusters must be less than 8 billion years old. Two recent reviews compared estimates of globular cluster ages [Fre00] [Gra97]. They estimated the ages of the oldest globular clusters to be 11.7 $\pm$ 1.7 billion years old. This conflicts with the age of the universe assuming a flat geometry. But different models of the Universe predict very different ages, and, in addition to the Hubble constant, the age of the Universe depends on other important cosmological parameters, including the matter density (Ω_m) and the dark (intrinsic) energy density (Ω_λ). Other possible models are shown figure 1-12 along with the globular cluster ages. It is important that globular cluster age dates are consistent with the age of the Universe because they provide a check, with vastly different systematic errors than present in measuring the Hubble constant (and other parameters).

Although the models used in calculating globular ages are complex, there are seven principle factors which dominate the uncertainty: The fourth largest is the rate of one nuclear reaction: a proton fusing with a ^{14}N nuclei. A recent Reviews of Modern Physics article by

[9] The traditional (Einstein-de Sitter) model assumes a matter dominated Universe with Ω_{tot} equal to one.

Adelburger et al. [Adl98] judged the previously reported uncertainty in this reaction rate to be significantly underestimated. This re-assessment does two things. First, it means this reaction rate, with its present uncertainties, is probably the second or third largest uncertainty in globular cluster ages. Second, the total uncertainty in globular cluster ages is much larger than previously reported. Adelberger et al. suggest that a better estimate adds as much as one billion years to the uncertainty in the globular cluster ages.

Figure 1-12 compares the globular cluster age estimates with various cosmological models. If one adds an additional one billion years on their error bar, globular cluster ages do not provide much restriction on the values of Ω_m and Ω_λ. However, if the uncertainty of the proton plus ^{14}N reaction could be reduced, globular cluster ages would provide an important constraint on cosmological models.

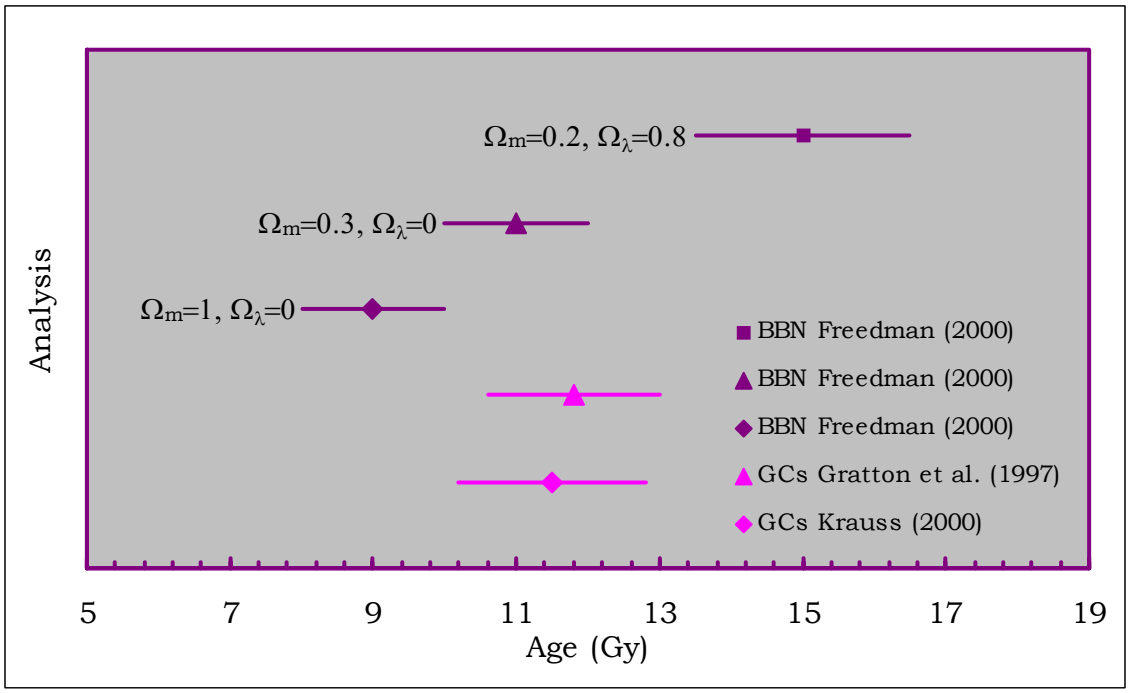

Figure 1-12: Estimates of the age of the universe

The ages of globular clusters help constrain cosmological parameters. One important factor in constraining the ages of globular clusters is the $^{14}N(p,\gamma)^{15}O$ reaction rate. A more precisely known reaction rate will reduce the uncertainty in their ages.

1.5 The CN Cycle and the $^{14}N(p,\gamma)^{15}O$ Reaction

Hydrogen burning is a crucial element in understanding a star's luminosity, evolution, and nucleosynthesis. The term hydrogen burning is vague because the process of fusing four protons into helium can be accomplished in a number of different ways. Most commonly, stars directly fuse four protons into helium in what is called the proton-proton (pp) chain. In other environments, this is more easily accomplished (i.e. faster) using heavier elements as catalysts[10]. (Catalytic cycles use heavier nuclei to accomplish the same end result as the pp chain. The heavier nuclei are not altered during the process.)

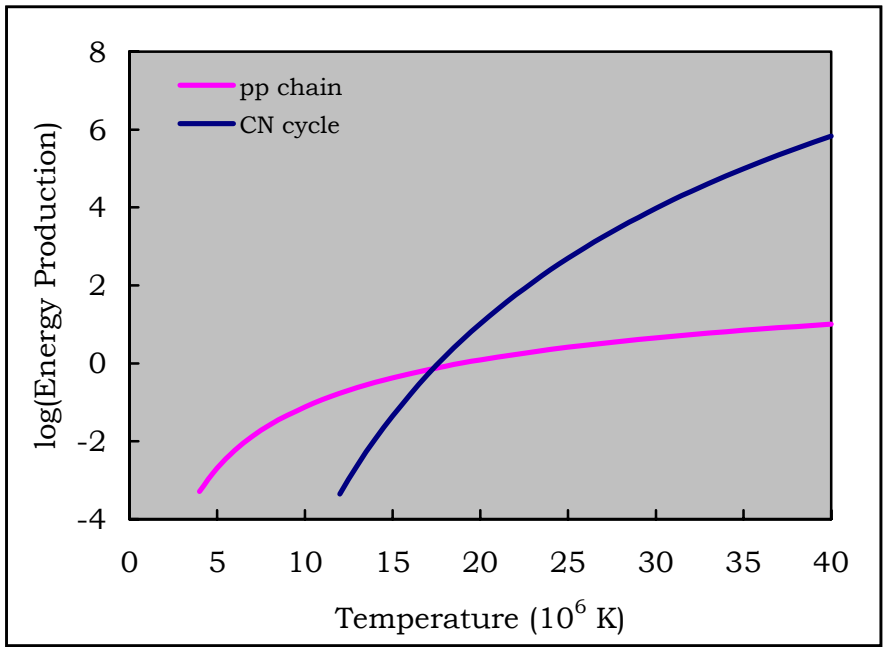

Figure 1-13: Energy production from hydrogen burning

Only two processes dictate energy production in main-sequence stars. For stars a bit larger than the Sun, the CN dominates.

The most important example of a catalytic cycle is the carbon-nitrogen (CN) cycle; others include the neon-sodium and magnesium-aluminum cycles. A particular star favors one process over the other depending on its temperature and chemical composition. If a star is a first generation star and contains few elements heavier than helium, then the pp chain will dominate during its main-sequence lifetime. However, if a star contains a significant

[10] This is primarily due to the slow inverse beta-decay process that dominates the first step of the pp chain.

abundance of carbon and nitrogen, then the pp chain has a higher probability of occurring at lower temperatures and the CN cycle at higher temperatures. Figure 1-13 shows the energy dependence of these two processes. For the purposes of this thesis, stars large enough to have central temperatures of 16 million Kelvin are of interest since the CN cycle contributes significantly. These stars are normally a little bit more massive than our Sun ($>2 \cdot M_{sun}$). As a star moves off the main-sequence and initiates helium burning, it produces significant amounts of carbon. During this period of shell hydrogen burning, the CN cycle dominates, even in stars that initially contained little or no heavier elements. Therefore, the CN cycle influences energy production even in lower mass stars at later stages of their evolution on the red-giant branch.

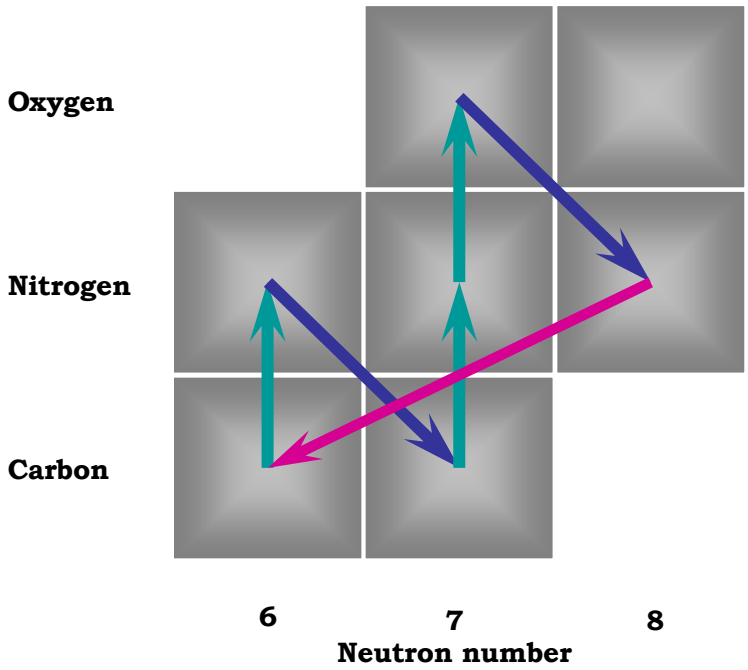

Figure 1-14: The CN cycle

The CN cycle contains six steps. Three steps capture a proton and emit a γ-ray (green). Two steps emit a positively charge electron (blue). One step captures a proton and emits a helium nucleus (red). The slowest reaction, which dictates how quickly this cycle progresses, is proton capture on nitrogen forming oxygen.

The CN cycle uses the elements carbon, nitrogen, and oxygen in a six step process shown in figure 1-14. Since this is a cycle, any nuclei can initiate the process and will simply go

around and around. For simplicity, let's assume that helium burning just created a ^{12}C nucleus (lower left-hand corner). The first step, shown in green, is the capture of a proton which forms ^{13}N. The second step, shown in blue, is β^+-decay by the ^{13}N nucleus, i.e. emission of a positron (positively charged electron) and a neutrino. The resulting ^{13}C nucleus experiences proton capture and forms the bottleneck nucleus ^{14}N. The next step, fusing a proton with ^{14}N, is the most important step of the CN cycle. This reaction forms ^{15}O which also experiences β^+-decay. The final step involves the ^{15}N nucleus absorbing a proton and emitting a helium nucleus. Thus, we are back where we started with ^{12}C nucleus. The heavier nuclei were simply catalysts, but 4 protons have been converted into helium! All six steps produce energy, and the sum of all the energy released is the same amount as in the pp chain.

The rate of revolution of the CN cycle determines the rate of energy production (because this is the amount of hydrogen burning that occurs). The rate at which any process cycles is limited by its slowest step. In the case of the CN cycle, the fusion of a proton with ^{14}N is the slowest step for temperatures existing in main-sequence stars. This reaction, written more technically as $^{14}N(p,\gamma)^{15}O$, occurs when a proton hits a ^{14}N nucleus creating an ^{15}O nucleus. [More generally, the notation A(p,γ)B means that A is the target nucleus, p is the incident proton, B is the product nucleus and a γ-ray is emitted.] When the ^{15}O nucleus forms, it exists in an excited state and releases energy by emitting a γ-ray only a tiny fraction of a second after forming. Figure 1-15 illustrates this process.

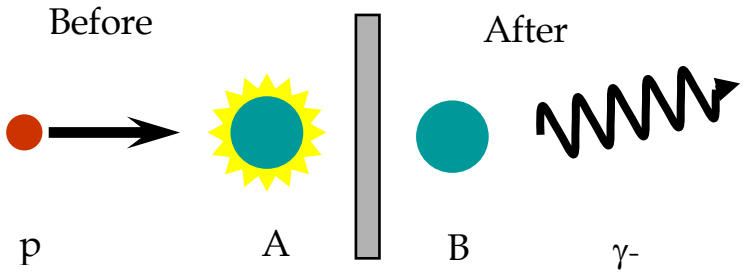

Figure 1-15: Reaction formalism

Since the $^{14}N(p,\gamma)^{15}O$ reaction is the slowest reaction in the CN cycle and the CN cycle governs energy production in massive stars, the $^{14}N(p,\gamma)^{15}O$ reaction dictates the rate of energy production in massive stars. This implies that one reaction controls energy production in

almost all main sequence stars above $2 \cdot M_{sun}$. The idea that a single reaction, involving some of the tiniest particles that are far smaller than what the human eye can see, dictates the life cycle of the largest objects in the Universe, is truly profound. This is the most astonishing fact that I have learned in my graduate career. The lifetime of a star, its structural evolution, its nucleosynthesis and other factors are all primarily determined by the rate of one nuclear reaction. For this reason, the principle goal of this thesis is to better understand this reaction by experimentally determining its probability and thus shedding light on the inner workings of massive stars.

1.6 Measuring Nuclear Reactions

Measuring the probability of a nuclear reaction, and in turn its reaction rate, is conceptually straightforward. For convenience, nuclear physicists express the probability in terms of the nuclear cross section (σ). The term cross section implies an area, i.e. the effective cross sectional area of the nucleus. The larger the effective cross section, the larger the area and the more likely it is for a proton to strike and fuse with the ^{14}N nucleus. Although this is not a physically accurate picture, it is conceptually useful. Determining the cross section of this reaction simply requires determining how many protons actually create a ^{15}O nucleus for each ^{14}N nucleus in the target. This implies that σ is given by:

$$\sigma \approx \frac{number\ of\ emitted\ \gamma - rays}{number\ of\ incident\ protons \cdot number\ of\ ^{14}N\ nuclei} \qquad \text{Equation 1-4}$$

In practice, we measure the nuclear cross section by taking a target, filled with ^{14}N nuclei each of "area" σ, and directing a beam of protons at it. At the same time, since the ^{15}O nuclei decay almost immediately, we count the number of γ-rays emitted. This doesn't occur very often; at the temperatures in the core of the Sun a single ^{14}N nucleus has a 2 in 10^{18} chance of fusing with a proton. Nevertheless, this is a nuclear physicist's "ruler". Since the cross sections of nuclei are very small, normally less than 10^{-24} cm^2, we can't measure them by hand!

The vast majority of work presented in this thesis relates to measuring the cross section of the ^{14}N(p,γ)^{15}O reaction. Achieving this goal required completing two steps. The first was assembling a laboratory that could be used to measure this reaction. Of the almost four years spent on this project, assembling the Laboratory for Experimental Nuclear Astrophysics

(LENA) took two and a half. The term "assembling" includes plumbing, electrical and design work, endlessly chasing leaks in the vacuum systems, destroying vacuum pumps, putting together a jigsaw puzzle of accelerator parts, almost killing my advisor by not grounding the accelerator column, installing and writing code for a LabVIEW control system, blowing up Fieldpoint control modules, installing electronics, setting things on fire, drinking too much champagne after finally getting beam on target immediately before Nuclear Theory class, calibrating detectors and flooding the lab numerous times after the de-ionized water system exploded. Oh, how could I forget, and consistently harassing the technical staff for three years. Despite my total lack of experience or qualifications, LENA eventually came on-line and has been running consistently since March 2002. Since LENA is simply a means to an end, I give a greatly abbreviated discussion of this work in chapter 3. This brings me to the second step of actually measuring the $^{14}N(p,\gamma)^{15}O$ cross section. As the ultimate goal of this thesis, we spent numerous hours over the course of one year directing a beam of protons at various energies onto many different nitrogen targets in order to understand this reaction. In chapter 2, I introduce the foundations of quantifying and extrapolating a nuclear reaction from the measurable energies down to those that actually exist in stars. Chapters 4 and 5 are devoted to the actual data collection and analysis of the results as well as implications of our measurement.

1.7 Notes

In the hope of keeping the reader's attention, I avoid using the passive voice whenever possible. The work contributing to the results of this thesis was, at almost every step, a team effort. I therefore normally use "we" instead of "I". For each chapter, I attempt to include everyone who contributed significantly. I even include Ryan Fitzgerald despite the fact that on almost every experiment he crashed the accelerator, vented the vacuum system, or burned through a target.

Whenever discussing energies, they are in the center of mass reference frame unless otherwise stated. The only deviation from the center of mass frame occurs in chapter 3 when discussing the Laboratory for Experimental Nuclear Astrophysics.

Parentheses indicate uncertainties on measured quantities after the measured value, e.g. 1.1(2) is equivalent to 1.1 ± 0.2.

Throughout this thesis, I quote references using the first three letters of the first author's last name and the last two characters for the year of publication.

Chapter 2:

Determining Nuclear Reaction Rates

2.1 Reaction Rates, Cross-sections and the Astrophysical S-factor

The nuclear reaction rate determines the influence of any nuclear reaction on a particular stellar environment. By definition, the reaction rate is the rate at which nuclear reactions take place per unit volume per second. The three primary contributions to this rate are: the nuclear reaction probability (given by the cross section), the energy distribution of the particles (a function of temperature), and the particle number density. Since the nuclear reaction probability and the particle energy distribution are strongly energy dependent, the reaction rate between nuclei x and y is defined as the integrated product of these three quantities over all energies:

$$r = N_x N_y \langle \sigma v \rangle = N_x N_y \int_0^\infty \sigma(E)\phi(E)dE \qquad \text{Equation 2-1}$$

where $<\sigma v>$ is the reaction rate per particle pair, N_x (N_y) is the x (y) particle number density, $\sigma(E)$ is the cross section, and $\phi(E)$ is the particle energy distribution[11]. Stellar environments exist in thermal equilibrium with particle energies described by a Maxwell-Boltzmann distribution:

$$\phi(E) = \left(\frac{8}{\pi \cdot \mu}\right)^{\frac{1}{2}} \left(\frac{1}{k \cdot T}\right)^{\frac{3}{2}} \cdot E \cdot e^{\frac{-E}{k \cdot T}} \qquad \text{Equation 2-2}$$

In charged particle reactions, such as main sequence hydrogen burning, the Coulomb barrier causes a rapid decrease of the cross section at low energies. To separate the nuclear physics from other effects, the cross section is typically expressed in terms of the astrophysical S-factor, S(E), defined as:

$$\sigma(E) = \frac{1}{E} \cdot S(E) \cdot e^{-\frac{1}{\hbar}\cdot\frac{Z_x \cdot Z_y}{2\cdot\varepsilon_o}\cdot\sqrt{\frac{\mu}{2\cdot E}}}$$ Equation 2-3

where Z is each nuclei's charge and μ is the reduced mass of the system. The first term of this expression is commonly called the "geometric" term. It results from the maximum geometrical cross section in the semi-classical limit. The exponentially decaying term approximately describes the Coulomb barrier penetration probability of a particle with no orbital angular momentum. This leaves the S-factor which ideally contains all of the nuclear physics information. Figure 2-1 compares the cross section to the S-factor. The cross section precipitously drops nine orders of magnitude between 50 and 450 keV. The S-factor has much weaker energy dependence; it varies less than one order of magnitude in the same energy window.

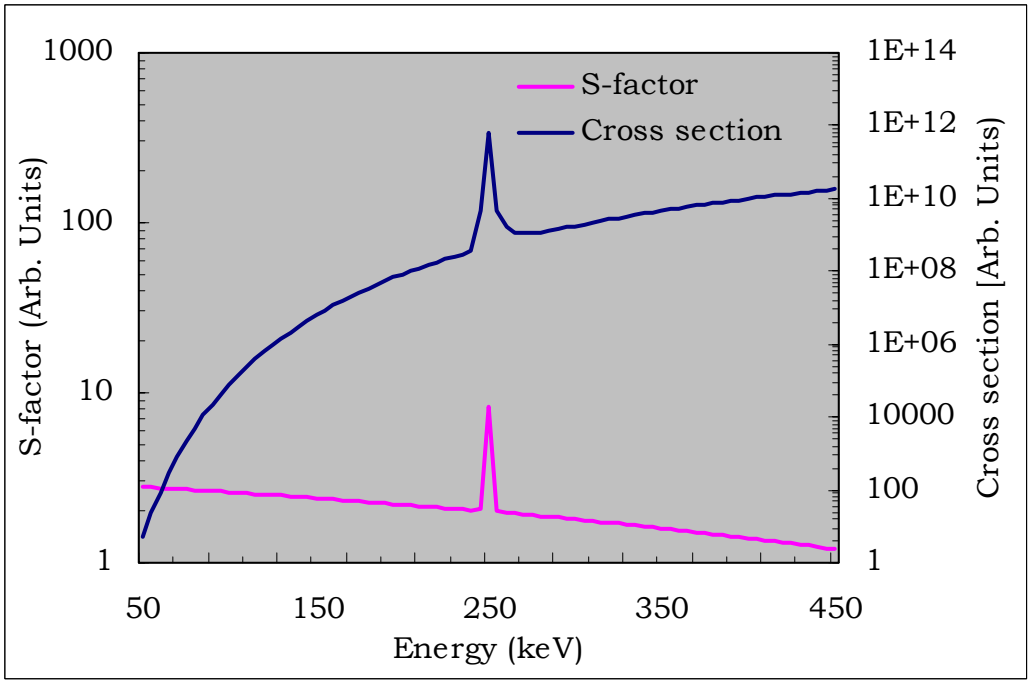

Figure 2-1: Cross section vs. S-factor

The cross section quickly drops at low energies while the S-factor is relatively constant. This makes the S-factor much easier to extrapolate into the low energy region.

[11] This expression assumes that X and Y are not identical particles. In this case, a factor of ½ multiplies the entire expression.

Substituting these quantities into the reaction rate per particle pair gives:

$$r = N_x N_y \left(\frac{8}{\pi \cdot \mu}\right)^{\frac{1}{2}} \left(\frac{1}{k \cdot T}\right)^{\frac{3}{2}} \cdot \int_0^{\infty} S(E) \cdot e^{-\frac{1}{\hbar}\cdot\frac{Z_x \cdot Z_y}{2\cdot\varepsilon_o}\cdot\sqrt{\frac{\mu}{2\cdot E}} - \frac{E}{k\cdot T}} dE \qquad \text{Equation 2-4}$$

Due to the rapidly decreasing Maxwell-Boltzmann distribution and the rapidly increasing cross section as energy increases, the integrand sharply peaks around a small energy window. If the S-factor is constant over this region, then it can be removed from the integral resulting in a direct proportionality between the reaction rate and S-factor.

This energy window, termed the Gamow peak, is frequently the only energy region that significantly contributes to the reaction rate. Its shape is approximately Gaussian with a mean value and full-width-half-maximum given by the following expressions [Rol88]:

$$E_o = \left(\frac{\sqrt{\mu} \cdot Z_x Z_y \pi \cdot e^2 \cdot kT}{\sqrt{2} \cdot \hbar}\right)^{\frac{2}{3}} \qquad \text{Equation 2-5}$$

$$\Delta E_o = \frac{4}{\sqrt{3}} \left(E_o \cdot kT\right)^{\frac{1}{2}} \qquad \text{Equation 2-6}$$

The location of the Gamow peak dictates the energies of astrophysical importance for a particular site. Below is a table of Gamow energies for the $^{14}N(p,\gamma)^{15}O$ reaction in various astrophysical sites:

Site	$T_6(10^6$ K)	kT (keV)	E_o (keV)	ΔE_o (keV)
Sun	15	1	27	14
Red Giant	40	3	50	30
AGB	80	7	81	50
Nova	200	17	150	60
Supernova	> 1000	> 90	> 440	> 500

Table 2-1: Astrophysically relevant energies

Energies surrounding E_o are the most relevant for each site. These energies are comparatively low and direct measurements in this region are challenging.

The sites listed above range from average stars like our Sun to the hottest astrophysical environments. In each case, the Gamow window occurs at a relatively low energy on the nuclear scale. The tiny cross sections at these energies make measuring most reactions in the Gamow peak very difficult. This is the fundamental challenge of nuclear astrophysics, which in almost all cases necessitates extrapolating higher energy data to these low energy regions (at least for nuclei beyond helium). For E_o below 50 keV, one often assumes the S-factor in equation 2-4 to be constant (or linear) and only the zero-energy S-factor value is used, S(0). In these cases, the reaction rate is directly proportional to the S(0) value.

The overall goal of this project is to reliably extrapolate the $^{14}N(p,\gamma)^{15}O$ cross section into the above energy regions. Presently, this extrapolation is the largest uncertainty in the $^{14}N(p,\gamma)^{15}O$ reaction rate. Accomplishing this goal requires an understanding of the mechanism through which the $^{14}N(p,\gamma)^{15}O$ reaction proceeds. Understanding the reaction mechanism provides important information about the behavior of the cross section as a function of energy which can then be normalized to existing, higher energy data.

2.2 [Basic] Nuclear Reaction Theory

The theory of nuclear reactions involves the interaction of individual nucleons through both the nuclear and electromagnetic forces. Despite approximately 70 years of study, the nuclear force is not understood in a fundamental manner. However, approximations that apply to specific nuclear phenomenon are sometimes accurate and useful. Although it is beyond the scope of this paper to explain the approximate quantum-mechanical description of nuclei fusing together, I will attempt to layout the general concepts and formalism of proton capture reactions relevant to astrophysics.

The nuclear cross section describes the probability of a reaction and is a combination of the attractive nuclear interaction and the repulsive Coulomb interaction. In contrast to the nuclear force, the Coulomb force is well understood. (In fact, the Coulomb interaction between a proton and an electron is the most accurate and precise physical measurement.) Since the S-factor describes the nuclear physics of a reaction, S-factor data, such as those

displayed in figure 2-2[12], help reveal the nuclear structure influencing the reaction mechanism. In this example, the data exhibit two general characteristics. First, the S-factor is, for the most part, smoothly varying over a large energy range. Second, over a small energy range near 250 keV, the S-factor rapidly changes by orders of magnitude. Two distinctly different models describe these radically different energy dependences. The direct capture model, where the proton emits a γ-ray on the nuclear periphery and directly enters a bound state in the parent nucleus, explains the smoothly varying portion of the S-factor. A region of rapid increase and decrease normally correlates to a known energy level in the parent nucleus and is therefore a resonant process. For energies near the reaction threshold, where distinct, isolated nuclear states exist, direct and resonance capture are the two contributions to the reaction mechanism. I discuss these processes, the theory behind them and their influence on the $^{14}N(p,\gamma)^{15}O$ reaction in the next two sections.

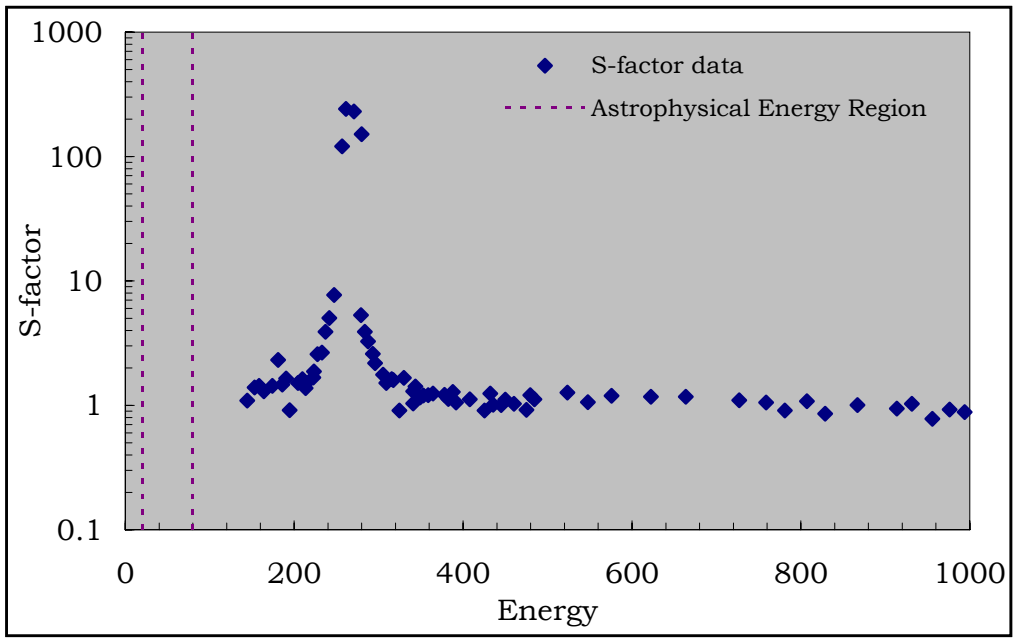

Figure 2-2: Direct and resonance capture in the $^{14}N(p,\gamma)^{15}O$ reaction

In this particular example, both direct and resonance capture occur, but a clear distinction exists between them. Distinguishing between these processes is crucial in attempting to

[12] Data displayed here are from [Sch87] and the present work.

extrapolate to astrophysical energies (shown with dashed lines). Unfortunately, such a clear distinction does not often exist since a reaction may proceed through both direct and resonance capture in the same energy region. Near resonances, the direct capture contribution is comparatively small. Far from resonances, the resonance contribution quickly decays, but the tails of strong resonances can extend into energy regions far from the resonance energy where they are comparable in magnitude to direct capture. This often means that at intermediate energies away from resonances both the tail of a resonance and direct capture are significant contributions to the S-factor. Deconvoluting them is especially problematic when the direct capture contribution is small (as it generally is in reactions with large Coulomb barriers) and resonances are close together. Figure 2-3 is a schematic showing the interplay of various resonance contributions and direct capture.

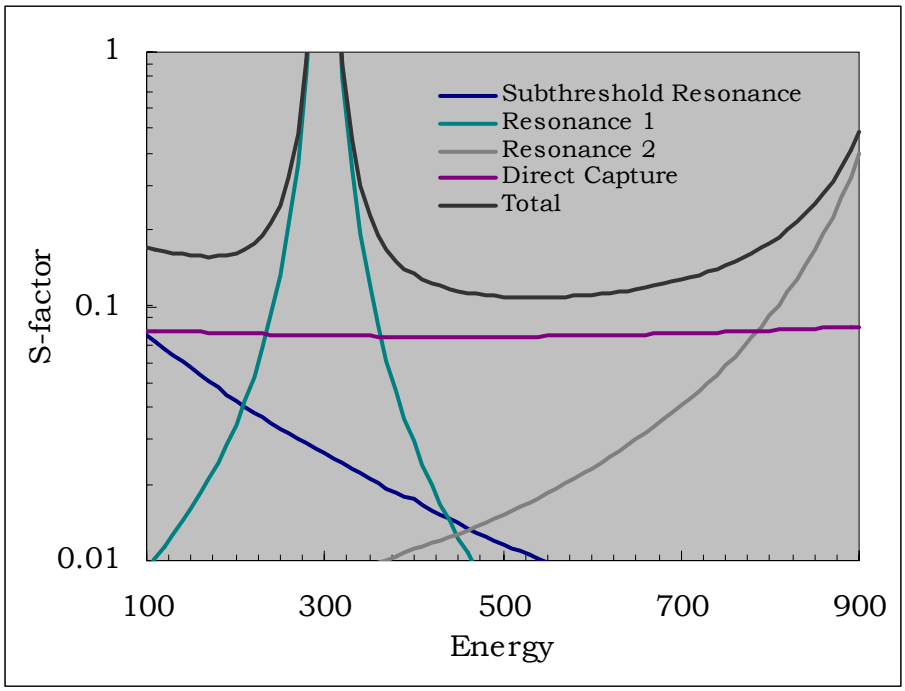

Figure 2-3: Resonance and direct capture

Experimental data, which measure the total contribution from all the components (black line), do not always reveal the underlying reaction mechanism. However, by combing nuclear structure information with experimental data, we can shed light on this mechanism. This is necessary when extrapolating to low energies where measurements are not possible.

Further complicating this picture is the fact that nuclear states are quantum-mechanical systems which exhibit interference. Interference can exist both between resonances and between resonances and direct capture processes. As a result of the complicated nature of nuclear reactions, each reaction is unique and requires careful consideration; some reactions are dominated by resonance capture and some by direct capture. The worst-case scenario exists in the case of proton capture on ^{14}N. Both resonance and direct capture are important contributors to the low energy S-factor and interference plays an important role in at least one transition.

2.2.1. The Direct Capture Model

A smoothly varying S-factor over large energy regions is normally attributed to a single step process where the projectile directly enters a state in the product nucleus by emitting a γ-ray[13]. In this prescription, the incident particle interacts with the target nuclei as a single core and not with individual nucleons. The product nucleus approximately consists of the projectile in a single particle orbit around the target nucleus. Since this process is governed by the interaction of the Coulomb field between the projectile and target, the cross section has a smooth energy dependence described by the barrier penetration probability. This implies a roughly constant S-factor.

Because of the Coulomb barrier, the vast majority of particles elastically scatter. As a result, the direct capture interaction can be treated using first-order time dependent perturbation theory, i.e. the nuclear interaction is a small perturbation to the Coulomb repulsion. Using this model, Tombrello and Parker calculate the direct capture differential cross section to be [Tom62]:

$$\frac{d\sigma}{d\Omega} = \frac{E_\gamma}{2\pi \cdot \hbar^2 \cdot c \cdot v \cdot (2j_p + 1) \cdot (2j_t + 1)} \sum_{m_i, m_f, P} \left| \left\langle f, m_f \left| H_{\text{int}} \right| i, m_i \right\rangle \right|^2 \qquad \text{Equation 2-7}$$

where E_γ is the γ-ray energy, v is the relative velocity between the incident and target nuclei at a large radius, j_p (j_t) is the spin of the projectile (target), and H_{int} is the interaction Hamiltonian.

[13] Disagreement exists as to whether or not direct and resonant capture have differing reaction mechanisms or whether the tails of remote resonances appear as "direct capture".

The interaction Hamiltonian, used in calculating the cross section, depends on whether the particular transition is described by an electric or magnetic operator and its multipolarity. The dominant and most common Hamiltonian contains the E1 operator. For simplicity, I show the final result exclusively for the E1 operator [Rol73].

$$\sigma(E) = 0.071\mu^{3/2}\left(\frac{Z_p}{M_p} - \frac{Z_t}{M_t}\right)^2 \frac{E_\gamma^3}{E_p^{3/2}} \frac{(2J_f+1)(2l_i+1)}{(2j_p+1)(2j_t+1)(2l_f+1)} \left(l_i 010 \middle| l_f 0\right)^2 R^2_{l_i 1 l_f}\, \mu b$$

Equation 2-8

The parameters are as follows:

$Z_p(Z_t)$	projectile (target) atomic number
$M_p(M_t)$	projectile (target) mass number
$E_\gamma(E_p)$	γ-ray (proton) energy
$j_p(j_t)$	projectile (target) spin
$l_i(l_f)$	initial (final) orbital angular momentum
J_f	final state spin
R	radial wave function integral

The radial integral is the overlap of the incoming, continuum wave function (u_c) with the final, bound state wave function (u_b):

$$R_{l_i 1 l_f} = \int_0^\infty u_c(r) \cdot O(E1) \cdot u_b(r) \cdot r^2 dr$$

Equation 2-9

Calculating this integral requires significant assumptions and knowledge about the nature of bound state wave functions. (I describe the exact calculations performed in this work in Chapter 5.)

Although the shape of the theoretical direct capture cross section can be an accurate description of the energy dependence of the experimental cross section, its absolute normalization can not be reliably calculated. This results from the crude assumption that the final state is a single particle bound in a potential well. In reality, the nuclei do not populate pure single particle states, but rather a (small) fraction of the total wave function exists as a single particle state. Spectroscopic factors, or asymptotic normalization coefficients, provide an empirical estimate of the fraction of the wave function in this configuration. They serve as

a normalization factor connecting theoretical calculations to experimental data, which in the case of spectroscopic factors is:

$$\sigma_{\text{experimental}} = \sum_{\ell_i,\ell_f} C^2S_{\ell_f}\,\sigma_{\text{theory}\,\ell_i,\ell_f} \qquad \text{Equation 2-10}$$

where the sum is over all possible final state orbital angular momentum (ℓ_f) and all incident orbital angular momentum (ℓ_i). Despite this sum, the lowest allowable ℓ value normally dominates the low energy cross section.

At first glance the spectroscopic factors appear to be fudge factors, but stripping reactions, e.g. (^{3}He,^{2}H) or (^{2}H,n), provide a completely independent measurement of their value. Stripping reactions have completely different systematic errors when performed at high energies where only direct processes are present. Agreement between spectroscopic factors via stripping experiments and those from normalizing direct capture cross section data provides a check on the validity of the direct capture calculations. States that display no direct capture in the experimental data may have small C^2S values and the direct capture contribution can be ignored[14].

2.2.2. The Resonance Capture Model

In contrast to a slowly varying energy dependence, resonance capture is strongly energy dependent. The cross section near a resonance can vary by many orders of magnitude (10^6) in a small energy range (10 keV). This behavior results from the presence of an excited nuclear state in the product nucleus near the energy of the incident particle. In the resonance capture model, there is strong overlap between the quantum-mechanical state of the two initial nuclei (projectile and target) and the excited compound nuclear state. At astrophysical energies, the excited states of the product nuclei exist at discrete, isolated energies (E_x) each with an energy width (Γ). The initial and final wave functions only overlap strongly when the energy of the initial state (projectile mass, target mass, and kinetic energy) and the final state (product mass and excited state energy) match. This implies that the resonance energies are:

[14] One can not always determine whether or not a direct capture component exists because its presence can sometimes be masked by interference effects. (Section 2.2.3)

$$E_r = E_x - Q$$ Equation 2-11

where Q is the difference in mass between the initial and final states. The total energy width of an excited state is related to its lifetime through the uncertainty principle and is the sum of all partial width contributions from each possible decay channel, e.g. proton, γ-ray, or α emission.

$$\Gamma = \frac{\hbar}{\tau} = \Gamma_p + \Gamma_\gamma + \Gamma_\alpha + \ldots$$ Equation 2-12

The ratio of each partial width to the total width is the probability of that particular process occurring. Therefore, the resonance cross section is a function of the partial widths present in the incoming and outgoing channels and sharply distributed near $E_r \pm \Gamma$. For the purposes of this work, only the proton and γ-ray channels are open, $\Gamma = \Gamma_p + \Gamma_\gamma$.

The exact form of the resonance (proton) capture cross section results from time dependent perturbation theory and a few weeks of writing algebra. If the energy levels in the product nuclei are adequately far apart, i.e. $\Delta E >> \Gamma$, then a single-level approximation adequately describes the contribution from each level. The single-level resonance cross section given by the Breit-Wigner equation is, by analogy to transmission of light through an absorptive medium,[Lan58]:

$$\sigma = \pi \cdot \lambda\!\!\!^{-2} \frac{2J+1}{(2J_p+1)(2J_t+1)} \frac{\Gamma_p(E) \cdot \Gamma_\gamma(E)}{\left(E_r - E - \left[S_c(E) - S_c(E_r)\right] \cdot \gamma^2\right)^2 + \left(\frac{\Gamma(E)}{2}\right)^2}$$ Equation 2-13

where the parameters are defined as follows:

$J_p(J_t)(J)$	projectile (target) (final state) spin
$\Gamma(\Gamma_p)$ (Γ_γ)	total (proton) (γ-ray) *formal* width
$E(E_r)$	proton (resonance) energy
S_c	shift function
$\lambda\!\!\!^{-}$	DeBroglie wavelength

This approximation often describes the resonant contribution accurately over an incredible

range of energies. Reactions with negligible direct capture contributions demonstrate its accuracy, e.g. over 10^6 resonance widths [Rol74]. This is extremely important because astrophysically relevant reactions frequently have small direct capture contributions at low energies. As a result, the tails of higher energy resonances appreciably contribute to, and often dominate, the low energy cross section. Calculating the resonance contribution far from E_r requires accurate and precise knowledge of the parameters E_r, Γ_p, and Γ_γ. The values of E_r can be precisely measured with high resolution accelerators and thus the values of Γ_γ and Γ_p are normally the largest sources of uncertainty.

For a narrow resonance, the (outgoing) wave functions do not vary appreciably over the resonance width. This implies that the difference in the shift functions $[S_c(E)-S_c(E_r)]$ is negligible (since S is the logarithmic derivative of the outgoing/reflected wave function). In a similar manner, Γ_p and Γ_γ are approximately constant. Under these conditions, the Thomas approximation simplifies the resonance description considerably:

$$\sigma(E) = \pi \cdot \lambda\!\!\!^{-2}\,\omega \frac{\Gamma_p \cdot \Gamma_\gamma}{(E_r - E)^2 + \left(\frac{\Gamma}{2}\right)^2}, \omega = \frac{2J+1}{(2J_p+1)\cdot(2J_t+1)} \qquad \text{Equation 2-14}$$

where the widths are the observed widths.

2.2.3. Angular Distributions and Interference Effects

In the simplest case, radiation emitted from an A(p,γ)B reaction results purely from either direct or resonance capture and is emitted in an isotropic fashion. Unfortunately, reactions rarely proceed through such a simple mechanism. First, the angular momentum coupling between the incident particle and target nuclei often enhances the emission of radiation at some angles and reduces it in others. Secondly, the cross section may contain contributions from more than one resonance and also from direct capture. Furthermore, if this is the case, the resonance contributions may interfere with each other or with the direct capture process.

For resonance capture, the angular distribution of the primary γ-ray is [Sha54]:

$$W(\theta) = \sum_k (-1)^{s-I} Z(\ell j \ell' j', sk) \cdot Z_1(LjL' j', Ik) \cdot P_k(\cos\theta) \qquad \text{Equation 2-15}$$

subject to the following constraints:

i) triangle condition: $\max\left[|\ell - \ell'|, |L - L'|, |j - j'|\right] \le k \le \min\left[\ell + \ell', L + L', j + j'\right]$

ii) parity conservation:
$$\ell + \ell' + k = even$$
$$L + \pi + L' + \pi' + k = even$$

where ℓ and s are the incoming particle orbital angular momentum and spin, L and π are the outgoing γ-ray angular momentum and parity, and I (j) is the final (intermediate) state spin. The functions P_k are each Legendre polynomials of order k. For a single resonance, s, ℓ, j = s', ℓ', j'. (The values of Z and Z_1 derived from angular momentum coupling are tabulated in Sharp et al..) For resonances that emit a cascade of γ-rays, the secondary γ-ray distribution is significantly more complex and I do not quote it here.

For direct capture, the primary γ-ray angular distribution only depends on the initial and final orbital angular momentum (ℓ_i and ℓ_f) and the γ-ray multipolarity (L) [Rol73]:

$$W_{DC}^{primary}(\theta) = \sum_k (\ell_i 0\, \ell_i 0 | k0) \cdot \overline{Z_1}(L\, \ell_i\, L\, \ell_i, \ell_f k) \cdot P_k(\cos\theta) \qquad \text{Equation 2-16}$$

where $\overline{Z_1}$ (tabulated by Ferguson [Fer65]) differs from the above Z_1 coefficient and the first term in brackets is a Clebsh-Gordan coefficient. If instead the secondary γ-rays are observed, then the distribution does depend on the states connecting the secondary transition [Rol73]:

$$W_{DC}^{secondary}(\theta) = \sum_k (\ell_i 0\, \ell_i 0 | k0) \cdot W(\ell_i \ell_f \ell_i \ell_f | L_1 k) \cdot W(J_f \ell_f J_f \ell_f | S k) \cdot \overline{Z_1}(L_2\, J_f\, L_2\, J_f, J_e k) \cdot P_k(\cos\theta) \qquad \text{Equation 2-17}$$

where S is the channel spin, J_f and J_e are the spins of the secondary transition f $\rightarrow$ e, and L_2 is the multipole of the secondary γ-ray. This expression assumes a single multipole and, for cases where significant mixing occurs, the sum must be extended over L_2.

Whenever a particular transition involves more than one process, the two or more processes may interfere. Interference effects are not always present and their presence cannot be predicted a-priori. However, when observed in the experimental data, one must consider them. The inference term between any two processes 1 and 2 is:

$$\sigma_{\text{tot}}(\mathrm{E},\theta) = \sigma_1(\mathrm{E})\cdot \mathrm{W}_1(\theta) + \sigma_2(\mathrm{E},\theta)\cdot \mathrm{W}_2(\theta) \pm 2\cdot\sqrt{\sigma_1(\mathrm{E})\cdot\sigma_2(\mathrm{E})}\cdot \mathrm{W}_{1,2}^{\text{int erference}}(\theta)\cdot\cos\left[\delta_1(\mathrm{E})+\delta_2(\mathrm{E})\right]$$

Equation 2-18

where δ_1 and δ_2 are the phase shifts of each contribution. The sign of the interference term is arbitrary and must be derived from the experimental data. The phase shifts differ for resonance and direct capture:

$$\delta_{\text{resonance}} = \arctan\left[\frac{\Gamma(\mathrm{E})}{2\cdot(\mathrm{E}-\mathrm{E}_r)}\right] + \phi_{\text{coulomb}} + \eta_{\text{nuclear}}$$

Equation 2-19

$$\delta_{direct\ capture} = \phi_{coulomb} + \eta_{nuclear}$$

Equation 2-20

where ϕ and η are the nuclear and Coulomb phase shifts and each is a function of the incoming orbital angular momentum (ℓ). The angular distribution for resonances is valid for interference between resonances, i.e. j and j' correspond to the first and second resonance. The γ-ray angular distribution for interference between a resonance and direct capture is given by [Rol73]:

$$\mathrm{W}_{\mathrm{R,DC}}^{\text{int}}(\theta) = (-1)^{\mathrm{P}}\cdot(2\mathrm{J}_r+1)\cdot(2\ell_f+1)\cdot \mathrm{W}(\ell_r \mathrm{L}_r \mathrm{J}_i \mathrm{J}_f \,|\, \ell_f\ \mathrm{J}_r) \sum_k (\ell_r 0\, \ell_d 0 \,|\, k0)\cdot \overline{\mathrm{Z}_1}(\ell_r\ \mathrm{L}_r\ \ell_d\ \mathrm{L}_d, \ell_f\ k)\cdot \mathrm{P}_k(\cos\theta)$$

Equation 2-21

where ℓ_r (ℓ_d) (ℓ_f) refers to the resonance (incident direct capture) (final state direct capture) orbital angular momentum, L_r (L_d) refers to the multipole of the resonance (direct capture) γ-ray and J_r (J_i) (J_f) refers to the resonance (channel) (final) state spin. The phase factor, P, is defined but it is multiplied by an arbitrary sign in the total cross section and thus will be ignored here. For the angle integrated cross section, the angular distribution coefficients serve as normalization factors and predict whether or not two processes interfere.

When numerous resonances or direct capture partial waves contribute to the cross section, each possible pair of contributions can interfere. Numerous contributions with different angular distributions quickly produce a complex cross section especially when numerous interference terms have arbitrary signs. In practice, the interference terms often simplify. For example, when two inferring processes share the same incoming orbital angular momentum, the nuclear and Coulomb phase shifts cancel.

To demonstrate a simple example of interference, the figure 2-4 shows a reaction with direct capture and a relatively weak but broad resonance. Both processes share the same incoming orbital angular momentum.

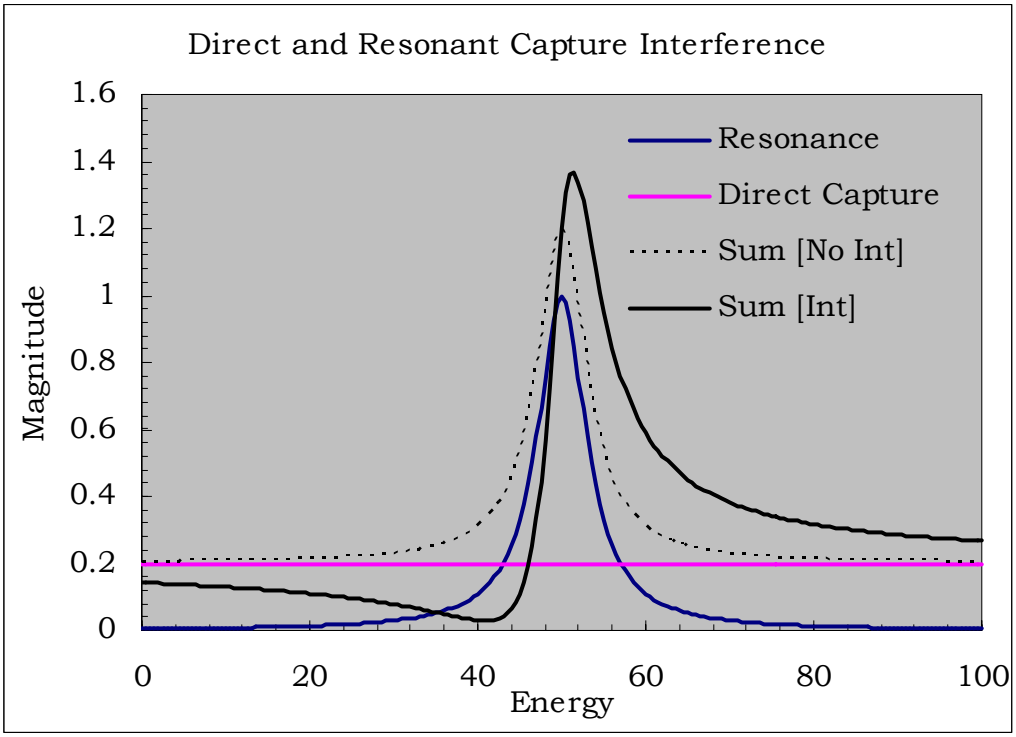

Figure 2-4: Interference between resonance and direct capture

There are a few characteristic features of this interference curve. First, constructive interference occurs on one side of the resonance and destructive on the other. This behavior reverses depending on the sign of the interference term. Second, the interference term diminishes after only a few resonance widths (e.g. 10). This example is somewhat exaggerated because the resonance contribution is normally much larger than direct capture near E_r. But

far away from resonances where the resonance tail and direct capture contribution are similar in magnitude, interference can still have a large impact. For energy regions where one contribution dominates, interference has little effect. The above example is relatively straightforward. When numerous processes are intertwined the picture quickly becomes complex because interference between each pair of components must be considered. This is in fact the case in the $^{14}N(p,\gamma)^{15}O$ reaction.

2.3 The $^{14}N(p,\gamma)^{15}O$ Reaction Mechanism

The $^{14}N(p,\gamma)^{15}O$ low energy S-factor has contributions from numerous states each with its own combination of direct and resonance capture[15]. These states exist at 0 (g.s.), 5183, 5241, 6176, 6793, 6859, and 7276 keV (see figure 2-5). The 7556, 8284, 8743 and 9484 keV states lie above the ^{14}N + p threshold at 7297 keV and result in resonances at 259, 987, 1447 and 2187 keV. The widths, spins, and parities of the ^{15}O excited states dictate the different contributions that may be important for each transition. Figure 2-6, at the end of this section, shows the various processes that contribute to one example: the ground state. Since different processes contribute differently to each state, I examine them individually below.

Previous experiments suggest that direct capture into the 6793 keV state comprises the majority of the low energy S-factor. Additionally, this state is a large branch of the 259 keV resonance. In order to reliably extrapolate the direct capture contribution, it is essential to distinguish between the resonant and direct capture contributions in the experimental data. This requires a complete understanding of the 259 keV resonance and data below 259 keV in order constrain the direct capture contribution.

Extrapolation of direct and resonance capture into the ground state, hereafter referred to as the "ground state transition", to low energies continues to complicate our understanding of this reaction. It is far and away the most uncertain transition and may contribute between zero and fifty-percent of the low energy S-factor. The ground state transition is a small branch of the 259 keV resonance and it also appears to have a significant direct capture component at higher energies. Two other states far from astrophysically relevant energies may also

[15] Throughout this text "low energy" refers to energies below 200 keV.

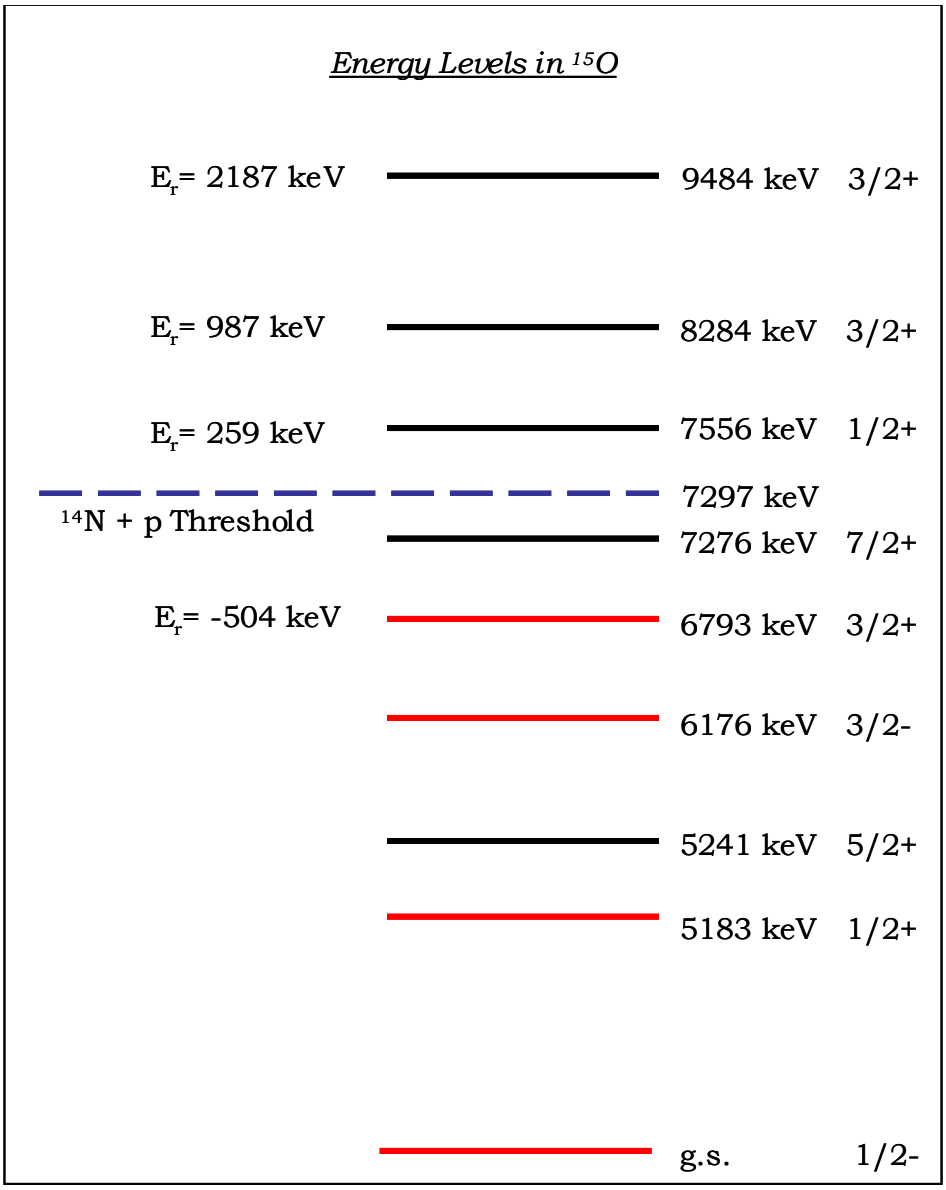

Figure 2-5: Enegy levels in ^{15}O

States shown in red contribute significantly to the low energy S-factor. The blue dashed line shows the reaction Q-value.

contribute significantly. The first is a broad resonance at 2187 keV whose tail remains significant at low energies. The largest uncertainty results from the possible tail contribution of the sub-threshold state located 504 keV below the ^{14}N + p threshold (i.e. the 6793 keV Extrapolation of direct and resonance capture into the ground state, hereafter referred to as the "ground state transition", to low energies continues to complicate our understanding of

this reaction. It is far and away the most uncertain transition and may contribute between zero and fifty-percent of the low energy S-factor. The ground state transition is a small branch of the 259 keV resonance and it also appears to have a significant direct capture component at higher energies. Two other states far from astrophysically relevant energies may also contribute significantly. The first is a broad resonance at 2187 keV whose tail remains significant at low energies. The largest uncertainty results from the possible tail contribution of the sub-threshold state located 504 keV below the $^{14}N + p$ threshold (i.e. the 6793 keV state). Despite being below threshold, the high energy tail of this state extends into the positive energy region. Three factors conspire to possibly make this an important contribution: i) it is relatively close to the threshold, ii) it is a relatively wide state and iii) it has angular momentum $3/2^+$ and proceeds through s-wave capture. As a result, transitions to the ground state may proceed through this tail and contribute in a resonance fashion to the ground state S-factor. States such as this plague extrapolations because their effects are small at energies measurable by experiments. In these cases, only by combining measurements of the state parameters (Γ_γ and C^2S) with experimental data, can limits be placed on their contribution. The principal unknown here is the effect of interference between the various processes. In chapter 5, I discuss how interference between the numerous resonances and direct capture leads to a multi-parameter fit that is difficult to constrain.

Resonances dominate the 5183 and 6176 keV transitions while direct capture comprises most of the 5241, 6859, and 7276 keV S-factors. Each of these states contributes only a small fraction of the low energy S-factor. Since in each case only one process governs the low energy region, their extrapolations are relatively well understood.

Ideally, one could calculate the cross section after identifying the reaction mechanism for each transition. This requires measuring each of the theoretical parameters: C^2S for each state and Γ, $\omega\gamma$, and E_r for each resonance. Precise measurements of these parameters are difficult. Even with precise measurements, difficulties with direct capture calculations and unpredictable interference effects normally necessitate direct measurements. By fitting cross section data using the above variables as fitting parameters, and getting good agreement with their measured values, one gains confidence in calculating the cross section at energies where it can not be measured. It is important to note that the simple theory of assuming direct capture and

Breit-Wigner amplitudes is a gross oversimplification. This model sometimes can not explain the observed data. A second and more sophisticated fitting technique is R-matrix theory, which is beyond the scope of this thesis. Although it has a more complete formalism, the results of different publications vary and sometimes are not convincing. However, agreement between these two fitting techniques justifies confidence in their respective extrapolations. The lack of a reliable extrapolation technique further underscores the necessity of measurements at the lowest possible energies to best constrain the fitting parameters.

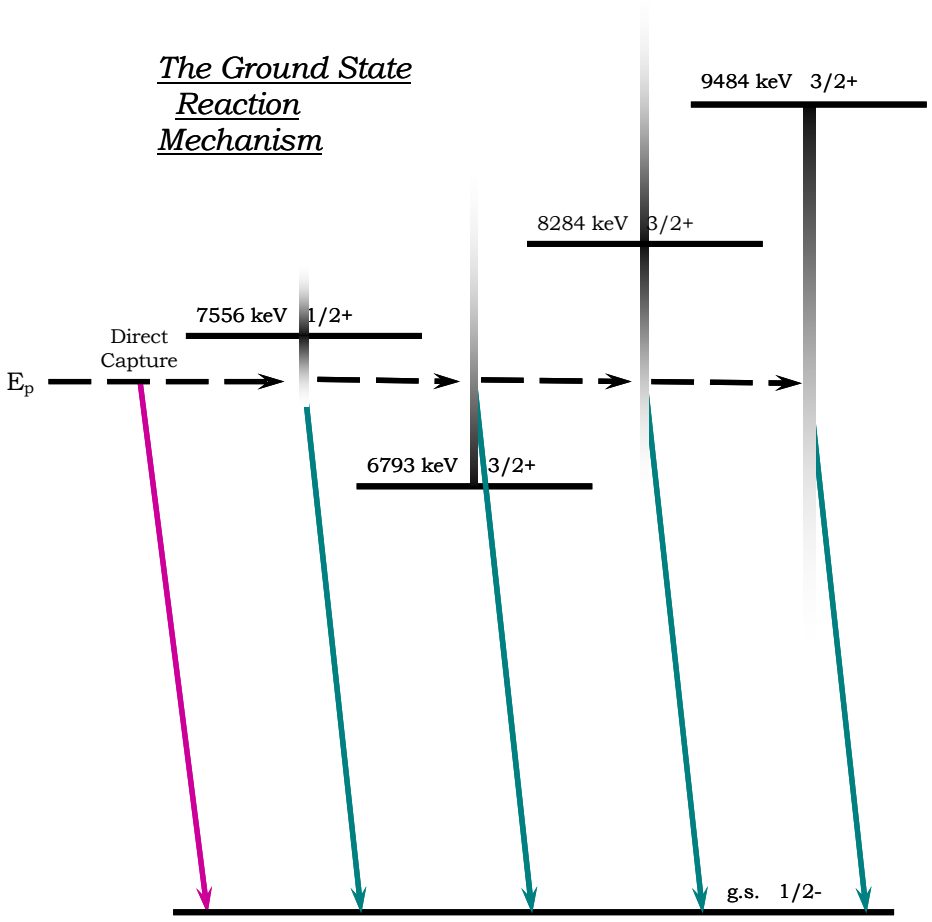

Figure 2-6: The ground state reaction mechanism

Direct capture is shown in purple while resonance processes are labeled in green. The shaded bars reveal the approximate widths of the various contributing resonances.

2.4 Previous Measurements of the $^{14}N(p,\gamma)^{15}O$ S-factor

Due to its importance in hydrogen burning, numerous experiments, dating back to 1957, examined the $^{14}N(p,\gamma)^{15}O$ low energy cross section. The most notable and relevant results to this project are those of Schröder et al. [Sch87] and Lamb and Hester [Lam57]. Indirect work by Bertone et al. of lifetimes [Ber01] and spectroscopic factors from [Ber02] and [Muk03] provide important insight into the reaction mechanism. Measurements of the 259 keV resonance provide an excellent understanding of the partial widths and a check on our systematic errors, [AjS81] and [Bec92]. Also, a recent measurement by Nelson et al. suggests a previously undetected resonance [Nel01]. I discuss all of the above work in the following section. Figure 2-7 at the end of this section displays all available cross section data and extrapolations (at low energies) to date.

Ironically, the lowest energy cross section measurement is also the oldest. Lamb and Hester first measured the S-factor between 100 and 135 keV. Their technique differed significantly from those used in more recent measurements and, although this could provide an independent check, it also raises concerns of systematic errors. They measured the positron emission from the decay of ^{15}O using a photomultiplier tube. TiN targets were bombarded with a 25 mA proton beam for 3 ^{15}O half-lives and then counted for 3 half-lives. The proton current was integrated using calorimetry of the target cooling water which is a difficult technique and prone to systematic errors. Their quoted error of 5% for the beam integration may be significantly low. The second difficulty with a measurement of this type is the target contamination of carbon which also β-decays but with a much larger half-life than ^{15}O. Lamb and Hester addressed this issue in their analysis. Although these two systematic errors raise concern, there is no a-priori reason to question their results. One limitation of this experiment is that it measured the total S-factor and not the contribution of individual states. In determining the S-factor at low energies, it is necessary to extrapolate each individual state because each state has its own reaction mechanism and thus a different energy dependence. A measurement of the total S-factor acts as a constraint on the sum of the individual extrapolations but does not constrain the individual extrapolations directly.

Schröder et al. performed the most complete cross section measurement to date and their extrapolations are the presently accepted values used in stellar model calculations. Unlike the

β-decay measurements of Lamb and Hester, Schröder et al. measured the contributions of each individual state and not solely the total cross section. These data extend over a large energy range from 270 to 3500 keV and are very important for two principle reasons: i) they provide a measurement of direct capture into the 6793 keV state over a wide energy range and ii) they provide a map of the resonant capture contribution to the ground state from the E_p = 259, 987, 2230 and 3210 keV resonances. Although these results do not extend close to energies near the astrophysically relevant region, they are nevertheless crucial in understanding the reaction mechanism. Their angular distribution measurements, which can not be performed at low energies, are important for the analysis of the results of this work. Their technique was similar to that used in the present study, which will be addressed in detail in chapters 3 and 4.

In the analysis of their results, Schröder et al. suggest a strong sub-threshold resonance (Γ = 8.5 eV) contribution to the ground state S-factor. They based these conclusions on fits to ground state data, which imply strong interference between direct capture and the sub-threshold resonance. Furthermore, a strong sub-threshold contribution would be consistent with the results of Lamb and Hester. Schröder et al. quotes an $S_{tot}(0)$ value of 3.20(54) keV·barn. Other analyses of the Schröder et al. data recommend a much larger uncertainty with $S_{tot}(0)$ ranging from 1.9 to 3.9 keV·barn [Adl98]. The abnormally large sub-threshold state contribution could be checked in two ways: by indirectly measuring the width ($\Gamma=\Gamma_\gamma$) of the sub-threshold resonance and by measuring the ground state S-factor at energies where its contribution is clearly discernable.

Two other experiments performed in the energy region 200 to 1000 keV by Pixley [Pix57] and Duncan & Perry [Dun51] vary significantly from the Schröder et al. results. Their data are sparse in this energy region and contain significant scatter. I assume the results of Schröder et al. supercede these older experiments.

As discussed in the previous section, calculating the various resonant and direct capture contributions requires knowledge of their parameters. The most important resonant contributions at low energies are the 259 keV resonance and possible sub-threshold resonance at -504 keV. Bertone et al. determined the width of the -504 keV resonance corresponding to

the 6793 keV state in ^{15}O by measuring its lifetime. Using the Doppler Shift Attenuation Method, they measured the lifetime to be $1.6^{0.75}_{-0.72}$ fs. This corresponds to a total width of 0.041 eV. Since there is no proton channel below the ^{14}N + p threshold, Γ_γ is the only contribution to the width, i.e. Γ(-504 keV) = Γ_γ(-504 keV). This width is significantly smaller than Schröder at al. suggested and reduces the sub-threshold resonance contribution to ground state capture by more than an order of magnitude. This result raises an inconsistency between the lifetime, the Schröder fits and the results of Lamb and Hester. By assuming a large sub-threshold contribution, Schröder et al.'s ground state fits agreed with the low energy data of Lamb and Hester. However, with the recent lifetime measurement, the ground state extrapolation is certainly invalid; this results in the ground state being the most uncertain of all the transitions.

Numerous attempts at measuring the resonance parameters provide an important check on the S-factor extrapolations. The figure of merit here is the resonance strength, which is the resonance cross section integrated over its width (see section 4.2.2). The 259 keV resonance has been measured numerous times most notably in inverse kinematics by Becker et al. (to be discussed in section 4.4). Their value for the resonance strength, 14 ± 1 meV, is the presently accepted value. Schröder et al. measured the 259 keV resonance width to be 0.99 ± 0.10 keV which, though slightly lower than previous results, is the accepted value [AjS81]. Similar, but less precise, knowledge of the 987 and 2087 keV resonances also exists [AjS91]. Other important information, relevant primarily to direct capture calculations, comes from measuring spectroscopic factors. Then newest study by Bertone et al. provides spectroscopic factors for all the relevant states except the 8284 and 9484 keV states which have not been measured to date. The following table shows a summary of these results.

In contrast to past measurements, Nelson et al. reported preliminary evidence for a previously undiscovered resonance at an energy of 119(2) keV. This corresponds to a new energy level in ^{15}O at 7414(2) keV. They reported observing a single γ-ray transition to the ground state and assigned the new level a spin and parity of $1/2^-$ based on shell model arguments. The proposed resonance strength of 4.5(9) μeV would have a very significant impact in main-sequence hydrogen burning in massive stars near 100 million K. These

Direct and Resonant Capture Parameters for States in ^{15}O				
State	C^2S		Γ^{obs}(keV)	$\omega\gamma$(eV)
g.s.	1.7(4)[a]	1.5(2)[c]		
5183 keV	0.0049(15)[a]			
5241 keV	0.094(20)[a]	0.073(7)[c]		
6176 keV	0.050(11)[a]	0.054(6)[c]		
6793 keV	0.51(11)[a]	0.66(17)[c]	41(19)E-05[d]	
6859 kev	0.61(13)[a]	0.54(7)[c]		
7276 keV	0.66(14)[a]	0.71(05)[c]		
7556 keV	0.82(18)[a]		0.99(10)[e]	0.014(1)[e]
8284 keV	0.014[b]		3.9(7)[e]	0.31(4)[e]
8743 keV	0.052[b]		34[e]	0.093(20)[e]
9484 keV	0.19[b]		191[e]	6.1(13)[e]

a) From [Ber02].
b) Calculated from Γ.
c) From [Muk03].
d) From [Ber01].
e) From [Ajs91].

Table 2-2: Previously measured resonant and direct capture parameters

temperatures primarily exist in (super)massive stars and the resulting increase of a factor of 30 in the reaction rate would greatly lower their lifetimes. For this reason, it was crucial for us to confirm the existence of this resonance.

Despite the numerous experiments and tremendous effort invested into measuring the $^{14}N(p,\gamma)^{15}O$ reaction, an absence of experimental data remains at astrophysically relevant energies. Due to the minuscule cross sections involved, there will not be any measurements below ~ 50 keV in the near future. As a result, it will remain necessary to have a sound theoretical understanding of the reaction mechanism in order to extrapolate the present and future data into this energy region. The published fits to existing data demonstrate the difficulty of this task. Three groups predict significantly different results especially for the ground state transition. The fit by Schröder et al. used a combination of direct capture and Breit-Wigner amplitudes. Two R-matrix fits performed by Angulo et al. [Ang01] and A.

Mukhamedzhanov et al. [Muk03] are consistent with the 6793 keV lifetime and predict similar low energy S-factor values but their ground state interference features differ significantly. This is especially true in the astrophysically important region below 100 keV. This disagreement mandates that new data be taken closer to the astrophysical region in order to constrain the fitting parameters. The figure 2-7 shows all of the available previous S-factor data and fits for the ground state and total S-factor. In addition to the previous fits, I show a calculation of the ground state S-factor assuming the parameters listed in table 2-2 and no interference or direct capture.

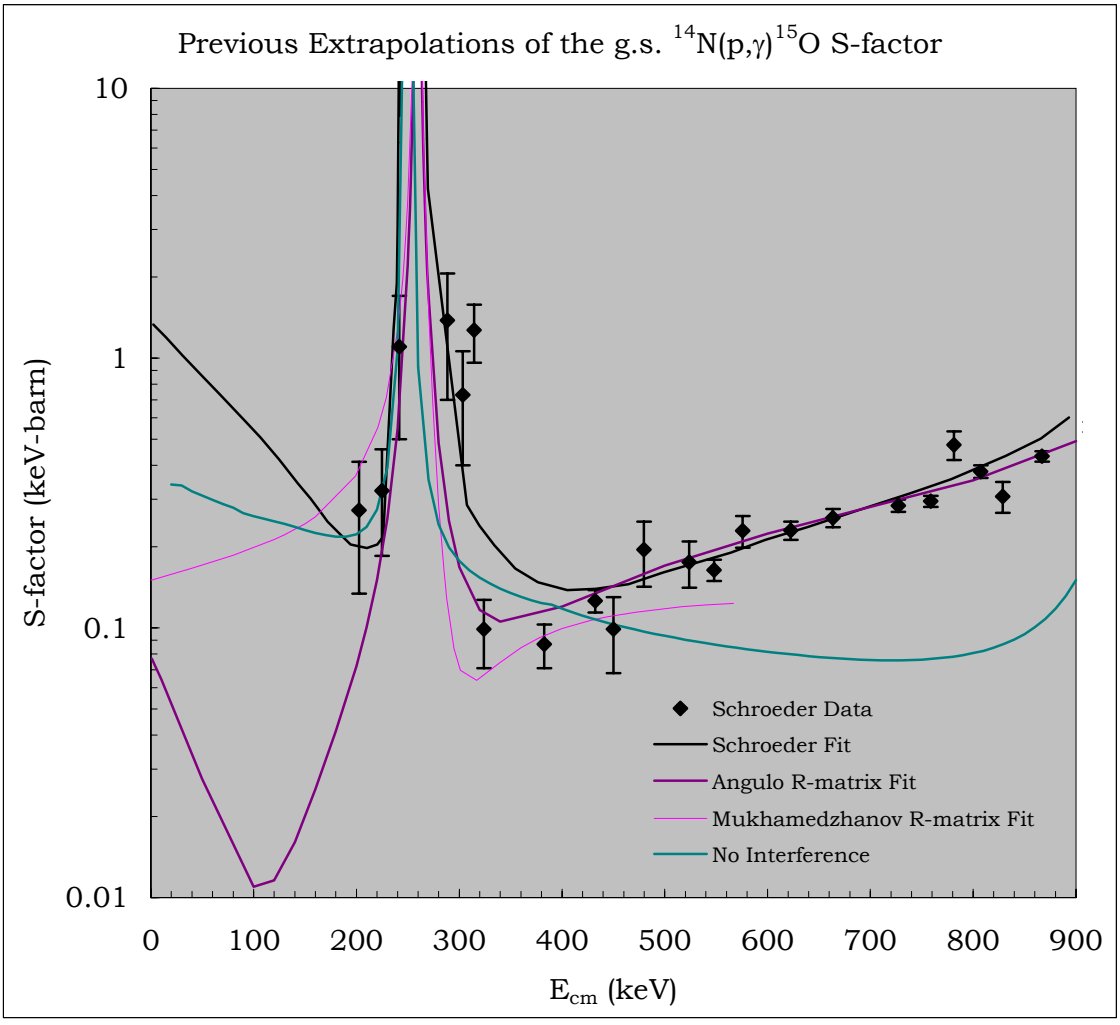

Figure 2-7: Previous ground state S-factor results

In order to constrain the fits at low energies, precise data in this region is necessary. Presently, the fits diverge by more than an order of magnitude.

2.5 The Project Goal

An examination of the previous work on $^{14}N(p,\gamma)^{15}O$ considerably illuminates the reaction mechanism and at the same time highlights a number of problems. Each transition shows a different combination of reaction mechanisms. Assuming a smaller ground state contribution than Schröder et al suggest, the 6793 keV transition is by far the largest contributor to the low energy S-factor. It is dominated by a large direct capture contribution that smoothly varies between the lowest energy data and 2500 keV; there is no apparent contribution from the 987 keV resonance. The 259 keV resonance dominates the well- understood 5183 and 6176 keV transitions which appear to have a negligible direct capture component. Chaos best describes the ground state transition where there is no consistency in the fits and a complete lack of low energy data, i.e. data with small enough uncertainties to constrain a fit. It is unclear whether there is a direct capture contribution or whether the S-factor is dominated by resonances and possible interference.

Presently, the largest problem with the low energy S-factor comes from Nelson et al. who place a resonance directly on top of the Lamb and Hester data. The second is an absence of significant data below the 259 keV resonance for any transition. The third is a large uncertainty in understanding the direct capture and sub-threshold contributions to the ground state. The R-matrix fit of Angulo et al. shows interference effects just above the 259 keV and 987 keV resonances but the low density of data points in this region weakly constrains the fit. Additionally, the Angulo et al. fit of the 6793 keV transition, which is 90% of the S-factor, shows a normalization problem likely due to the absence of data below 259 keV.

In light of these issues, we established four principle goals of this project:

1) Search for the resonance reported by Nelson et al..
2) Measure possible interference effects in the ground state S-factor between 300 and 500 keV. (Measuring the ground state transition implies measuring the others since it is the weakest in this region.)
3) Measure all states below the 259 keV resonance down to 200 keV.
4) Measure the 6793 keV transition down to the lowest possible energy.

Most importantly, these measurements should greatly reduce the uncertainty in the ground state and constrain the direct capture normalization at low energies in the 6793 keV transition.

Chapter 3:

The Laboratory for Experimental Nuclear Astrophysics

3.1 Purpose, Design and Construction

Low energy cross section data are the primary nuclear physics input into stellar models. We frequently can not measure cross sections at energies that overlap with those existing in stellar environments. It is therefore our greatest experimental challenge is to push these measurements to the lowest possible energies. The Laboratory for Experimental Nuclear Astrophysics (LENA) was designed to measure proton capture reactions at the lowest possible energies and its form precisely follows this function.

The limiting factor in measuring low energy cross sections is the experimental count rate. In general, the count rate (N) is given by:

$$N = I \cdot \sigma \cdot n_t \cdot \eta \qquad \text{Equation 3-1}$$

where I is the incident beam current, σ is the reaction cross section, n_t is the number of target nuclei per unit area, and η is the detection efficiency. Designing an experiment to measure low energy cross sections means maximizing I, n_t, and η. The target best suited for cross section measurements differs between reactions and therefore can not be maximized in a general manner. This leaves I and η as the crucial design parameters. Maximizing the beam current is relatively straightforward and requires designing a powerful ion source. However, low counts rates result in long experiment lifetimes which demand stability and reproducibility, in addition to maximal output. Maximizing the detection efficiency is a significantly more complex problem. Each experiment requires individual consideration but generally three main

strategies are involved: i) a large intrinsic detection efficiency, ii) placing the detector as close as possible to the source (target), and iii) minimizing background contamination.

Low energy cross section measurements are challenging because small count rates can produce large statistical uncertainties. In addition to, and because of this, it is vitally important to reduce systematic errors. For example, one of the largest systematic errors results from determining the number of active nuclei (n_t) present in the target. Targets degrade with time as they are subject to proton bombardment. This degradation can be monitored using well studied resonances which normally occur at higher energies, i.e. E > 200 keV. These resonances provide large counts rates and allow the state of a target to be determined quickly. This technique forms the basis of LENA's coupled accelerator design.

LENA consists of two proton accelerators, an ECR ion source mounted on a high voltage table and a JN Van de Graaff accelerator, coupled to a common analyzing magnet and target assembly. Figure 3-1 shows an overhead view of the laboratory. The ECR ion source produces proton currents up to 2 mA at energies between 0 and 200 keV. The Van de Graaff accelerator produces proton currents up to 180 μA at energies from 100 to 1000 keV. Fieldpoint modules provide an interface between the LabVIEW control system and hardware. A shared analyzing magnet directs either proton beam onto the target which is viewed by a large volume High Purity Germanium detector placed within a NaI annulus and lead shield. The detector signals enter NIM and VME electronics modules which are interfaced with a LINUX data acquisition system through a VME on-board computer. I discuss each of these components in detail below.

Construction of LENA began in 1996, but the necessary utility work was not completed until shortly after I joined the project in the fall of 1998. Since then, we have come a long way (compare figure 3-2 and 3-3). At the time of this writing, it is almost fully functional. Numerous people assisted in the design and construction of LENA including (alphabetically): B. Carlin, A. Champagne, C. Iliadis, C. Fox, R. Longland, R. O'Quinn, J. Pollanen, R. Runkle, A. Stephan, C. Westerfeldt, and J. Wills. It is important to note that LENA does not have a devoted technical staff and only a small group of people accomplished the vast majority of the design, assembly, calibrations and troubleshooting including A. Champagne, J. Pollanen, R. Runkle and A. Stephan.

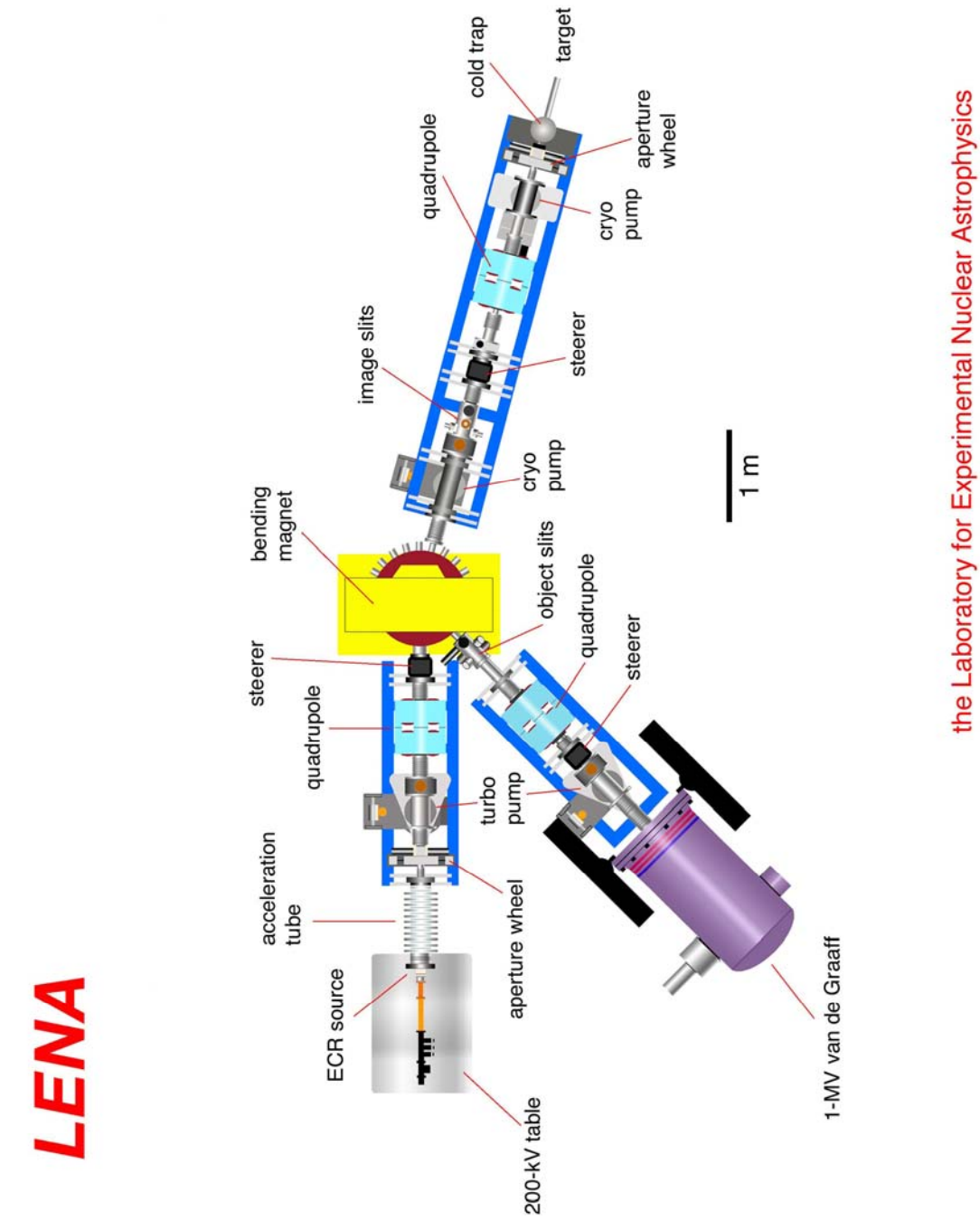

Figure 3-1: LENA shematic

Figure 3-2: LENA construction - September 1999

This photograph shows the state of LENA when I joined the project. The daunting task of assembling two accelerators, the entire vacuum system and target assembly lies ahead. Thanks to my total lack of experience, I acquired an immense amount of knowledge.

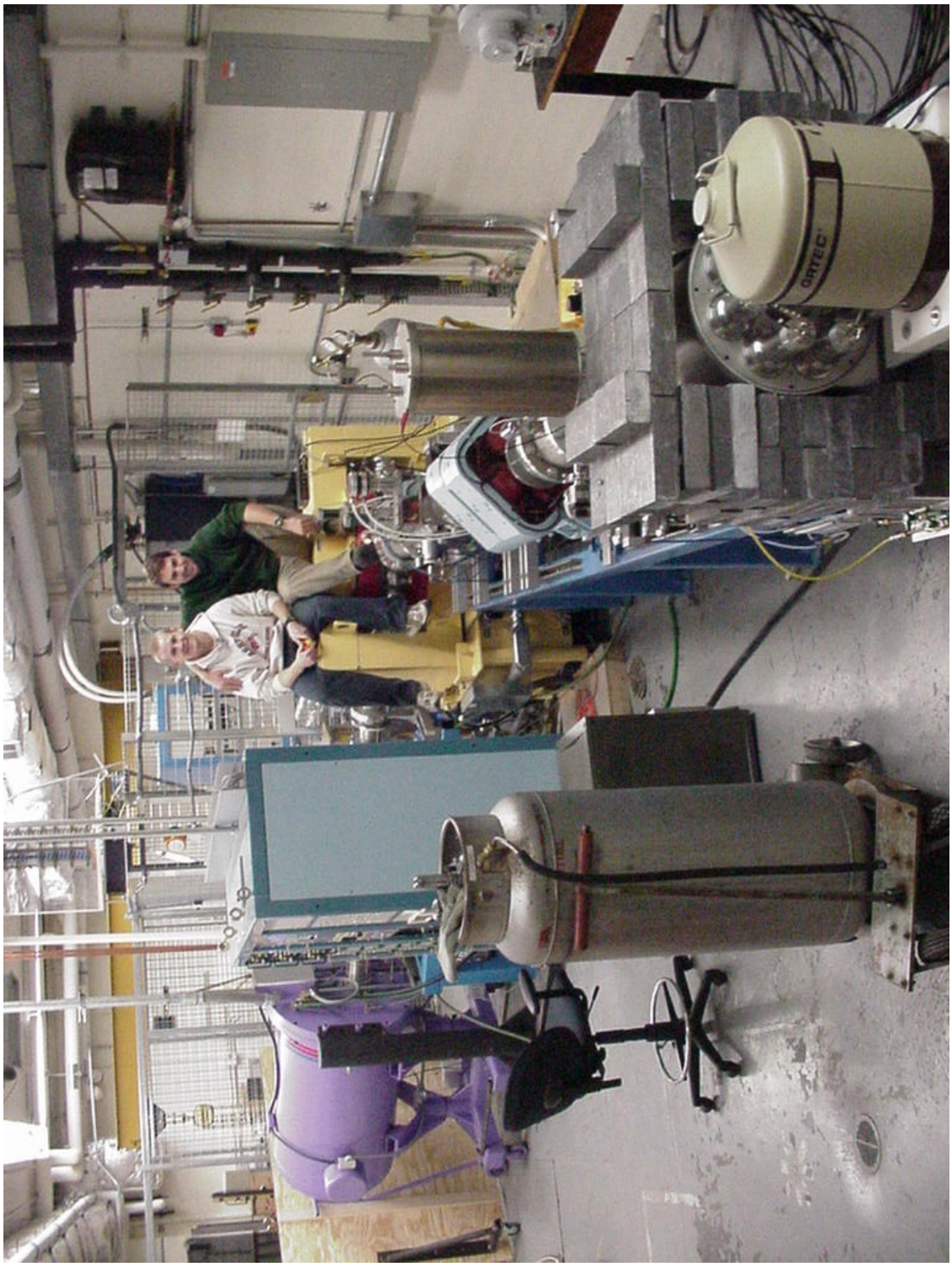

Figure 3-3: LENA construction - January 2003

The two accelerator junkies shown in this picture are Johannes Pollanen and I. This picture shows a fully assembled LENA, just a few bugs to work out yet.

3.2 The Accelerators

3.2.1. JN Van de Graaff

The JN Van de Graaff accelerator (hereafter referred to as JN) consists of an isolated terminal raised to high voltage by a motor-driven charging belt. The insulating belt strips electrons from a charging screen at the terminal and deposits them at the positively biased screen located on the baseplate. A 400 Hz alternator attached to the charging belt powers the terminal which contains four circuits: rf-power, gas leak, extraction electrode, and focus electrode. The radio frequency circuit is a 4 tube 80 W oscillator coupled to an evacuated plasma bottle by two metal leads spaced ~5 cm apart. Two tuning capacitors match the impedance of the 125 MHz rf circuit to the source bottle. Maximizing the coupled rf power maximizes the beam current. After bleeding in H_2 gas and striking a deep red hydrogen plasma, a positively charged electrode extracts the beam from the source bottle into the (de)focus electrode. Under normal operating conditions the extraction and focus electrode are kept at +2.1 and -17.0 kV. The ion source produces proton beams up with currents up to 180 μA and energies between 100 keV and 1000 keV, though normal beam currents range between 100 and 120 μA. The beam output is strongly dependent on the cleanliness of the source bottle.

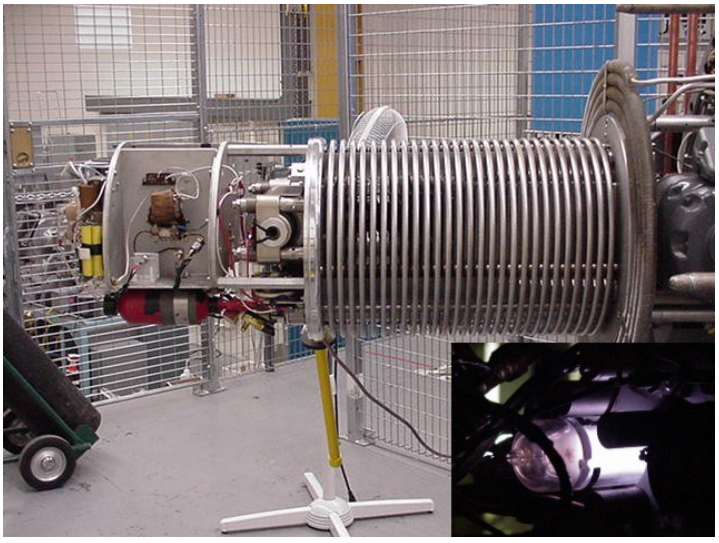

Figure 3-4: JN accelerator and plasma bottle

LENA acquired components of the JN from various universities including Duke University, the California Institute of Technology, and the University of Connecticut. The entire terminal has been reconstructed and is now controlled remotely by stepper motors and power supplies integrated into the LabVIEW control system. During operation, a Terminal Potential Stabilizer (TPS) regulates the terminal potential using a slit control feedback mechanism fed by currents measured at the exit of the analyzing magnet. The field of the analyzing magnet controls the beam energy, which is proportional to the square of the magnetic field ($E_p = k \cdot B^2$). We calibrated the proton beam energy and magnetic field using well known narrow resonances in $^{26}Mg(p,\gamma)^{27}Al$ and $^{27}Al(p,\gamma)^{28}Si$; the table 3-1 lists their resonance energies[16]. The best fit k value[17] is 6088(6) keV/T^2 (see figure 3-5). Direct capture of $^{12}C(p,\gamma)^{13}N$ provided an independent check on the energy calibration and assured its accuracy to within ± 2 keV. We determined the beam resolution using aluminum resonances by subtracting the energies at the ¾Y_{max} and ¼Y_{max} points of their yield curves. The average resolution is 0.7% E_p, e.g. 2 keV at E_p = 300 keV.

Reaction	$E_{resonance}$	Source
$^{18}O(p,\gamma)^{19}F$	150.9 ± 0.2	[Bec95]
$^{27}Al(p,\gamma)^{28}Si$	222.7 ± 0.4	[Uhr85]
$^{26}Mg(p,\gamma)^{27}Al$	292.06 ± 0.09	[Uhr85]
$^{27}Al(p,\gamma)^{28}Si$	293.08 ± 0.08	[Uhr85]
$^{27}Al(p,\gamma)^{28}Si$	326.97 ± 0.05	[Uhr85]
$^{26}Mg(p,\gamma)^{27}Al$	338.4 ± 0.1	[End90]
$^{27}Al(p,\gamma)^{28}Si$	405.44 ± 0.10	[Uhr85]
$^{26}Mg(p,\gamma)^{27}Al$	453.8 ± 0.1	[End90]
Note: Energies given in the laboratory frame.		

Table 3-1: Calibration resonance energies

[16] All of the energies listed in the discussion of LENA are in the laboratory reference frame.

[17] This value depends on the X-steerer setting. In this case, the current was -0.5.

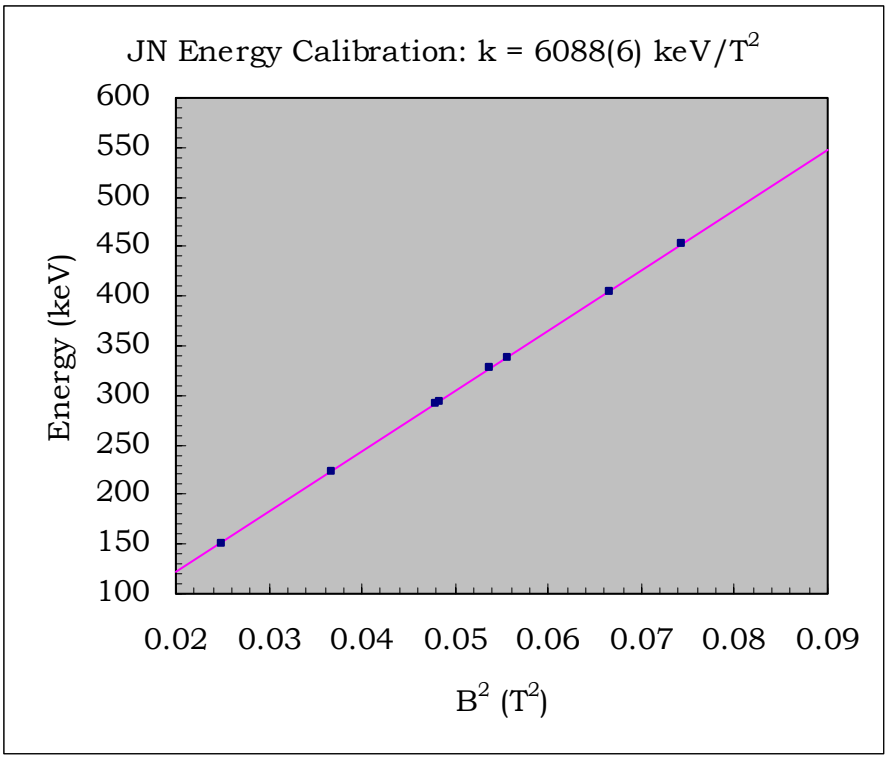

Figure 3-5: JN Van de Graaff energy calibration

3.2.2. 200 kV Accelerator

The 200 kV accelerator consists of a compact ECR ion source mounted on an electrically isolated table attached to a 200 kV power supply. RF power is supplied by a 2.45 GHz magnetron power supply coupled to an evacuated plasma chamber through a waveguide. The magnetron is protected from reflected microwaves by a circulator and dummy load. The microwaves enter an evacuated plasma chamber through a transparent aluminum-nitride window. The plasma chamber contains low pressure H_2 gas (~ few Torr) in an 875 gauss axial magnetic field provided by a samarium-cobalt permanent magnet. A small number of free electrons absorb the microwaves and enter circular orbits around the axial magnetic field. These free electrons ionize H_2 molecules and begin an avalanche, producing a plasma. The Electron Cyclotron Resonance source is so named because the microwave frequency and magnetic field satisfy the resonance condition:

$$B = \frac{2\pi \cdot m \cdot f}{e}$$ Equation 3-2

where f is the microwave frequency, m is the proton mass, and e is the proton charge. For 2.45 GHz, the magnetic field of 875 gauss satisfies this condition. Our magnetic field is roughly constant throughout the magnet (figure 3-6).

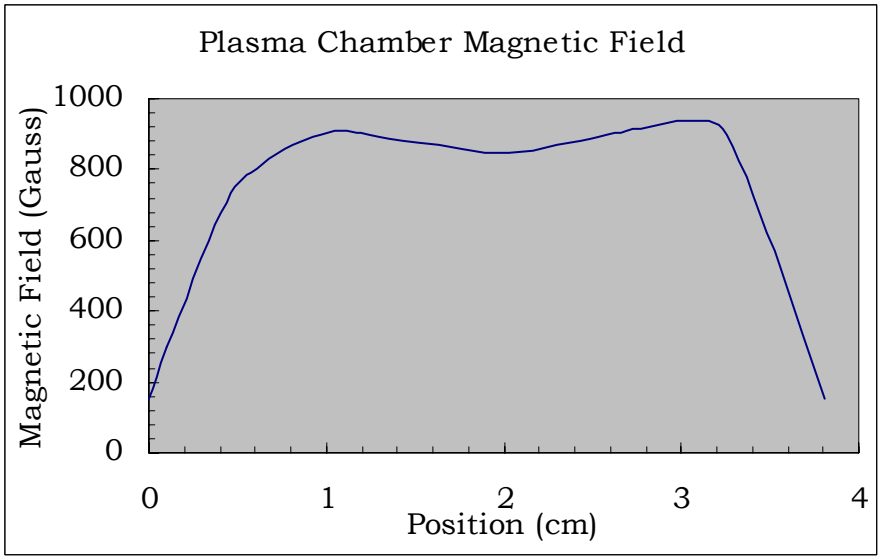

Figure 3-6: Magnetic field of the plasma chamber for the ECR source

Plasma formation occurs after matching the waveguide and plasma chamber impedances with the 3-stub tuner. We observe this when the reflected power precipitously drops to approximately zero as measured by the circulator. After striking the plasma, two electrodes – acceleration and deceleration – extract beam from the chamber (see figures 3-7 and 3-8). The acceleration lens extracts and focuses the beam while the deceleration lens defocuses the beam before it enters the acceleration tube. For further focusing/defocusing there is a focus electrode at the beginning of the acceleration tube, which provides an acceleration (deceleration) gap of up to 15 (-5) kV.

After initially tuning the waveguide at the (grounded) 200 kV table, the magnetron, gas leak, and power supplies are all controlled remotely using LabVIEW. This control system is powered through an isolation transformer (200 kV maximum); fiber optics allow LabVIEW to communicate with the field point modules at high voltage.

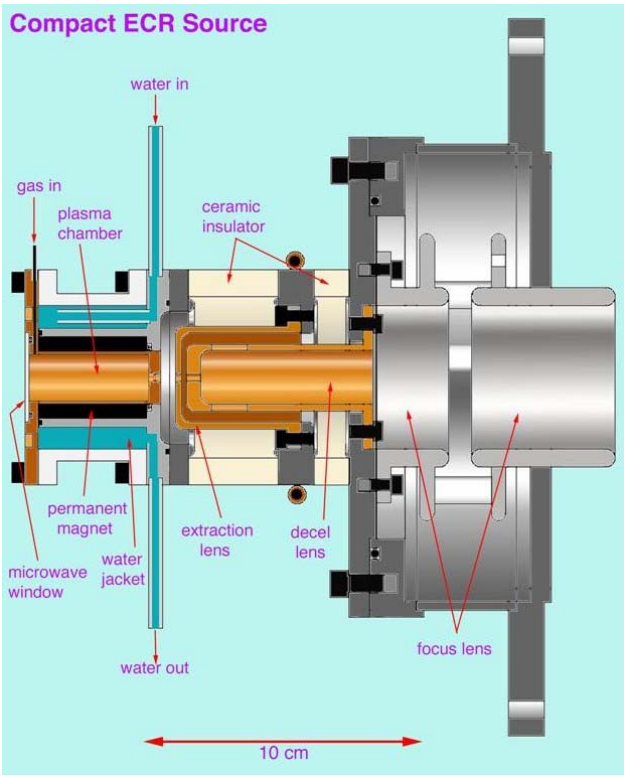

Figure 3-7: ECR source schematic

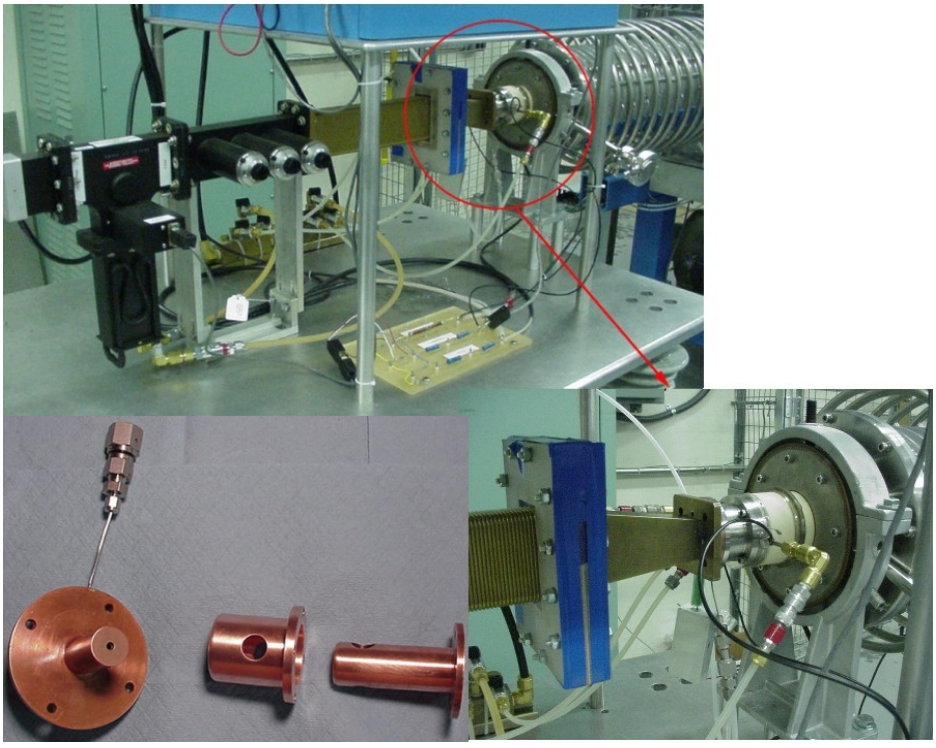

Figure 3-8: ECR source and electrodes

3.3 Beam Optics

Art Champagne designed the beam optics for both accelerators. Coupling two accelerators with different optical properties to a common analyzing magnet and target beam line is a challenge. The objective is to transport both a relatively small sized, high energy, low current beam from the JN an also transport a large sized, low energy, high current beam from the 200 kV accelerator while using the same optical instruments on the target beam line. In each case, the goal is to have a circular beam spot of approximately 1 cm diameter on target. The optical nature of each beam differs significantly. The JN beam has a waist point before and after the analyzing magnet. In contrast, the 200 kV beam remains largely parallel throughout its transport from source to target in order to reduce space charge effects (see figure 3-9). This problem is demonstrated in a simulation of the beam optics shown below. Despite this challenge, the beam optics are very good. Very little beam is lost in the transport process and the user has wide latitude in the tuning parameters. This is demonstrated in the ability to tune the JN beam into almost any shape, which initially burnt up a number of our targets! (The results of a horizontal line tune are shown in figure 4-1.)

The beam optics demand precise alignment of all optical components including the accelerator tubes, quadrupole magnets, slits, apertures, and the analyzing magnet. Each beam line has one quadrupole and one steering magnet. The target beam line contains a slit box whose alignment is crucial for the JN beam control and calibration. We aligned all of the components to a typical accuracy of less than a millimeter. For the quadrupole magnets, magnetic paper indicated the optical center which differs from the spatial center (which is normally used). The alignment procedure required tedious concentration and sitting in the dark for many hours.

As was typical during the construction of LENA, there were a number of surprises along the way. For example, upon opening the analyzing magnet for alignment, we discovered that it was not circular but rather pie shaped. With such a magnet, we could not obtain the correct radius of curvature for the JN beam. Thus, the addition of a shim was necessary (figure 3-11).[18]

[18] We received quality advice on the solution to this problem from A. Zeller of the NCSL at Michigan State University.

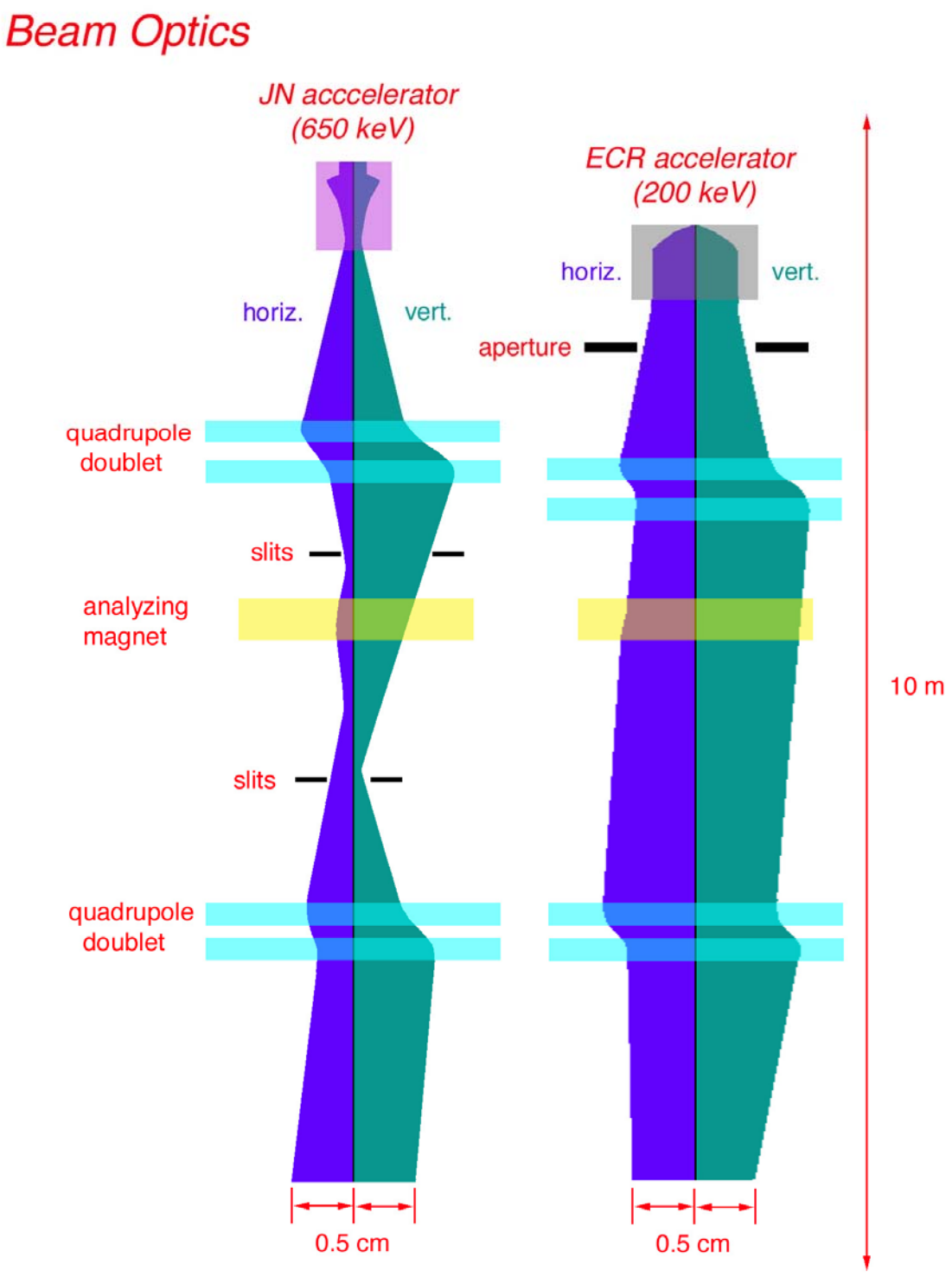

Figure 3-9: Beam optics simulation

Figure 3-10: Aligning the optical instruments

Alignment of all the beam optics components was a challenge that required sitting in the dark for many hours. The left hand photo shows the magnetic field at the center of a quadrupole focusing magnet. The right hand photo shows me looking through the scope.

Figure 3-11: Analyzing magnet before and after the shim

3.4 LabVIEW Control System

One crucial requirement for the design of LENA was ease of use. The long experimental timeframes require numerous operators of the accelerator with varying levels of experience. To make LENA as user friendly as possible, the software package LabVIEW, running on a PC, controls almost the entire accelerator system. The LabVIEW environment allows the operator to simultaneously monitor the status of all components of the accelerator, beam transport and vacuum systems. All accelerator and beam optics control is accomplished using four assignable knobs. The startup and shutdown functions are automated such that, for example, a long term shutdown of the entire lab requires pressing three buttons and turning two keys.

Figure 3-12: LabVIEW control system

FieldPoint modules and stepper motors are the connection between LabVIEW and the laboratory hardware. Various input modules monitor beam currents, power supplies, magnetic fields, vacuum gauges, and radiation monitors. Similarly, various output modules provide control voltages and logic functions. The control PC is isolated from the hardware by FieldPoint modules and fiber-optic connections. This prevents voltage transients from damaging the PC and allows control of FieldPoint modules located on the 200 kV platform.

Contrary to popular criticism, the control PC, running Windows95, has never crashed during operation.

3.5 Target Setup

The targets used in this and most experiments consist of a metal backing (e.g. Ta) with the target nuclei implanted or evaporated onto the front of the backing. The beam spot is restricted to a circle of ~1.5 cm in diameter by two circular apertures; the target backings are approximately 4 cm by 4 cm. Metal backings allow for direct chilled water cooling (10° C) of the target to prevent loss of target material upon excessive heating by the beam.

Absolute cross section measurements require accurate integration of the beam current on target. We accomplish this by electrically isolating the target backing and its holder using rubber o-rings, non-metallic vacuum components, and de-ionized cooling water. Surface electrons may be ejected from the target upon beam bombardment; in order to prevent the loss of these electrons, a copper ring placed approximately 1 mm from the target is biased to negative 300 Volts. This not only prevents secondary electrons from leaving the target but also prevents electrons and charged particles created at slits and apertures from drifting onto the target. The target holder is connected to a charge integrator which outputs 1 pulse/μC to a scalar module. We checked the reliability of the beam integration setup by measuring well known resonance strengths. Although this is a check of the combined accuracy of the beam integration and detection efficiency, the photopeak efficiency was calibrated to an accuracy of a few percent the relevant energy region. For the resonance at a proton energy of 405.5 keV in ^{27}Al(p,γ)^{28}Si, our resonance strength measurement of 8.3(2.0)[19] meV compares well with 8.63(52) from Powell et al. [Pow98].

Eliminating sources of background is vitally important in low count rate experiments. One potential source of background is surface contamination from residual gas in the vicinity of the target. This is especially problematic when the target is sufficiently heated by large beam currents. The most common contaminant is carbon which, as shown in figure 3-14, can render a target useless. Minimizing contaminant build-up requires maintaining the best

[19] The large uncertainty results from massive sum corrections.

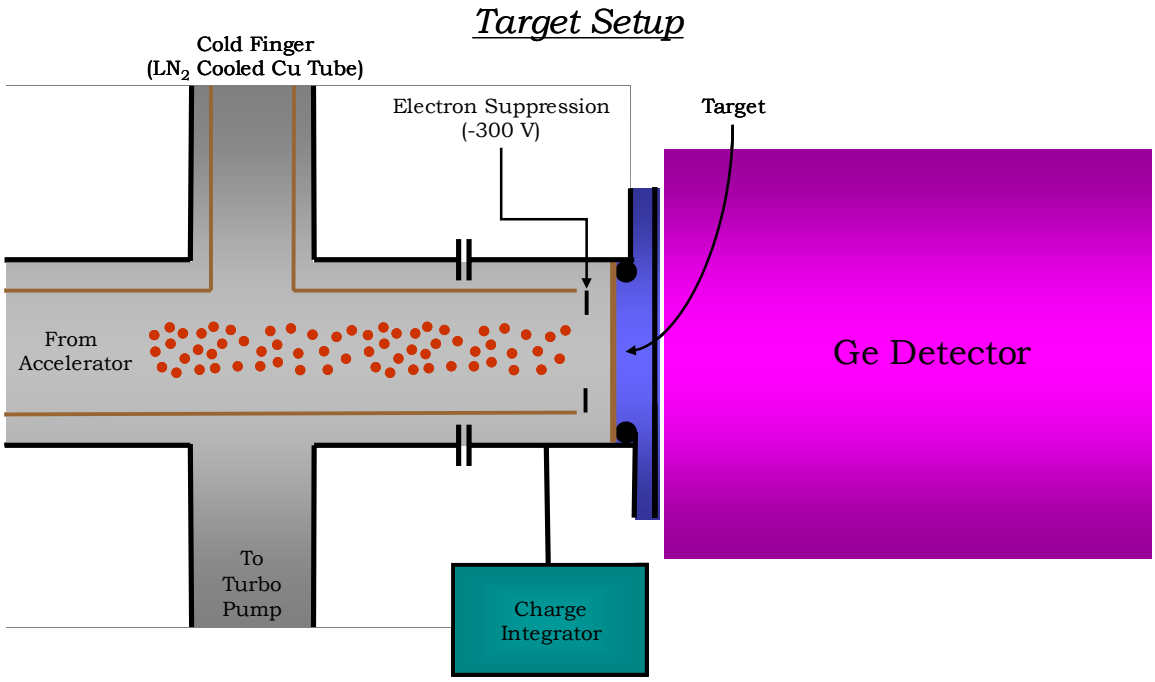

Figure 3-13: Target setup

possible vacuum in the target region. We use three methods to provide a good target vacuum: cryogenic pumps in the target beam line along with a compact turbo pump and liquid nitrogen cooled cold trap placed as close to the target as possible. Cryogenic pumps reduce the concentration of oil vapor in the vacuum system normally generated from turbo pumps. (No compact cryogenic pumps exist that could fit in close geometry to the target.) The cold trap is a copper tube through which the beam passes that is connected to a LN_2 bath. The vacuum at the target with (without) the cold trap is typically low 10^{-7} (low 10^{-6}) torr.

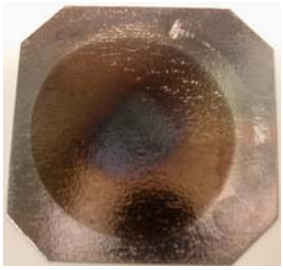

Figure 3-14: Carbon burned target

The brown circular region shows where ^{14}N was implanted into the tantalum backing. The darkened center region results from Carbon build-up on the target.

3.6 Detector System

3.6.1. Detection Scheme

In most cases, measuring the cross section of an A(p,γ)B reaction involves detecting the outgoing γ-ray. This is because the recoil nucleus, B, normally remains in the target while the emitted high energy γ-ray, i.e. > 500 keV, easily penetrates the stainless steel target holder and escapes into the surrounding environment. Therefore, the target-detector setup must maximize the γ-ray detection efficiency. This involves three strategies: i) maximizing the intrinsic detection efficiency, ii) minimizing the source to detector distance and iii) minimizing the contaminant background.

The vast majority of γ-rays interacts with the detector through Compton scattering and leaves only a fraction of their total energy. Ideally, the continuum of Compton scattered γ-rays from the reaction of interest could be counted, but these γ-rays can not be distinguished from those of background sources. Detection of full-energy γ-rays is less efficient but provides a unique signature of the parent reaction. Therefore, in LENA experiments the full-energy γ-rays are of primary interest and it is imperative to identify them. We use a large volume (135%) high purity germanium (Ge) detector for this task. This provides the best compromise between photopeak (full-energy peak) efficiency and energy resolution, which allows accurate photopeak identification. (The energy resolution is, for example, 4 keV at FWHM for a γ-ray energy of 7000 keV.) This detector maximizes the intrinsic detection efficiency at the price level our grant could afford!

The target setup shown in figure 3-13 minimizes the distance from the target to the outside of the vacuum system (~ 9 mm). This allows the face of the Ge detector to be located as close as possible to the target, while still keeping the target directly water cooled. The distance from the target to the face of the detector is 10(1) mm which is small relative to the Ge crystal (diameter ~9 cm). Although close geometry is necessary in order to maximize detection efficiency, the cost is a significant amount of coincidence summing. Coincident summing occurs when two γ-rays deposit energy in the detector within the resolving time of the electronics. The result is a count at the sum of their total deposited energy and a count lost at the energy deposited by each individual γ-ray. For example, the full-energy peak efficiency

for a ^{60}Co source, which emits two coincident γ-rays, is decreased by approximately 15%. I discuss this issue in detail in Chapter 5.

Reducing background is the most complex aspect of the detection system. The sources of background include environmental radiation, cosmic ray sources, and beam induced sources, each having their own energy dependence. The environmental sources are mainly ^{40}K (1461 keV γ-ray) and ^{208}Tl (2614 keV γ-ray). The Compton scattering of these two γ-rays creates a continuous background below 2614 keV and makes photopeak identification difficult in this energy region. The cosmic ray background mainly results from the scattering of very high energy γ-rays, muons, and neutrons. They leave a relatively constant amount of background between 3 and 13 MeV (the usual region of interest). Beam induced background is frequently the largest and most problematic source of background. This can vary depending on the type of target but common contaminant reactions appear in the table below. The most troublesome of these, ^{11}B(p,γ)^{12}C, emits two coincident high energy γ-rays, leaving a continuous background below ~ 16 MeV.

Reaction	Q-value (keV)	$E_{resonance}$(keV)	Common E_γ(keV)
^{11}B(p,γ)^{12}C	16094	163	4440, 11654 + E_p
^{19}F(p,αγ)^{20}Ne	8115	341	6130, 6920, 7120
^{12}C(p,γ)^{13}N	1944	457	1944 + E_p
^{13}C(p,γ)^{14}N	7551	1523	7551 + E_p

Table 3-2: Common contaminant reactions

The first line of defense against background was simply surrounding the detection setup with ~ 5 cm of lead. At the time of this experiment, this was only possible on four sides but nevertheless greatly reduced the environmental background[20]. A thicker layer of lead actually increased the background arising from the scattering of cosmic rays in the lead [Row02]. Inside the lead shield, but surrounding both the target holder and Ge detector, was a NaI annulus that is 36 cm long with a 42 cm outer diameter and 12 cm inner diameter. The annulus is divided into 16 segments that produce separate signals. We employed the Ge-NaI

[20] Since this work the lead shield has been expanded to six sides.

detection system in two ways. First, the annulus provided an anti-coincidence veto for the Ge detector when the same γ-ray left an energy signal in both the NaI and Ge detectors, e.g. cosmic rays. Similarly, it vetoed sources of background that emitted coincident γ-rays when the reaction of interest produced only a single γ-ray (e.g. minimizing background from $^{11}B(p,\gamma)^{12}C$). Secondly, when the reaction of interest created two γ-rays, a coincident requirement on the two detectors greatly reduced single line background and coincident background above the Q-value of the reaction. Figure 3-15 displays this setup.

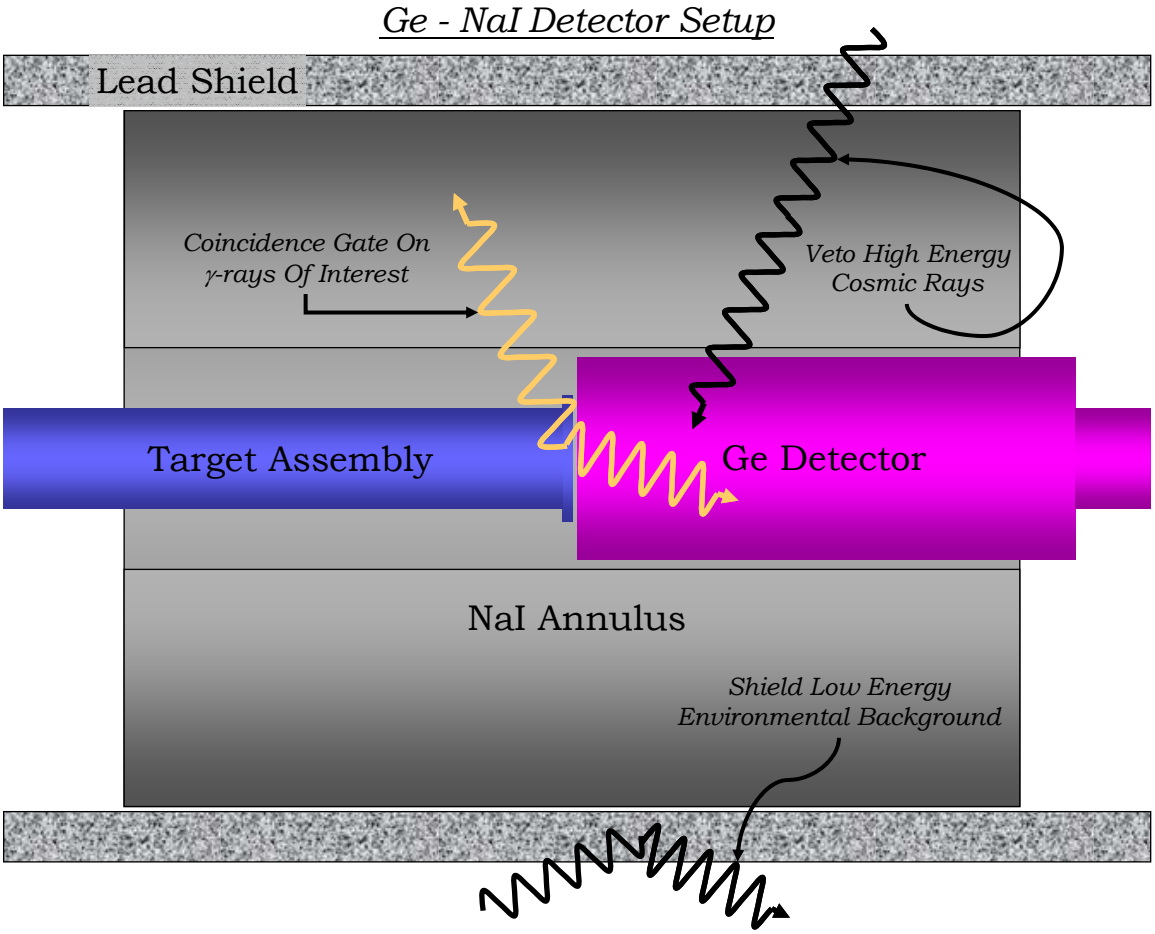

Figure 3-15: Detector setup

This high efficiency, low background setup is the key to making efficient measurements. The Ge and NaI detectors provide energy gates that together sort out γ-rays of interest from those of other sources.

The following graph demonstrates the power of this combined setup to eliminate environmental and cosmic ray background. There was no beam on target during these 16 hour runs. The lead shield reduced the background between 3 and 9 MeV by a factor of 1.7. The NaI anti-coincidence veto, which had a 5 μs gate between the Ge and NaI signals, reduced the background by another factor of 16.

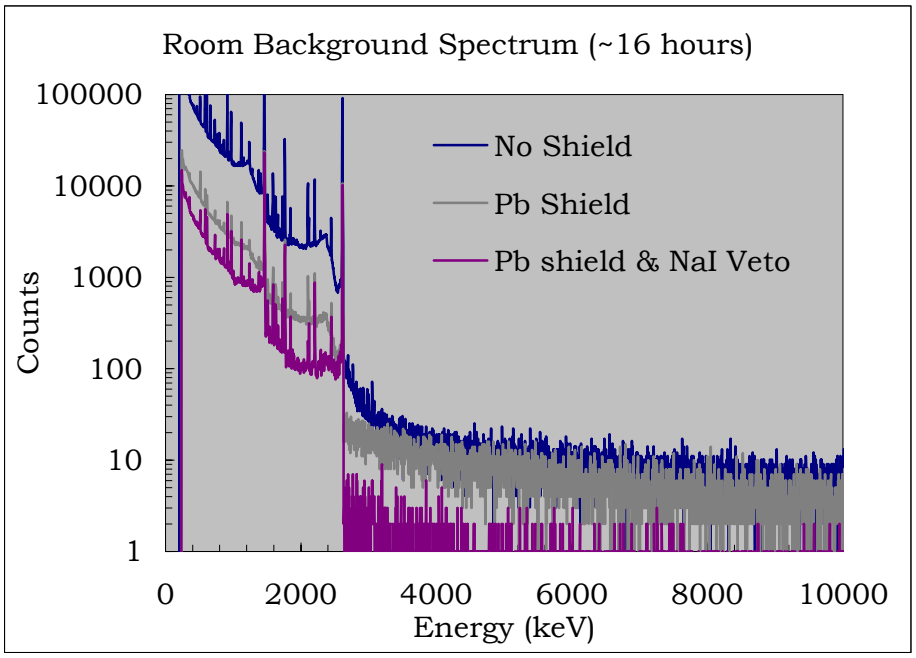

Figure 3-16: Room background spectra

The Pb shield mainly reduces the low energy environmental background while the NaI veto greatly reduces the higher energy background resulting from cosmic rays.

3.6.2. Detector Calibration

Absolute cross section measurements require knowledge of the absolute detection efficiencies. Because of our close detector geometry, it is imperative to know both the absolute photopeak efficiency (for normalizing cross section data) and the absolute total detection efficiency (for summing corrections). The photopeak efficiency is the probability of detecting the *full-energy* of a γ-ray emitted from the target while the total efficiency is the probability of detecting *any* amount of energy from the emitted γ-ray.

We measured the absolute photopeak detection efficiency, $\eta(E)$, using two methods. First, we measured the efficiency of single line sources (^{137}Cs with E_γ=662 keV and ^{54}Mn with E_γ=835 keV) using the factory measured activities to determine their activity at the time of calibration. Second, we made use of the coincident γ-rays produced by ^{60}Co which, in close geometry, often sum together in a third peak at an energy equal to the sum of the coincident γ-ray energies. The power of this technique is that it yields the absolute efficiency independent of the source activity. The decay of ^{60}Co produces γ-rays (with a probability of 99.9% in each case) at 1173.2 (γ_1) and 1332.5 keV (γ_2) and the sum peak occurs at 2505.7 keV (γ_3). Assuming the total efficiency is equal at 1173.2 and 1332.5 keV[21], $\eta(\gamma_1)$ is [Kim03]:

$$\eta(\gamma_1) = \sqrt{\frac{N_{\gamma_1}^{obs} \cdot N_{\gamma_3}^{obs}}{N_t^{obs} \cdot N_{\gamma_2}^{obs} \cdot N_{\gamma_3}^{obs} + N_{\gamma_2}^{obs\,2} \cdot N_{\gamma_1}^{obs}}} \qquad \text{Equation 3-3}$$

where N_t^{obs} is the total number of counts in the entire spectrum and N^{obs} is the number of counts in each photopeak. (For γ_2, simply reverse the indices for 1 and 2.)

These four points provide an absolute efficiency calibration between 662 and 1332 keV. However, in this case it is necessary to know the efficiency up to ~ 8000 keV. We calculated the photopeak efficiency using the simulation program MCNP and normalized the result to the four absolute efficiency points. As an independent check on our ability to calculate the efficiency curve, we measured the relative efficiency using radioactive sources (^{56}Co and ^{152}Eu) and branches of well understood resonances (^{14}N(p,γ)^{15}O, ^{23}Na(p,γ)^{24}Mg, ^{26}Mg(p,γ)^{27}Al, and ^{27}Al(p,γ)^{28}Si). The strength of these sources and reactions create difficult dead time and summing problems. To alleviate these problems, we used varying detector geometries. Whenever possible, the detector was in the 10 mm geometry and the γ-ray yield was corrected for summing. The shape of the simulation and relative efficiency agreed well (figure 3-17). The weighted deviation between the normalized MCNP curve and the experimental data was approximately 5%. The absolute photopeak efficiency was:

[21] This approximation is accurate to 3%.

$$\eta_{photopeak}(E) = 10^{-0.5375+0.155\cdot\log\left[\frac{E}{keV}\right]-0.136\cdot\log\left[\frac{E}{keV}\right]^2} \qquad \text{Equation 3-4}$$

To add perspective, the efficiency from gamma-sphere is only double our value at 1 MeV.

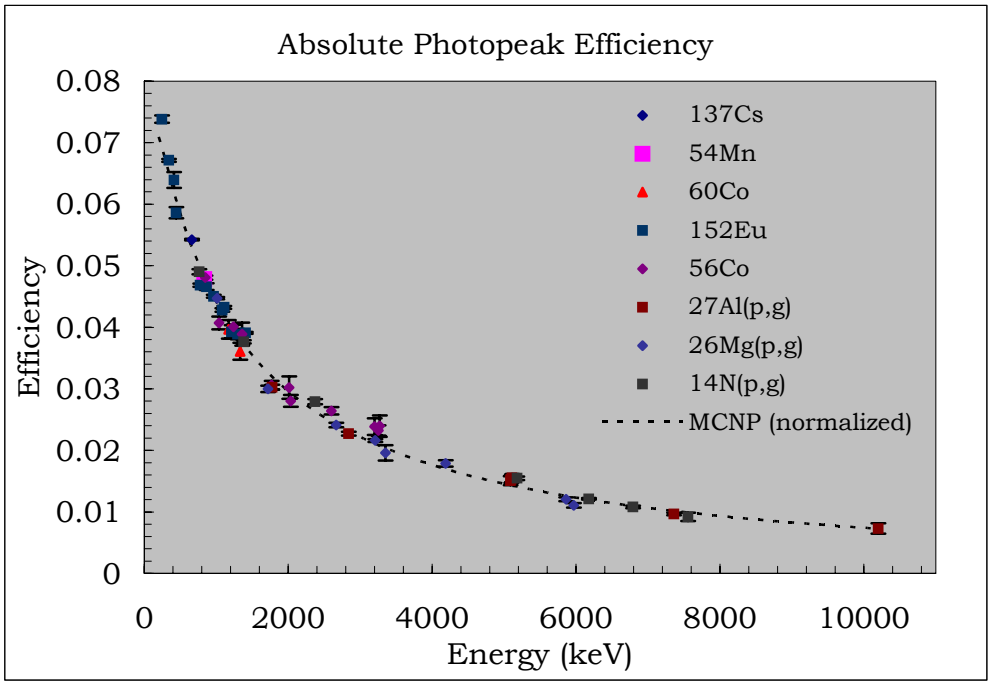

Figure 3-17: Ge detector photopeak calibration

When analyzing γ-ray yield data, it is necessary to correct for summing and this requires knowledge of the *total* absolute detection efficiency. We determined this in a similar manner to that for the photopeak efficiency, by measuring it directly with ^{54}Mn, ^{137}Cs and ^{60}Co sources. For the single line sources, we determined the total number of counts in the entire spectrum, correcting for background subtraction and the low energy noise threshold. For ^{60}Co, the absolute efficiency is again independent of source activity and only dependent on the number of γ-rays in the each photopeak, the sum peak, and the total number of counts in the spectrum (N_t^{obs}). This technique assumes that the total efficiencies for the two γ-rays are equal which is in error by a maximum of 3% [Kim03]. Therefore, the total efficiency at the average of their energy, 1253 keV, is:

$$\eta^{total}(1253\,keV) = \sqrt{\frac{N_{\gamma_1}^{obs} \cdot N_{\gamma_2}^{obs}}{N_t^{obs} \cdot N_{\gamma_3}^{obs} + N_{\gamma_1}^{obs} \cdot N_{\gamma_2}^{obs}}}$$ Equation 3-5

Unfortunately, the total efficiency can not in practice be measured at high energies. We rely on simulating the total efficiency using MCNP. This simulation agrees with the three experimental points to within 5%. The energy dependence of the total efficiency is well-understood and the three data points simply provide a normalization [Deb88][Lon03]. Therefore, the lack of high energy data points does not imply a large uncertainty in the total efficiency at high energies. The absolute total efficiency was:

$$\eta_{photopeak}(E) = \left[525.4 - 0.2058 \cdot \frac{E}{keV} + \left(5.807 \cdot 10^{-4}\right) \cdot \left[\frac{E}{keV}\right]^2\right] \cdot \left(3.551 \cdot 10^{-4}\right) \cdot e^{-1.779 \cdot \left[\frac{E}{keV}\right]} + 0.1543$$ Equation 3-6

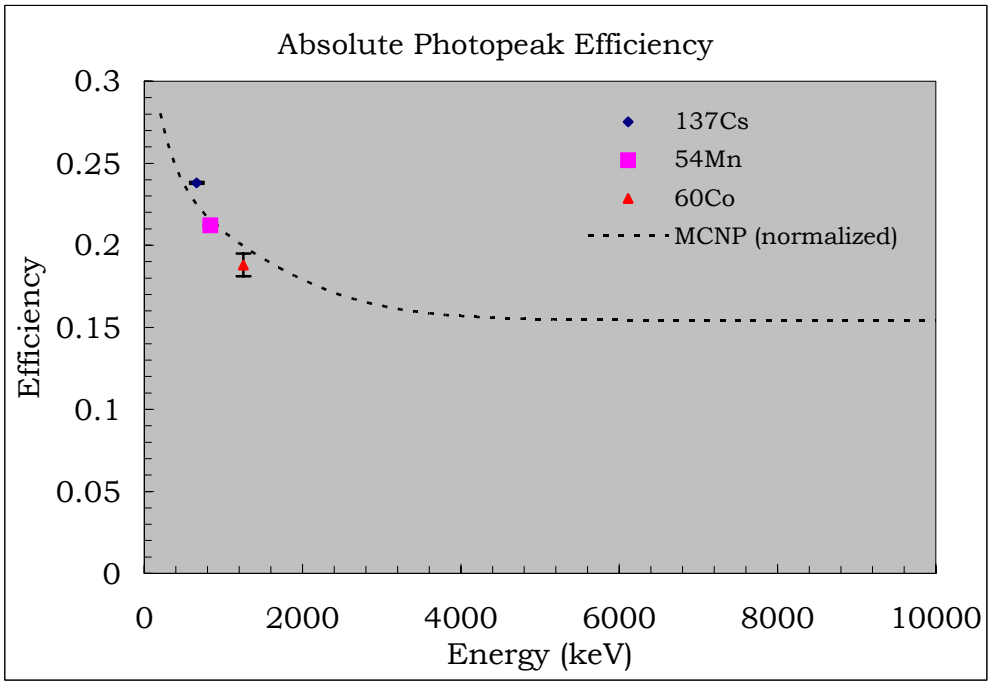

Figure 3-18: Ge detector total efficiency calibration

3.6.3. Detector Setup and Electronics

The Ge and NaI signals were fed directly into standard NIM electronics. All signals were processed with NIM modules and fed into a VME ADC. The 16 segments from the annulus were gain matched and summed together with a fan-in-fan-out module. This effectively resulted in one signal each from the NaI annulus and Ge detector. We split each detector signal into two separate branches for energy and timing. The timing branch was delayed to adjust for the shaping time of the energy signal. The timing branch had three components fed through a timing filter amplifier: the ADC gate, coincidence TAC and anti-coincidence TAC. Each event in the Ge detector triggered the ADC with a threshold at approximately 300 keV. We measured the ADC dead time through coincidences between the ADC BUSY output and clock set at one second intervals. Because of the low count rates involved, the dead time was usually ~ 0.5%. Figure 3-19 shows a schematic of this setup.

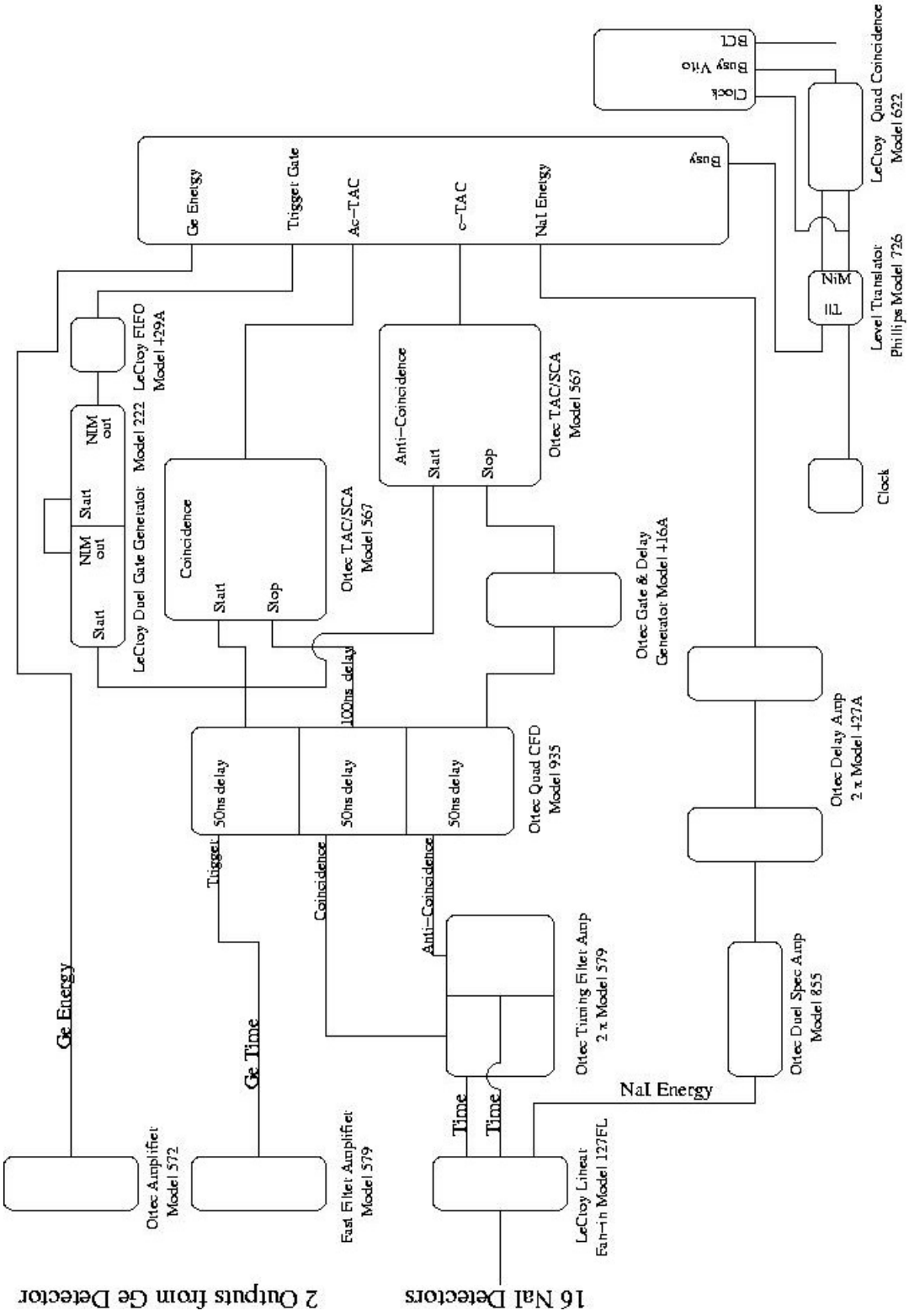

Figure 3-19: Ge-NaI electronics setup

Chapter 4:

Measuring the $^{14}N(p,\gamma)^{15}O$ S-factor

4.1 The Experiment

The measurements presented in this chapter are the culmination of one year in which we ran experiments almost continually from March 2002 to March 2003 (with a six week break for my honeymoon!). This includes well over 1000 hours of running and considerable time, spent in a control room with no windows, and effort from the many participants. The main contributors to the actual data collection were C. Fox, J. Pollannen and I. Important assistance came from A. Champagne, R. Fitzgerald, C. Iliadis, and C. Rowland. In total, there exist approximately 4 GB of data in 1000 files. We burned 25 targets clean. In addition, target construction required J. Pollanen and R. Runkle to sit for many hours in the basement of the dungeon-like Philips Hall. I believe the quality of the data demonstrate the effort invested.

4.2 The Cross section and Experimental Yield

4.2.1. Non-resonant Yield

The observed yield of a reaction is directly proportional to the probability of the reaction occurring, which for convenience is represented by the cross section (σ). Since the cross section is the effective size of one target nucleus, the number of reactions per incident particle (Y) is the product of the cross section and the number of target nuclei per area (n_t).

$$Y = \sigma \cdot n_t = \frac{S}{E} \cdot e^{-\frac{1}{\hbar}\cdot\frac{Z_x \cdot Z_y}{2\cdot\varepsilon_o}\cdot\sqrt{\frac{\mu}{2\cdot E}}} \cdot n_t \qquad \text{Equation 4-1}$$

where S is the S-factor introduced in section 2.2 (along with the other parameters). The target nuclei are distributed over a finite target thickness (Δ) and the cross section is energy dependent over this interval. For small Δ and in a region absent of resonances, the S-factor is smoothly varying and approximately constant over the target thickness. To correct for the

energy dependence of the cross section over the target thickness, the energies in equation 4-1 can be evaluated at an effective energy (E_{eff}). (See section 4.6.2.)

The experimental yield is the number of outgoing γ-rays per incident proton.

$$Y_{\exp} = \frac{N_{\gamma}^{observed}}{N_{p}^{incident} \cdot \eta_{\gamma} \cdot W_{\gamma}} \qquad \text{Equation 4-2}$$

where $N_{\gamma}^{observed}$ is the photopeak intensity, $N_{p}^{incident}$ is the total number of incident protons, η_{γ} is the absolute γ-ray photopeak detection efficiency and W_{γ} is the angular distribution coefficient of the particular γ-ray in question. By equating the above yields and rearranging, the S-factor is:

$$S(E_{eff}) = \left[\frac{N_{\gamma}^{observed}}{N_{p}^{incident} \cdot \eta_{\gamma} \cdot W_{\gamma}} \right] \cdot E_{eff} \cdot e^{-\frac{1}{\hbar}\cdot\frac{Z_x \cdot Z_y}{2\cdot\varepsilon_o}\cdot\sqrt{\frac{\mu}{2\cdot E}}} \cdot n_t \qquad \text{Equation 4-3}$$

Each individual transition has at least one unique γ-ray and thus different $N_{\gamma}^{observed}$, η_{γ}, W_{γ} and S(E) values.

In principle, this is a simple relationship. It requires counting N_{γ} and N_p and determining n_t and η_{γ}. Determining η_{γ} and N_p is relatively straightforward. The largest sources of error normally result from low statistics (e.g. $N_{\gamma}^{observed} < 50$) and systematic errors arising from target stoichiometry and stopping power estimates.

4.2.2. Resonant Yield

Resonances at energies below the Coulomb barrier are characteristically narrow with widths of a few keV or less. These narrow resonances are difficult, if not impossible, to measure in a stepwise fashion. In practice, when measuring a narrow resonance, the beam resolution and target thickness are often much larger than the total resonance width. This necessitates measuring the total resonant contribution which results from integrating the equation 2-14 over all energies:

$$\int_0^{\infty} \sigma_{res}(E)\,dE = 2 \cdot \pi^2 \cdot \lambda\!\!\!^{-}_{res}{}^2 \cdot \omega\gamma, \text{where } \lambda\!\!\!^{-}_{res}{}^2 = \frac{\lambda_{res}{}^2}{4 \cdot \pi^2} \qquad \text{Equation 4-4}$$

where ω is the statistical spin factor mentioned previously and γ is $\frac{\Gamma_p \cdot \Gamma_\gamma}{\Gamma}$. Since the proton widths under consideration here are typically much larger than the γ-ray width ($\Gamma_p \geq 10^3\ \Gamma_\gamma$), then $\Gamma_p \sim \Gamma$ and $\Gamma_\gamma \sim \gamma$. Therefore, measuring the resonance strength provides an accurate determination of Γ_γ; measuring the total width gives Γ_p.

It is customary to refer to the combined quantity ωγ as the resonance strength. This is the crucial experimental quantity. The total resonance strength may be distributed among various branches. This is due to the fact that the compound state formed by a resonance can decay through several lower energy states each with a unique primary γ-ray. The branching ratio, for a particular state i, is the probability that the resonance proceeds through state i:

$$B_i = \frac{\Gamma_\gamma^i}{\Gamma_\gamma^{total}} = \frac{Y_{res}^i}{Y_{res}^{total}} \qquad \text{Equation 4-5}$$

where Y_{res}^i is the resonant yield for state i and Y_{res}^{total} is the sum of yields from all branches. The total yield from all the branches is directly proportional to the resonance strength:

$$Y_{res}^{total} = \frac{\lambda^2}{2} \cdot \frac{\omega\gamma}{\varepsilon} \qquad \text{Equation 4-6}$$

where the quantity ε is the effective stopping power of the target in the center of mass system. This relationship is valid when the target thickness is much larger than the resonance width. In practice, it is necessary to correct for the small fraction of the resonance existing outside the target. In this case,

$$Y_{res}^{total} = \frac{\lambda^2}{2 \cdot \pi} \cdot \frac{\omega\gamma}{\varepsilon} \cdot \left[\arctan\left(\frac{E - E_r}{\Gamma/2} \right) - \arctan\left(\frac{E - E_r - \Delta}{\Gamma/2} \right) \right] \qquad \text{Equation 4-7}$$

where Δ is the thickness of the target (see section 4.6.4). Equation 4-5 must also be corrected

for effects such as beam straggle and beam resolution as described by [Rol88]. When the resonance occurs well within the target (Δ>>Γ), these factors are negligible. The experimental yield is measured identically as in equation 4-2. Substituting this and rearranging the previous equation relates the resonance strength to the yield:

$$\omega\gamma = \frac{2\cdot\pi\cdot\varepsilon}{\lambda^2\cdot\mu}\frac{1}{\left[\arctan\left(\frac{E-E_r}{\Gamma/2}\right)-\arctan\left(\frac{E-E_r-\Delta}{\Gamma/2}\right)\right]}\sum_i\frac{N_{yi}}{N_p\cdot\eta_i\cdot W_i} \qquad \text{Equation 4-8}$$

where i is the sum over each transition.

4.3 Targets

The targets in this experiment consisted of a Nitrogen/Tantalum compound which we produced by implanting N_2^+ ions into a Ta backing (~0.5 mm thick). The implantation produces a surface layer on the backing whose depth is a function of the implantation energy. Keinonen and Anttila extensively studied nitrogen implantation including target stoichiometry and the thickness as a function of implantation energy [Kei78]. Their Ta:N ratio was 0.64(8) which our targets reproduced.

We fabricated all targets at the Physics and Astronomy Ion Implanter at the University of North Carolina at Chapel Hill. The implanter produced N_2^+ beams with energies of 20 keV, 40 keV and 110 keV which created 5, 10, and 18 keV thick targets at the 259 keV resonance. These thicknesses are consistent with measurements by Seuthe et al. [Seu87]. The varying thicknesses balance statistical uncertainties resulting from low count rates and systematic error from averaging the S-factor over the target thickness (see section 4.4.3). The implantation target setup was nearly identical to that described in section 3.4. The beam spot exiting the acceleration tube was the size of a pencil eraser and was scanned over an area approximately 8 cm x 8 cm to ensure a uniform implantation layer. To confirm this, the target chamber was equipped with a window that allowed observation of the beam spot. The total charge accumulation exceeded that prescribed by Seuthe et al. by approximately a factor of two in order to ensure saturation and thus consistent stoichiometry. For each target, yield curves of the 259 keV resonance indicated the target thickness and confirmed saturation. Each yield curve was fit and integrated using the program YCFIT [Row01]. An example yield curve and

fit are shown in figure 4-1. The resonance energy corresponds to the point at ½ the maximum yield on the front face of the target; note that this value is shifted from 259 keV. This results from a dead layer on the target's surface. Due to the implantation beam energy, the implantation layer didn't extend to the target surface. This means that the proton beam lost some energy before entering the active portion of the target. The characteristic dead layers were 0.5, 1.5 and 2 keV for the 5, 10 and 18 keV thick targets.

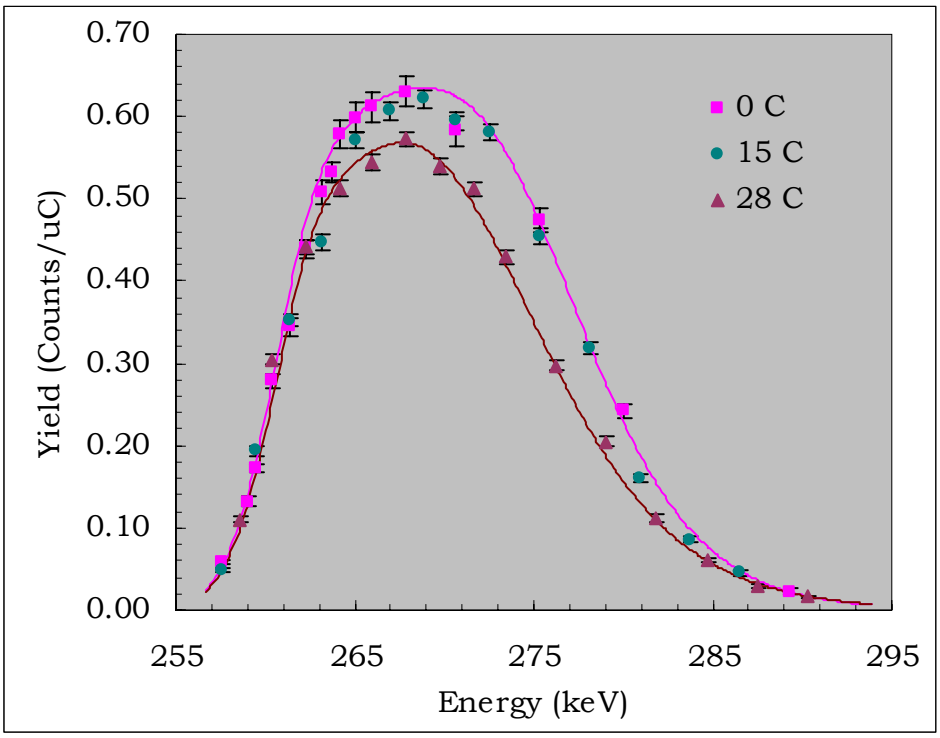

Figure 4-1: Example yield curve showing varying accumulated charges

During the experiment, the targets experienced varying beam currents and energies. Overall, the targets remained stable over accumulated doses of up to 20 – 25 Coulombs, depending on their thickness. Over this period, minimal carbon buildup occurred (the Cu tube was essential in this regard). The target lifetime strongly depends on the beam power density, and, whenever possible, it was minimized by maintaining a large, circular beam spot (diameter ~ 1.3 cm). We monitored the size using a MgO covered beam stop located in front of the target. The third picture in figure 4-2 shows how, in times of weakness, the beam was focused into a line and quickly burned through targets.

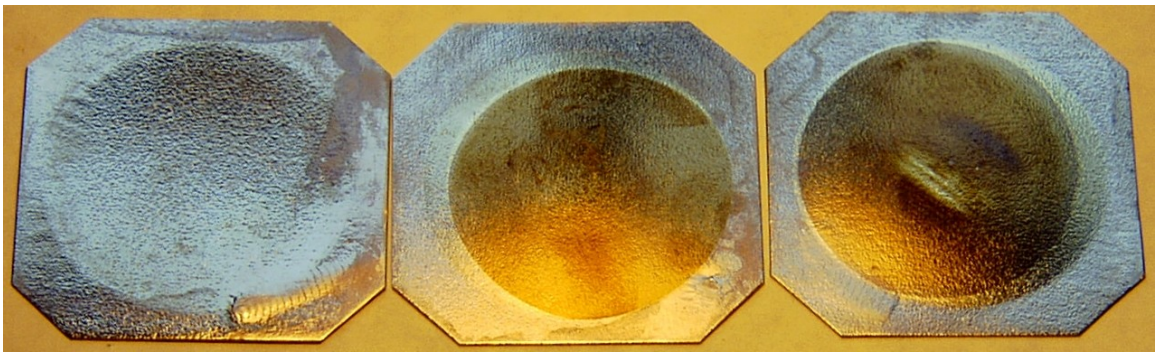

Figure 4-2: Blank and N_2^+ Implanted (New and Used) Targets

These targets were used in this experiment. The left hand picture shows a tantalum backing prior to implantation. In the center, the circular region was implanted with ^{14}N. The right hand target was bombarded with a horizontally tuned beam. This quickly degrades targets.

4.4 Measuring the E_p = 259 keV Resonance Strength

Understanding the 259 keV resonance was crucial to the success of this experiment. It was not only an important contribution to the cross section but served numerous other functions. We measured the number of target atoms (n_t), the target thickness (Δ) and target degradation using this resonance. Both n_t and Δ were crucial normalization quantities for the absolute cross section and it was therefore important to have an accurate understanding of the resonance parameters: the total resonance strength ($\omega\gamma$) and the total width (Γ).

We re-measured this resonance strength for two reasons: to ensure the accuracy of the previous results and, more importantly, to check the systematics of our experimental setup including the target stoichiometry. The maximum resonant yield occurs when $\Delta >> \Gamma$ and the high and low energy tails are centered in the target. We measured the resonant yield with an 18 keV thick target at a beam energy of 270 keV. With this energy and thickness, the target covered 97% of the resonance. We measured the resonant yield of each branch, which required correcting the raw data for coincident summing effects. (I discuss this point in detail in section 4.6.4) The only non-experimental input was the target stopping power (ε_{tot}). The program SRIM2000 was used to calculate the individual stopping powers of protons in nitrogen and tantalum [Zie00]. Assuming the well-established Ta/N from Keinonen and Anttila, the total stopping power was calculated from the weighted sum of the individual

stopping powers:

$$\varepsilon_{tot} = \varepsilon_{Nitrogen} + \frac{N_{Ta}}{N_{Nitrogen}} \varepsilon_{Ta} \qquad \text{Equation 4-9}$$

where N is the number density of atoms. The total stopping power used here was 3.48 x 10^{-14} eV · cm^2. Keinonen and Anttila measured the range coefficients for protons in ^{15}N and their results agree well with Monte Carlo calculations. Furthermore, their measurement of ε for protons in a similar nucleus, ^{13}C, agrees exactly with calculations, albeit a 30% error bar.

Figure 4-3 shows the resonant γ-ray yield from one particular spectrum. We calculated the resonance strength by averaging the primary and secondary γ-ray yield. Our value of 12.7(2.1) meV for the resonance strength differs by less than 9 percent from the value of 14(1) meV quoted by Becker et al.. They used inverse kinematics, i.e. a ^{14}N beam incident on a hydrogen gas target, and because of this their results is considered the standard value. For strong resonances like this one, statistical errors are negligible and systematic errors dominate. Reactions performed in inverse kinematics eliminate systematic errors associated with the target because the yield is measured relative to well understood elastic scattering. The fact that our value agrees well with Becker et al. implies that our combined errors in target stoichiometry and detection (both photopeak and total) efficiency were minimal. The large error of 17% results primarily from uncertainties in these quantities. Most notable of these were the uncertainties in the stopping powers (15%). Uncertainties in the photopeak efficiency and total efficiency contributed 5% each to the total uncertainty.

Another important result is a new measurement of the branching ratios (equation 4-5). The previous branching ratios quoted in [AjS91] have small errors (~0.005) but it quickly became clear that the ground state branch was far too big. We measured the branching ratios with the detector located 23 cm from the target, which eliminated the need for summing corrections. For this measurement, the only uncertainties result from the *relative* photopeak efficiency and statistics. Our results are consistent with the previous values for all transitions except the ground state. This new result is especially important for calculating the ground state S-factor far from the 259 keV resonance.

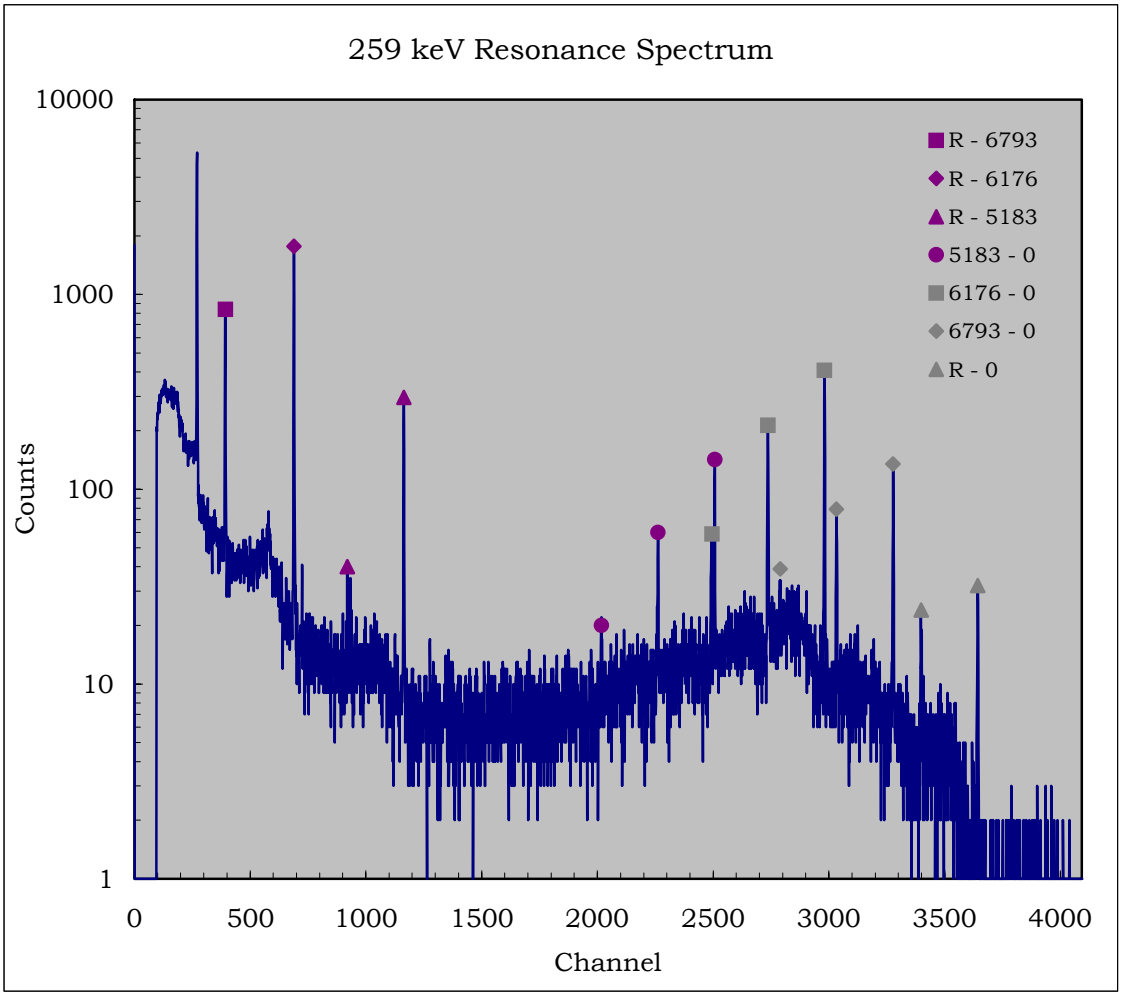

Figure 4-3: Example on-resonance spectrum

E_r = 259 keV Branching Ratios		
Transition	Previous	Present
ground state	3.5 ± 0.5	1.7 ± 0.2
5183 keV	15.8 ± 0.6	17.7 ± 0.9
6176 keV	57.5 ± 0.4	58.7 ± 3.4
6793 keV	23.2 ± 0.6	21.9 ± 1.2

Table 4-1: Branching ratios for the 259-keV resonance

4.5 Search for a resonance at E_p = 119 keV

The Nelson et al. experiment utilized a 10 to 40 μA proton beam incident on a deuterated ammonia ice target. The proton beam stopped in the target and γ-rays were observed at beam energies between 110 and 150 keV. Because they used a stopping target, only the front half of the resonant yield curve could be observed. Mapping the entire yield curve is crucial in confirming the existence a new resonance because it demonstrates that the resonance only exists in a small energy region, which can be checked against the target thickness. In addition, they determined the incident proton flux relative to proton capture on deuterium (hence the deuterated ammonia target) which is known to create a significant neutron flux [Jen50]. Coincidently, the observed 7414 keV γ-ray peak resided on top of a neutron capture background peak and corresponds exactly to a neutron capture line in ^{14}N. Because of the difficulty in extracting the yield from the background and concerns of consistent target normalization under beam bombardment, it was important to confirm the existence of this resonance with a technique that was not hindered by these systematic errors.

The LENA setup differed from that of Nelson et al. in three important ways: the targets did not contain deuterium, they were of finite thickness, and they were continually checked for degradation using the 259 keV resonance. The 259 keV yield curve for the target used in this search was shown in section 4.1. The thickness was approximately 18 keV at this energy and there was no noticeable degradation over the duration of this experiment (~5 Coulombs). In order to place the resonance in the center of the target, it is necessary to determine the target thickness *at the beam energy*. This was calculated from the stopping powers:

$$\Delta(\mathrm{E}) = \frac{\varepsilon_{\mathrm{E}}}{\varepsilon_{259}}\Delta(259) \qquad \text{Equation 4-10}$$

where E is the beam energy. From the measured thickness, we calculated a target thickness of 22 keV at 119 keV using stopping powers from SRIM2000. With the proposed resonance strength and these target properties, the expected yield had a maximum value of 130 counts/Coulomb between 120 and 160 keV. Figure 4-4 shows the expected yield curve. (Note that the yield curve was shifted to account for dead layer effects at the target surface.)

We determined the resonance strength relative to the value for the 259 keV resonance through the relation:

$$\omega\gamma_{119} = \omega\gamma_{259} \cdot \frac{119 \cdot \varepsilon_{119} \cdot Y_{119}}{259 \cdot \varepsilon_{259} \cdot Y_{259}} \qquad \text{Equation 4-11}$$

which follows from equation 4-6. This method further reduces systematic errors by the use of relative stopping powers. We searched for this resonance by measuring the yield at proton energies of 126, 135, 149 and 168 keV. The 126 and 135 keV points correspond to expected on-resonance points. Two separate points were taken to compensate for a possible error in the resonance energy. (With both of these points, any resonance between 105 and 135 keV would be detected.) The two additional off-resonance points at 149 and 168 keV allowed a comparison of background counts between the resonant and non-resonant yield. A blank target run, i.e. only a Ta backing, demonstrated the amount and shape of any non-nitrogen induced background. Figure 4-4 shows the observed yield for the on-resonance points. In all cases we observed no counts at the predicted peak location of 7414 keV.

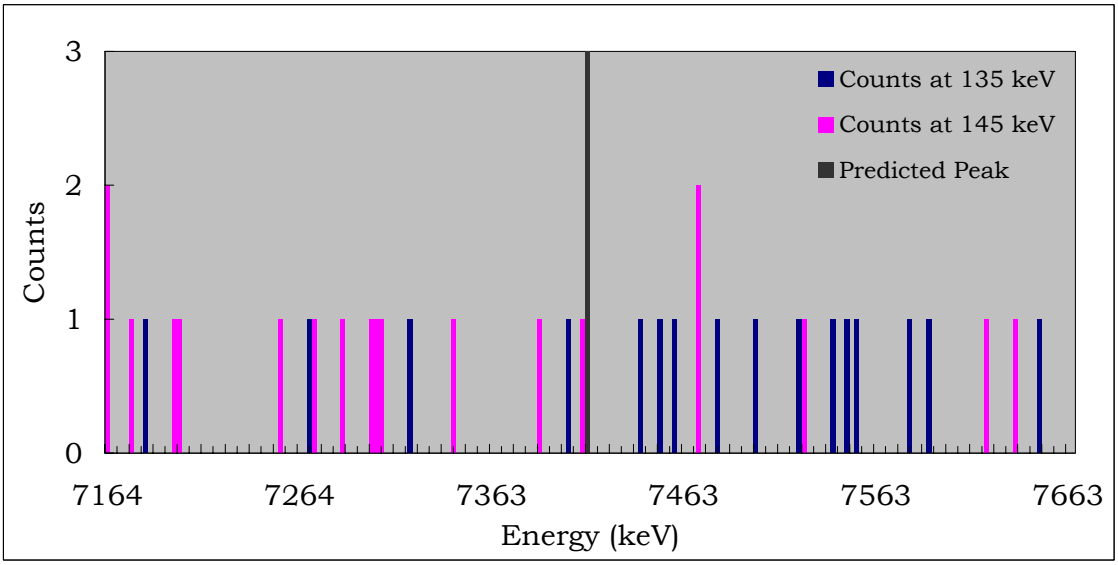

Figure 4-4: Yield of the predicted resonance at E_p = 119 keV

Since the predicted γ-ray yield was not observed, we determined an upper limit on the yield based on the observed background and total charge accumulation. We accomplished this using a maximum-likelihood estimation with Poisson statistics described by Hannam and

Thompson [Han99]. The background template was uniform with no structure, as observed in the blank target run. The signal template was a Gaussian peak whose width was a width a function of the detector resolution (4.0 keV FWHM), detector energy calibration uncertainty (1 keV), resonance energy uncertainty (2 keV), and an estimated maximum Doppler broadening (4 keV FWHM). The MLE for all spectra was zero and, as a result, only an upper limit for the yield could be established. Figure 4-5 shows the 90% confidence limit on the yield for each energy.

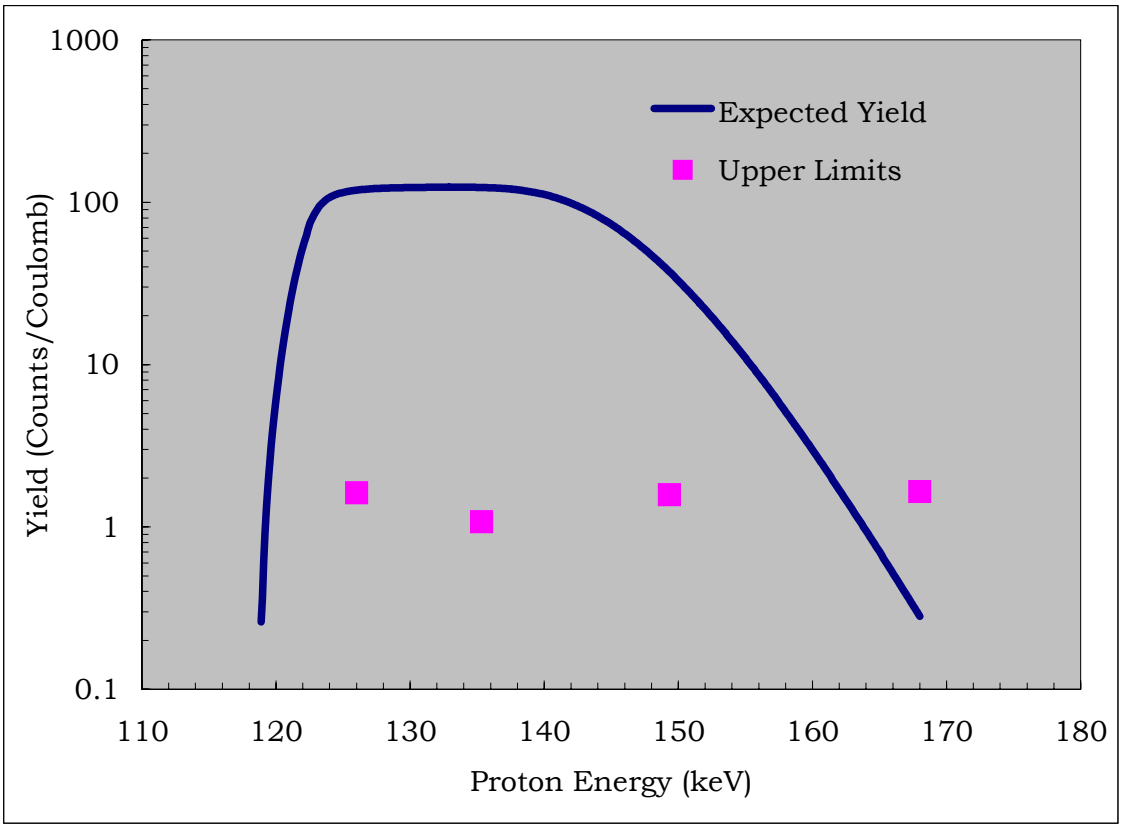

Figure 4-5: Predicted and measured yields from the 119 keV resonance.

The two on-resonance points constrained the maximum resonant yield to 0.96 counts/C at a 95% confidence level. It is important to note that each upper limit was not sensitive to the background template used since there was negligible background. (If the background model were completely neglected, the combined yield from Poisson statistics would be 1.02 counts/C.) The upper limit confines the resonance strength to a maximum of 32 neV. No systematic uncertainties were included in this calculation. They were estimated to be: 7% in

the 259 keV resonance strength, 5% for the relative stopping powers, and negligible uncertainties in the *relative* charge collection (117 keV versus 259 keV) and detection efficiency (6793 keV versus 7414 keV). These uncertainties were not combined with the Poisson distributed upper limits since they are Gaussian distributed; if they were, the combined upper limit would rise only 2%.

The upper limit of 32 neV applies not only to a resonance at 117 keV but, because of the target thickness, these data rule out any resonance in the ground state transition between 113 and 145 keV up to a resonance strength of 0.11 μeV. The value of 32 neV is over two orders of magnitude lower than the proposed resonance strength. We conclude that the Nelson et al. experiment was flawed.

4.6 Non-resonant S-factor Measurements

4.6.1. Overview

Measuring the non-resonant S-factor consumed the majority of time and energy during the experimental phase of this project. Our measurements extend from 133 to 485 keV and almost overlap the previous low energy measurement of Lamb and Hester. The crucial difference between these two experiments is that we observed each transition individually. The transitions of primary astrophysical interest are capture into the ground state, 6176, and 6793 transitions. The ground state transition emits only one γ-ray with an energy equal to the sum of the reaction Q-value and the beam energy, i.e. 7297 keV + E_{beam}. This transition is the worst case scenario because it is a small branch, has multiplicity one (no coincident requirement is possible), the detection efficiency above 7000 keV is poor, the photopeak is smeared out over the target thickness, and γ-rays from the other transitions will sum into the ground state photopeak. Furthermore, it could be significantly Doppler shifted; however this was not observed. Because of these factors, the ground state was the most difficult to detect and we measured it down to an effective energy of 187 keV. The 6176 keV transition mainly results from the 259 keV resonance and precipitously drops below this energy. Furthermore, the Compton scattered γ-rays from the larger 6793 keV transition make the identification of the 6176 keV peak difficult. We measured this transition down to 153 keV. Below this energy, we abandoned both the ground state and 6176 keV transitions and focused only on the 6793 keV transition, which comprises 90% of the S-factor. The non-resonant analysis differed

from the resonant case in three principle ways: an effective energy had to be determined, detector gating was necessary for background reduction, and significant summing corrections were required. I address each of these in the following sections.

4.6.2. The γ-ray Yield

Measuring the non-resonant yield implies small count rates, particularly compared to resonance capture in contaminant reactions. Futhermore, the large environmental background was not fully reduced because the NaI annulus could not be completely surrounded with lead. This made measuring the primary γ-rays difficult, even when requiring a Ge-NaI coincidence. Despite the lower detection efficiency, measuring the higher energy γ-rays from secondary transitions resulted in more accurate peak identification and lower statistical errors. In all cases except the ground state, the secondary γ-rays were used in the final S-factor calculations. Figure 4-6 shows the decay scheme for the four most populated transitions.

The 259 keV resonance effectively divides the excitation function measurements into high and low energy regions. Above 259 keV, we observed background from $^{13}C(p,\gamma)^{14}N$ and $^{19}F(p,\alpha\gamma)^{20}Ne$ that polluted the γ-ray spectra. The broad $^{19}F(p,\alpha\gamma)^{20}Ne$ resonance produces a 6130 keV γ-ray whose Compton scattered γ-rays swallowed the 5183 and 5241 keV photopeaks. This is shown in the figure 4-7. At higher energies, the $^{13}C(p,\gamma)^{14}N$ reaction ($E_\gamma >$ 7500) made the ground state transition difficult to detect. For energies below 259 keV, the high energy background was almost exclusively from $^{11}B(p,\gamma)^{12}C$ whose yield far surpassed the environmental and cosmic ray background. In all cases, we extracted the peak intensities assuming a linear background. The only instance where this was problematic occurred in the 6176 keV transition near the 341 keV resonance of $^{19}F(p,\alpha\gamma)^{20}Ne$. This resonance produces a large peak at 6130 keV which made fitting the 6176 keV peak difficult.

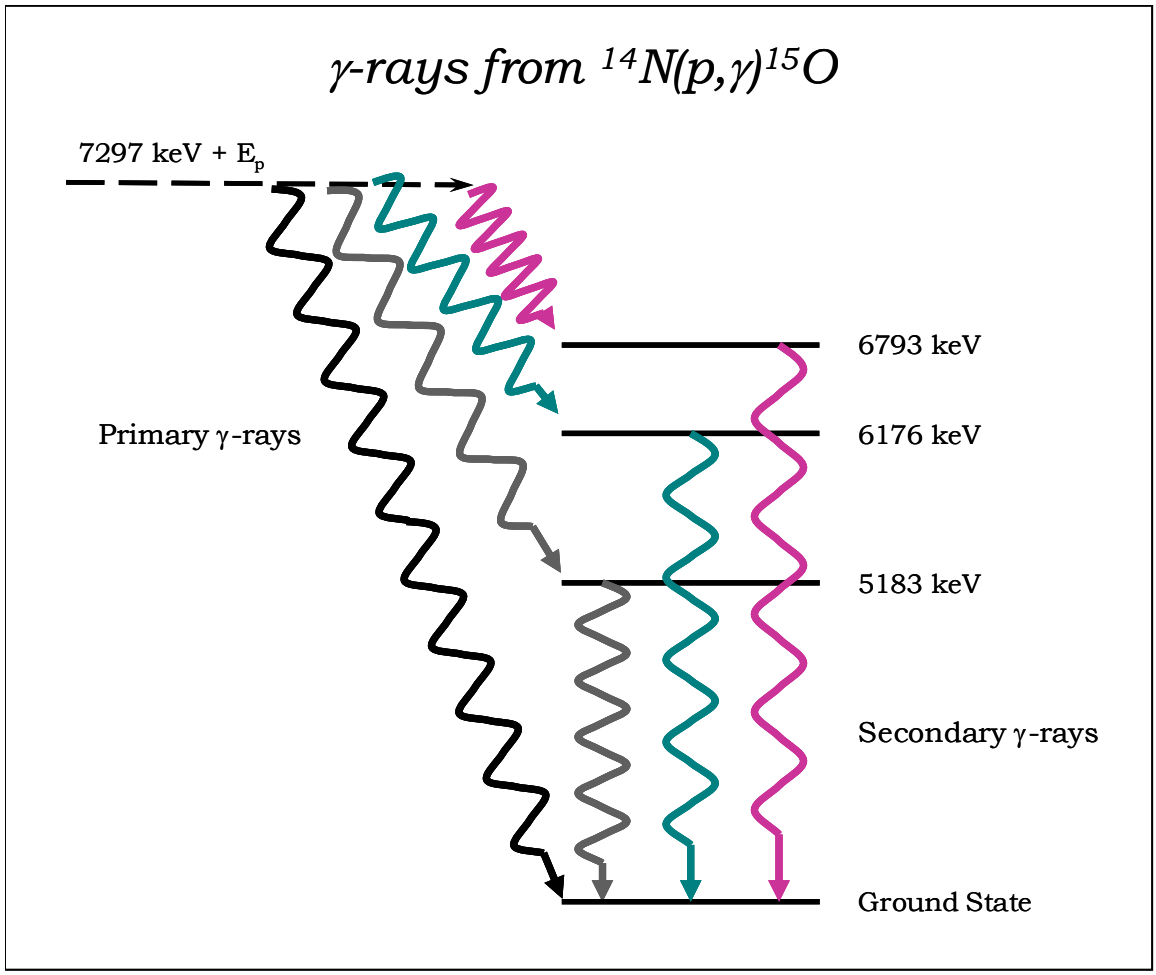

Figure 4-6: γ-rays emitted from the $^{14}N(p,\gamma)^{15}O$ reaction

The observed γ-ray yields used in the analysis were the primary γ-ray connecting to the ground state and the secondary γ-rays from the excited states, i.e. 6793, 6176 and 5241 keV. Not shown here are three small branches that proceed through an excited state at 5241 keV. For the two γ-ray cascades, both γ-rays are emitted within the resolving time of the electronics. Because of this and our close geometry, the observed γ-ray yields were corrected for summing effects. For the ground state, false counts were added to the photopeak when both γ-rays from any of the other transitions deposited all of their energy in the Ge detector. For the other transitions, counts were lost from the photopeak when the coincident primary γ-ray yield deposited any of its energy in the Ge detector.

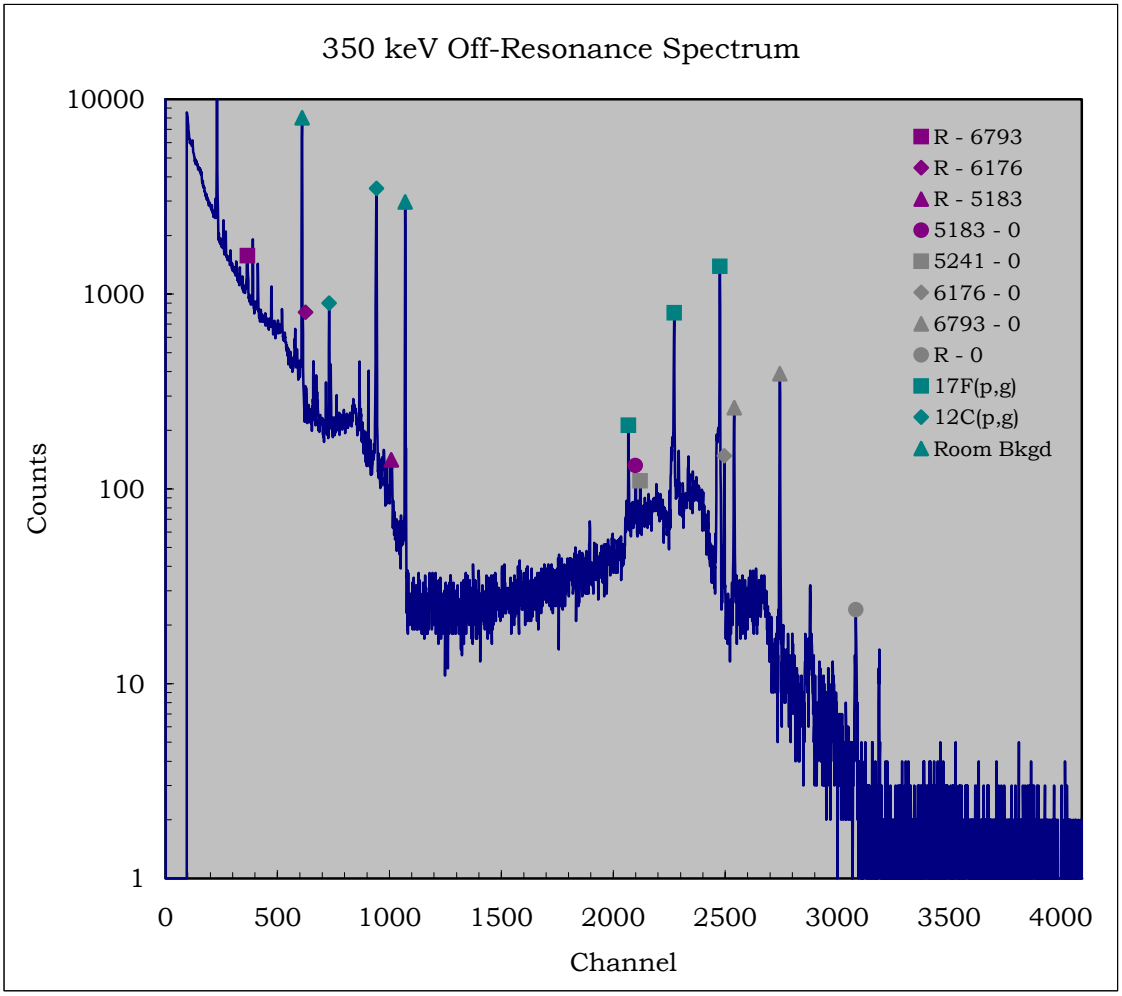

Figure 4-7: Off-resonance spectrum

4.6.3. Determining n_t

The S-factor is directly proportional to the number of active target nuclei per area (equation 4-3). For experiments measuring absolute as opposed to relative yields, the uncertainty in this quantity is often greater than statistical and other systematic uncertainties. The tantalum-nitride targets used in this experimental are comparatively well understood. The value of n_t can be calculated directly from the stoichiometry, which is known to 13%, but in addition to this uncertainty one must add uncertainties in calculating absolute stopping powers (15%). Combined, these give a 20% uncertainty.

When a particular nucleus has a precisely measured resonance, these uncertainties can be reduced significantly by directly measuring n_t from the resonance yield. This is especially true

for resonance strength measurements using inverse kinematics, because this technique eliminates stopping powers entirely. In general, the resonance strength and n_t are related by [Gov59]:

$$n_t = \frac{2}{\lambda^2}\frac{A}{\omega\gamma} \qquad \text{Equation 4-12}$$

where A is the area under the resonant yield curve. The present uncertainty on the 259 keV resonance strength is 7% and the uncertainty in A results mainly from the detection efficiency whose uncertainty was 5%. With these values, the total uncertainty in n_t is thus reduced to from 20% to approximately 9%.

4.6.4. Effective Energy Determination

In practice, we did not measure the yield at the beam energy but over the energy distribution of protons in the target. Protons traveling through the target slow down due to electromagnetic interactions with atoms. The vast majority of protons that do not react exit the target with energies below the incident beam energy. The average difference between the entrance and exit energies is the target thickness, which we extract from resonant yield curves. Because the beam can interact with ^{14}N nuclei at any of these energies, the non-resonant yield must be averaged over proton energies that exist in the target. This creates a problem in determining the cross section, which varies over the target thickness. When measuring the yield far from a resonance, the cross section continues to vary considerably over the target thickness, but the S-factor normally varies slowly over small energy ranges (<20 keV).

To minimize this effect, one would ideally use the thinnest targets possible, but there is a trade off between target thickness and count rate. Low count rates result in larger statistical uncertainties. Thick targets increase the count rate, but also increase the systematic error from assuming a constant S-factor. For regions where we expect the S-factor to vary, the thinnest possible targets must be used. At low energies, this problem is reduced because the cross section quickly decreases towards the back of the target. This results in a small contribution from energies less than a few keV below the beam energy. For most energies, we judged a 10 keV target to be optimal. For the very low energy points, i.e. E_p < 200 keV, thicker targets provided a reasonable count rate. In this energy region, thick targets add only a small

systematic error because in this region there are no known resonances and a smooth, mainly direct capture, contribution to the S-factor. The behavior of the cross-section over the target is well understood and easily corrected for as prescribed by [Rol88]. In all cases, we assumed the S-factor was constant over the target thickness.

We profiled each target using the yield curve of the 259-keV resonance. The total (observed) thickness (Δ) extracted from the yield curve includes four components: energy loss in the target (Δ_t), beam straggle (Δ_s), beam resolution (Δ_b), and the resonance width (Γ). These quantities each contribute to the total thickness by adding in quadrature:

$$\Delta^2 = \Delta_b^2 + \Delta_s^2 + \Delta_t^2 + \Gamma^2 \qquad \text{Equation 4-13}$$

The value of Γ was measured previously [AjS91] and we measured Δ_b using an aluminum target (discussed in chapter 3). The values of Δ_s and Δ_t served as fitting parameters in the calculated yield curves. We determined the target dead layer from a shift in the resonance energy of the yield curve fits. This value was between 0.5 and 2 keV. Using the fit results, we calculated the target thickness at the beam energy from equation 4-10 for each target. The calculated thicknesses agreed well the observed thicknesses deduced from the widths of primary γ-ray peaks. Note that Δ_t is essentially constant over the interval between the beam energy and the effective energy.

After determining Δ_t and E_{dead} and assuming a constant S-factor, the effective energy was obtained from the integral of the cross-section over the target thickness:

$$\int_{E_{beam}-\Delta}^{E_{beam}} \frac{1}{E} e^{-2\cdot\pi\cdot\eta} dE = 2\cdot \int_{E_{eff}}^{E_{beam}} \frac{1}{E} e^{-2\cdot\pi\cdot\eta} dE \qquad \text{Equation 4-14}$$

We compared this calculation to effective energies derived from the primary γ-rays whose energies are given by:

$$E_\gamma^{primary} = E_{eff} + Q - E_x \qquad \text{Equation 4-15}$$

where E_x is the energy of the excited state and $E_\gamma^{primary}$ is the centroid energy of the primary γ-

ray peak. The measured and calculated values of E_{eff} agree to within the uncertainties γ-ray energies and detector calibration. A second, but less precise, check was performed by measuring the S-factor at the same effective energy using targets of differing thickness. For these points, the S-factors from different targets agree. Therefore, equation 4-14 was an accurate determination of E_{eff}.

4.6.5. Detector Gating

The two main detection schemes discussed in chapter 3 were both used in this project. The decay scheme of ^{15}O lends itself well to the Ge-NaI technique. For the ground state transition, which was normally the weakest branch and emits a single high energy γ-ray, the NaI annulus acted as an anti-coincidence shield, vetoing any coincident background. The amount of background reduction depends strongly on the beam energy. Almost all of the background resulted from beam induced sources. At energies where there was no $^{13}C(p,\gamma)^{14}N$ contamination, the veto reduced the background by more than an order of magnitude. Since the ground state was normally the weakest transition by far, the count rate of other transitions was normally sufficiently high and required no gating.

For energies below 187 keV where only the 6793 keV transition had an appreciable count rate, we used the annulus as an anti-coincidence shield. In this setup, the primary γ-ray deposits part of its energy in the NaI annulus and we observe the 6793 keV photopeak in the Ge detector. Since the primary γ-ray possesses only a few hundred keV of energy, we set a threshold on the NaI veto so that only γ-rays in the annulus above 1000 keV were vetoed. This reduced conincident background mainly from $^{11}B(p,\gamma)^{12}C$ which emits two high energy γ-rays. This technique also proved to be superior to that of demanding a coincidence between the Ge and NaI detectors. A coincidence requirement would reduce the overall detection efficiency by that of the NaI, approximately 66%.

The spectra shown in figure 4-8 demonstrate the power of this detection scheme. In the case shown here, a 650 keV γ-ray is coincident with a 6793 keV γ-ray. This first spectrum shows a Ge spectrum with a lead shield but no NaI anti-coincidence requirement. The second spectrum shows the Ge detector with a 1000 keV threshold veto on the NaI annulus.

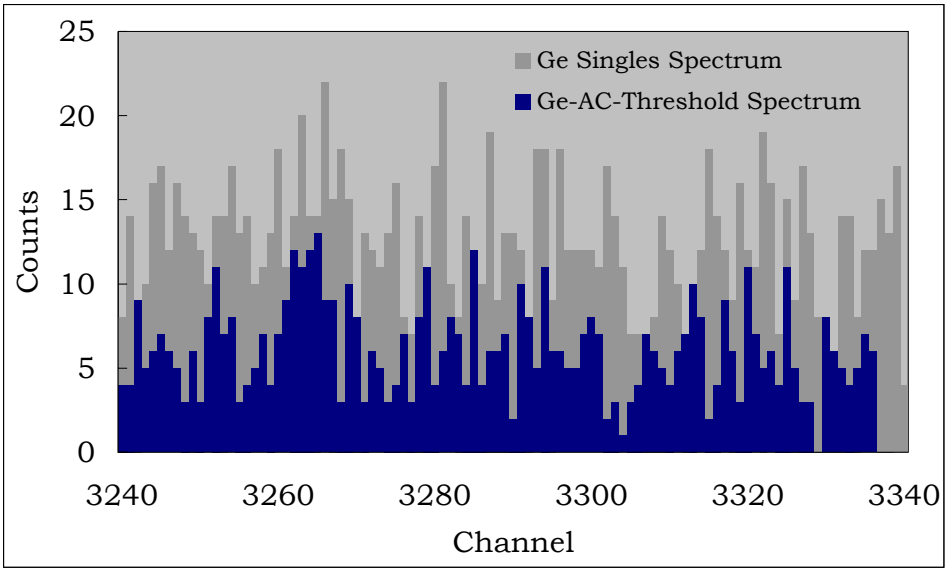

Figure 4-8: Ge singles vs. anti-coincidence spectra

4.6.6. Sum Corrections

Gamma-ray summing effects occur whenever coincident γ-rays are present – especially in close geometry. The two main effects result from "summing in", when false counts appear in a photopeak, and "summing out", when true counts are removed from a photopeak. Summing corrections were an important part of the final analysis. They primarily depend on the total detection efficiency, which required a significant amount of effort to measure and model. Fortunately, the decay scheme of ^{15}O is simple and well understood (see figure 4-6). This allows for relatively straightforward sum corrections. Unfortunately, the ground state, which is the most uncertain transition, is also most affected by summing. On the order of a half of the counts in the ground state photopeak resulted from coincident γ-rays from the 6176 and 6793 transitions.

Summing out refers to the case where a count is lost from a photopeak because a coincident γ-ray(s) also deposited some amount of energy, normally from Compton scattering. The probability for the coincident γ-ray to deposit any amount of energy is equal to the total detection efficiency. Therefore, the number of true counts that leave the photopeak is proportional to the product of the photopeak efficiency and the total efficiency for detecting the coincident γ-ray. With this relationship, the observed γ-ray intensity can be corrected. For

example, in a case where γ_1 is detected but γ_2 is in coincidence:

$$N_1^{observed} = N \cdot \eta_{photopeak}(\gamma_1) - N \cdot \eta_{photopeak}(\gamma_1) \cdot \eta_{total}(\gamma_2) \quad \text{Equation 4-16}$$

where N is the total number of decays. Rearranging for the total number of decays results in:

$$N = \frac{N_1^{observed}}{\eta_{photopeak}(\gamma_1)} \cdot \left[\frac{1}{1 - \eta_{total}(\gamma_2)} \right] \quad \text{Equation 4-17}$$

Using this technique, we corrected all intensities except for the ground state. In all of these cases, two coincident γ-rays are emitted. For example, at a beam energy of 200 keV, the sum correction for the 6793 keV transition is 1.30, i.e. 30% of the γ-rays were lost. Because of the large corrections involved, the absolute efficiency was an important contribution to the overall uncertainty.

This effect was reversed for the ground state transition. The number of observed γ-rays in the ground state is not only a function of the number of ground state γ-rays created, but also of the number of 6176 keV and 6793 keV transitions[22]. This results from the fact that these transitions emit two γ-rays that can both simultaneously deposit their full energy in the detector. The probability of both γ-rays to deposit their full energy is simply the product of their photopeak efficiencies. Consequently, the number of observed ground state γ-rays is related to the number of emitted γ-rays through the following relationship:

$$N_{g.s.} = N_{g.s.}^{observed} \eta(E_{g.s.}) - N_{6176} \eta(6176) \eta(E_{primary}) - N_{6793} \eta(6793) \eta(E_{primary}) \quad \text{Equation 4-18}$$

where the N_{6176} (N_{6793}) refers to the number of 6176 (6793) transitions given by the previous equation. This technique corrected the ground state intensities; although the size of the correction varied significantly, an example correction was 0.50 at 365 keV, i.e. 50% of the counts were false events!

[22] It is also a function of the other branches because they all add up to the ground state γ-ray energy. However, the other transitions are small branches.

4.6.7. Angular Distributions

For all measurements, the detector location was 1 cm from the target and 0 degrees from the beam axis. Despite the large solid angle in close geometry, the measured yields must be corrected for angular distribution effects. The angular distribution coefficient is normally expressed in terms of Legendre polynomials:

$$W(\theta) = 1 + \sum_k a_k \cdot Q_k \cdot P_k(\theta) \quad for\ k = 1, 2, \ldots \qquad \text{Equation 4-19}$$

where a_k are expansion coefficients, Q_k are the detector attenuation coefficients (i.e. how much effective solid angle the detector covers at a specific γ-ray energy), and P_k are Legendre polynomials. Because of the close geometry and large crystal size, the Q_k values are generally small indicating the large detector solid angle. The expansion coefficients can be determined from fitting angular distribution data with equation 4-19.

Schröder et al. measured the angular distributions for most transitions between 235 and 3000 keV (although for low energies they observed only the strongest transitions). The primary γ-rays exhibited some angular dependence, especially in the 6793 keV transition. However, the secondary γ-rays did not show an angular dependence. The 259 keV resonance primarily proceeds through $\ell = 0$ capture which emits isotropic γ-rays. Since this resonance dominates the low energy S-factor, the results of Schröder et al. are not surprising. The two resonances at -504 and 987 keV also proceed through $\ell = 0$ capture. These resonances are the only significant contributions to the 5183 and 6176 keV transitions. The 6793 keV transition also has a significant direct capture component which direct capture theory predicts to be isotropic. This is also true of the ground state. This is consistent with the results of Schröder et al. which displayed no anisotropy at 850 keV (a region of purely direct capture in the 6793 keV transition). As a result, no angular corrections for any of the observed secondary transitions were necessary.

4.6.8. S-factor Results

We obtained experimental S-factor results from the observed γ-ray yields, target thicknesses, detector efficiencies, and sum corrections at each energy. Figure 4-9 displays these data. In total, 37 different energies were measured. In certain cases, points were

repeated at almost exactly the same energy in order to test the reliability and reproducibility of the measurements. Averaging these points left 30 independent measurements. The transitions within each measurement had very different statistical uncertainties depending on the particular energy. Aside from this, they all shared systematic uncertainties which I list in table 4-2.

Systematic Error Estimates	
Source	Error (%)
Aboslute Photopeak Efficiency	5
Absolute Total Efficiency	5
Charge Integration	3
Target Nuclei Density	7
Total	10

Table 4-2: Experimental error estimates

The uncertainties in efficiencies were based on the level of agreement between calibration data and MCNP calculations. For example, in the case of the absolute total efficiency, we scaled the MCNP calculation by 1.01 to match the calibration data. However, the three data points showed a small amount of scatter around this curve yielding an overall uncertainty of 5%. The charge integration uncertainty was based on three factors: i) our ability to reproduce well measured resonance strengths in Aluminum, ii) comparing the total beam current to the current observed on apertures near the target and iii) comparing the beam current with the electron suppression bias on and off. The uncertainty in the target atom density resulted mainly from the uncertainty in the 259 keV resonance strength.

The experimental errors associated with each data point vary, mostly due to statistics. The combined statistical and systematic errors are present in figure 4-9 and all future figures. Uncertainties resulting from statistics, sum corrections and target effects (we used many targets) are not correlated between individual data points, but those arising from the photopeak efficiency and beam integration are correlated. This implies that the majority of errors, especially at low energies, are not correlated. We assumed this in the analysis discussed

in chapter 5.

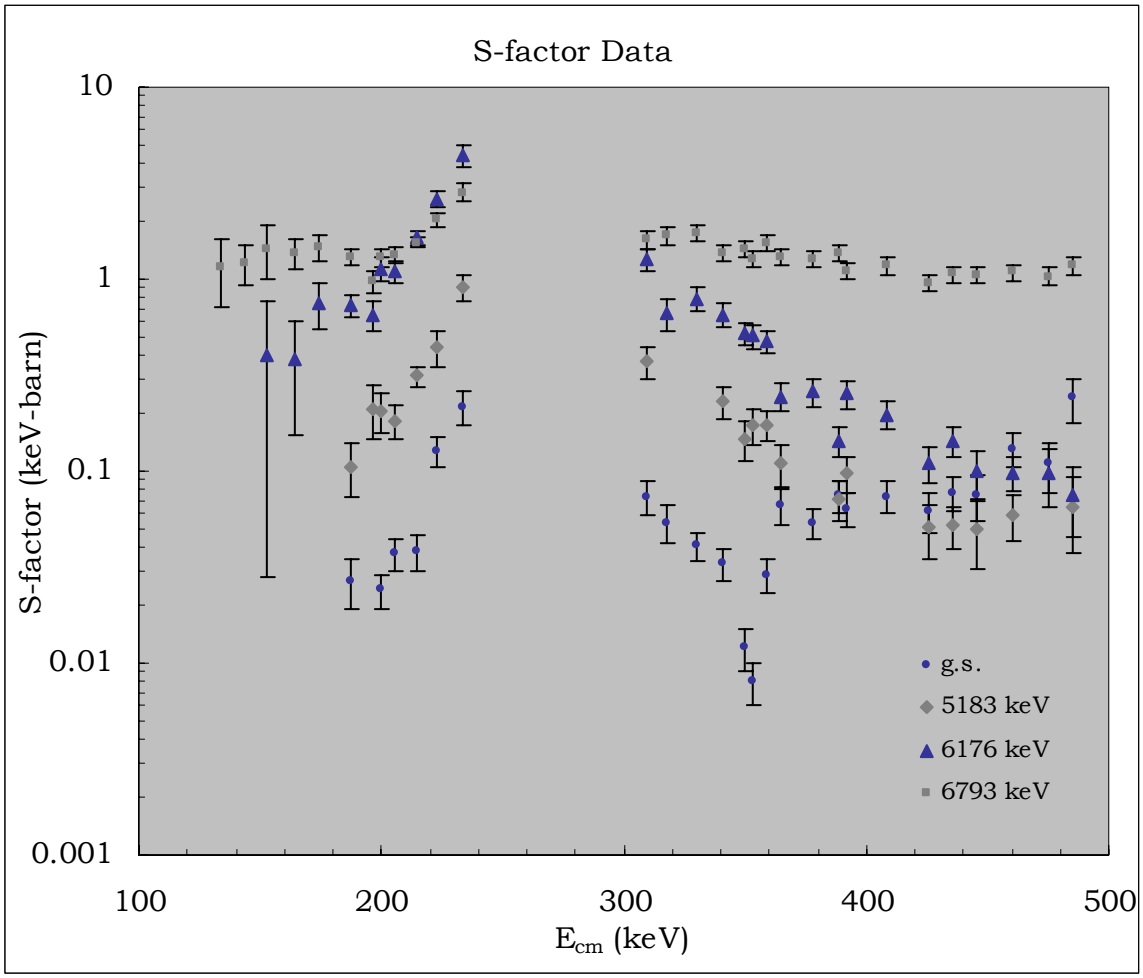

Figure 4-9: S-factor results

Chapter 5:

Results and Implications

5.1 S-factor Extrapolations

Our S-factor measurements extend down to 133 keV. In order to determine the S-factor at lower energies and also to test the feasibility of future measurements, which will be taken over long periods of time with many targets, we must reliably extrapolate the existing data. The extrapolations performed in this work rely on the direct and resonance capture formalism discussed in chapter 2. This theory is certainly incomplete, but at low energies, where only a few states dominate the reaction process, it is a reasonable approximation. The crucial test is agreement between independent measurements of normalization parameters and best-fit values from experimental data. We performed direct capture calculations for each transition and normalized the results using C^2S values derived from $^{14}N(^3He,^2H)^{15}O$ studies [Ber02]. For the extrapolations, we considered all resonances below 3000 keV and a direct capture contribution when suggested by the data. The structure exhibited by each transition varies widely and consequently I discuss them individually below.

5.1.1. Direct Capture Calculations

We calculated the single-particle direct capture contribution for each transition using the code CAP [Tho03]. This calculation uses a nuclear interaction represented by the Woods-Saxon potential with adjustable radius and diffuseness parameters. Differing somewhat from Schröder et al., who used values of 4.09 and 0.7 fm, we assumed 3.2 and 0.7 fm for the radius and diffuseness which are based on analyses of stripping reactions [Ber02]. The nuclear potential depth was normalized to the binding energy for each state. A Coulomb term was added to the potential:

$$V(r) = \begin{cases} r < R_o & \dfrac{-V_o}{1+e^{\frac{r-R_o}{a_o}}} \\ r > R_o & \dfrac{-V_o}{1+e^{\frac{r-R_o}{a_o}}} + \dfrac{Z_p Z_N}{4\cdot\pi\cdot\varepsilon_o}\cdot\dfrac{1}{r^2} \end{cases}$$ Equation 5-1

In ^{14}N + p, there are two possible channel spins, $1/2^+$ and $3/2^+$ and we considered both of these possibilities. In each transition, the E1 operator dominates and thus we neglected contributions from other operators. We considered all incident angular momentum $\ell_i \leq 3$.

Figure 5-1 shows an example of the nuclear and Coulomb potential, along with wave functions, used in these calculations. We calculated the bound state wave functions, u_b, from this potential. The unbound (incident) wave functions were calculated using the regular and irregular Coulomb functions. The overlap amplitude ($u_b \cdot O(E1) \cdot u_c$) integrated over all space determines the probability of capture into the single particle state bound within the potential well (see equation 2-9). We then normalize this cross section using the C^2S values in table 2-2 and equation 2-10.

In the next four sections, I present the results of these calculations combined with the contribution from various resonances. In most cases, the only important resonance is at 259 keV. We compared these calculations to the experimental data by varying C^2S and Γ_γ as fitting parameters. I discuss the transitions that contribute to the cross section at low energies in order of importance.

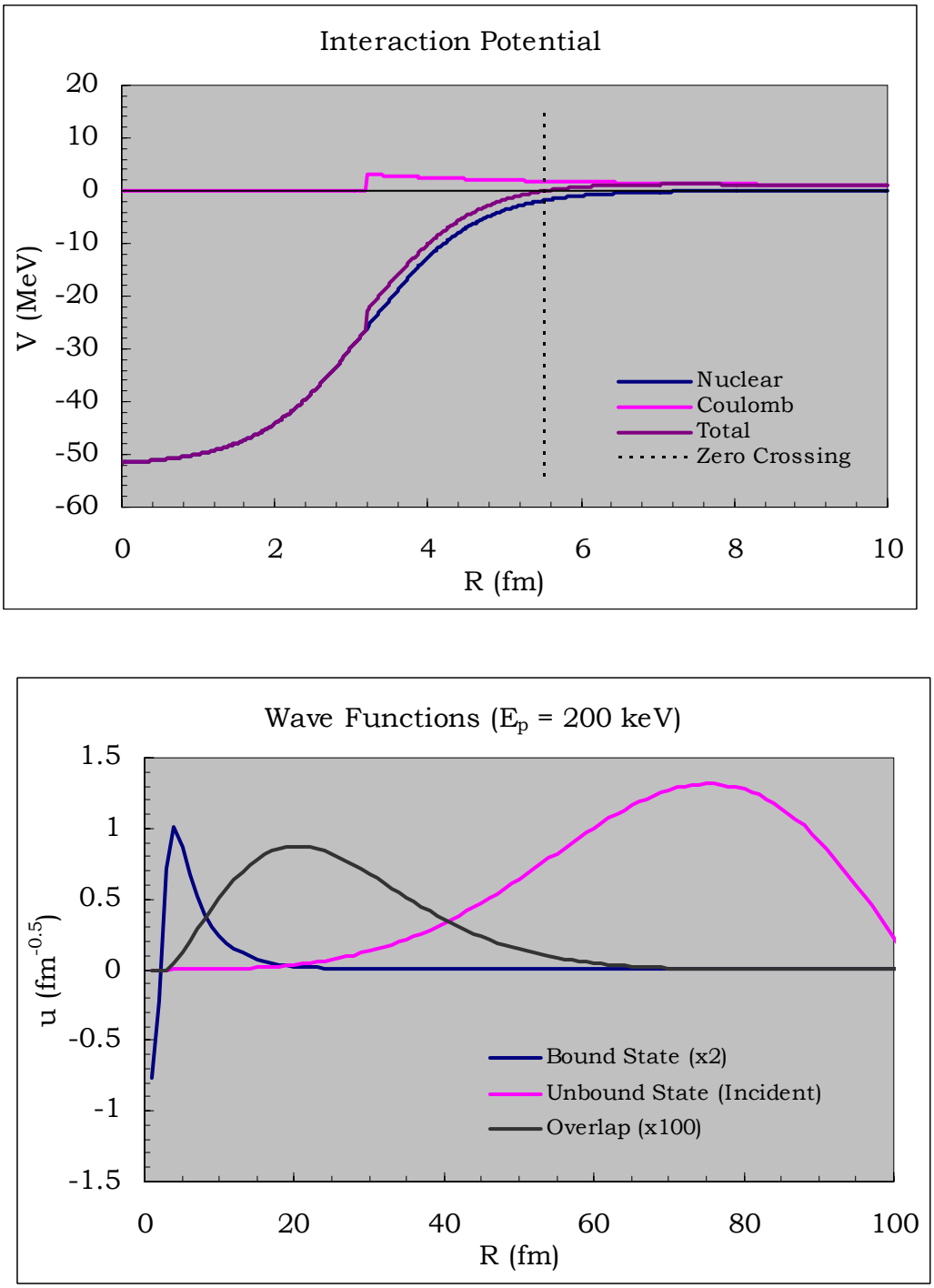

Figure 5-1: Direct capture interaction potential.and wave functions

The interaction potential (top) and wave functions (bottom) calculated for direct capture into the 6793 keV state at a proton energy of 200 keV. Note the large influence of the diffuseness parameter on the nuclear potential. For all transitions, the E1 operator dominated and the overlap is the product of $u_b \cdot O(E1) \cdot u_c$, which is the integrand in equation 2-9. The bound wave function and overlap were scaled to reveal their structure.

5.1.2. The 6793 keV Transition

The experimental data for this transition clearly demonstrate two distinct reaction mechanisms. The first is a resonance contribution centered at 259 keV with underlying direct capture that is relatively constant from 187 keV up to 2500 keV. This is an enormous energy range and demonstrates the existence of two distinct processes: one resonant and one non-resonant. The $\ell_i = 1$ direct capture component dominates the low energy region. At higher energies near 2000 keV the $\ell_i = 3$ term becomes significant, but it is suppressed by a smaller spectroscopic factor. The calculations accurately reproduce the data through the entire energy range of our results and those of Schröder et al.. The angular momentum coupling predicts no interference between the 259 keV resonance (s-wave) and the direct capture (p-wave) which is consistent with the experimental data. As a result, we fit the S-factor with an incoherent sum of resonance and direct capture while leaving C^2S and Γ_γ as free parameters:

$$S_{total}(E) = S_{dc}(E) \cdot C^2S + S_{259}(E) \qquad \text{Equation 5-2}$$

I show a comparison of the fit results and experimental values in table 5-1. The close agreement between the fit and experimentally derived values (normalized $\chi^2 = 1.29$) lends credence to the validity of the extrapolation. We estimated errors on the fitting parameters from varying the normalized χ^2 value by 1. This is valid for uncorrelated errors (see chapter 4 and [Bev92]). The best fit value of 0.65(8) agrees well with the value derived from stripping. The γ-decay width also shows good agreement with the value derived from the resonance strength[23]. However, it is not well constrained by the fit since the data mainly result from direct capture. The agreement between best fit parameters and results from indirect measurements further implies a reliable fit. This agreement is crucial because the 6793 keV transition comprises approximately 90% of the total S-factor.

Our fit lies significantly lower than that of Angulo et al. throughout the entire low energy region. This is not surprising since the Angulo et al. fit is significantly higher than the data at higher energies. In contrast, our result does agree well with that of Schröder et al. but the present results extend to lower energies and better constrain the fit.

[23] For a narrow resonance such as the 259 keV resonance, Γ_γ follows directly from $\omega\gamma$, i.e. $\Gamma_\gamma = \gamma$ (see section 4.2.2).

Parameter	Experimental	Fit
C^2S	0.57 (12)	0.65 (8)
Γ_γ (μeV)	42 (3)	46 (17)
	χ_ν^2 = 1.29	

Table 5-1: Fit results for the 6793 keV transition

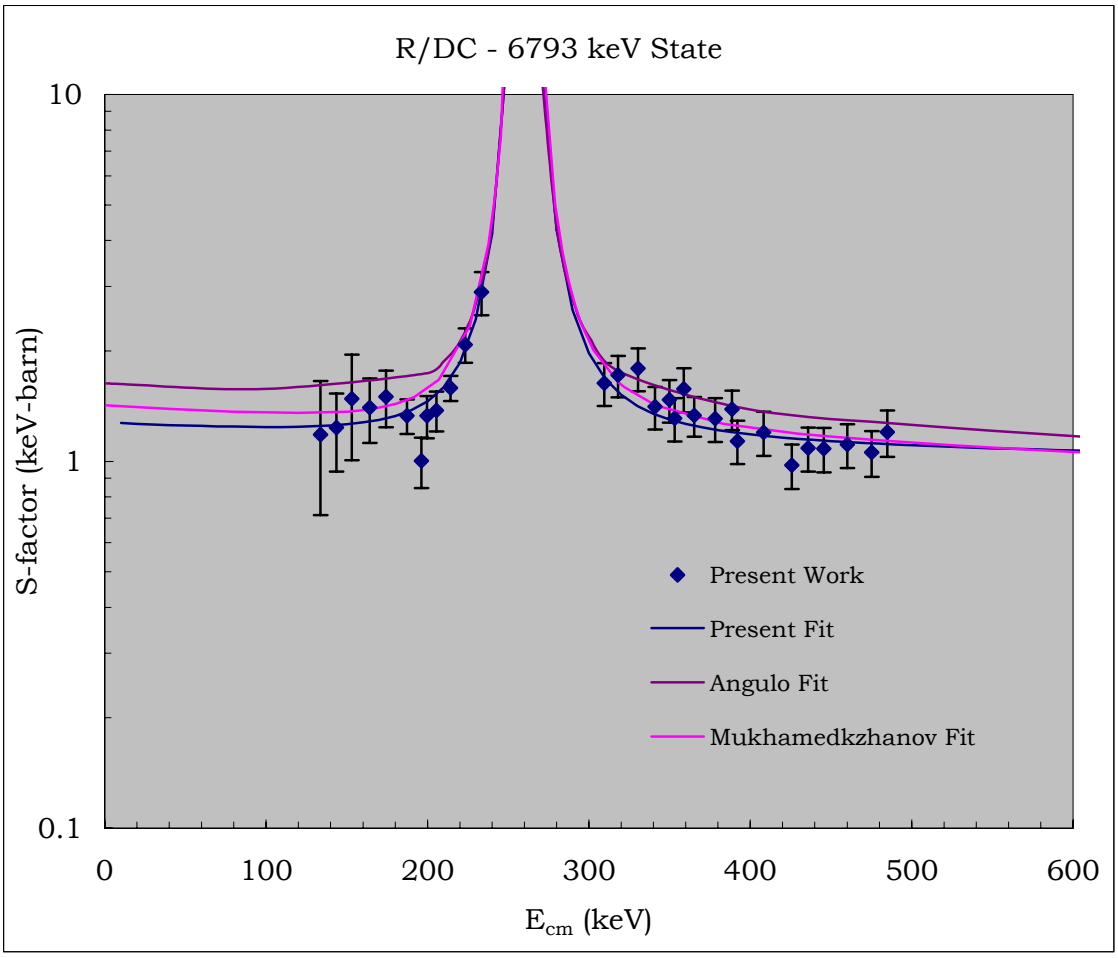

Figure 5-2: S-factor for the 6793 keV transition

5.1.3. The 6176 and 5183 keV Transition

The 6176 and 5183 keV transitions have identical reaction mechanisms. Resonances at 259, 987 and 1447 keV dominate the low energy region. Interference between the two $1/2^+$ resonances at 259 and 1447 keV is possible but the effects would be small and there is no evidence of interference in the data. Although the C^2S value from Bertone et al. predicts a large direct capture contribution, there is also no evidence of direct capture in the data.

Consequently, we neglected direct capture and interference in the fit and only kept Γ_γ(259 keV) as a free parameter. The S-factor was thus an incoherent sum of three resonances:

$$S_{total}(E) = S_{259}(E) + S_{987}(E) + S_{1447}(E) \qquad \text{Equation 5-3}$$

In both cases, the fit agrees well with the experimental data having normalized chi-squares of 1.74 and 3.30. In both cases, we deduced the Γ_γ error as discussed in the 6793 keV transition. Their Γ_γ values agree with the resonance strength measurement.

For both transitions, the present experimental data agree well with those of Schröder et al. on the low energy tail of the 259 keV resonance. In the energy region between 300 keV and 500 keV the present results are somewhat higher. This is not of great concern since only the low energy region is astrophysically relevant.

The fit of the 6176 keV transition gives an S(0) values approximately one third lower than the Angulo et al. R-matrix fit. Both our fit and that of Angulo et al. are much lower than the Schröder et al. fit which shows a mysteriously asymmetric 259 keV resonance. This is a significant difference and the new low energy data do not support the Schröder et al. fit. With either the R-matrix or present fit, this state comprises a small contribution to the total S-factor.

Angulo et al. did not analyze the 5183 keV transition but the present results agree well with the Schröder et al. fit. Their data are not present in figure 5-3, but both data sets contain an apparent leveling off in the data near 500 keV. Both fits give the same S(0) value within 1σ.

Parameter	Experimental	Fit (6176 keV)	Fit (5183 keV)
Γ_γ (μeV)	42 (3)	51 (10)	34 (15)
χ_ν^2		1.74	3.30

Table 5-2: Fit results for the 6176 and 5183 keV transitions

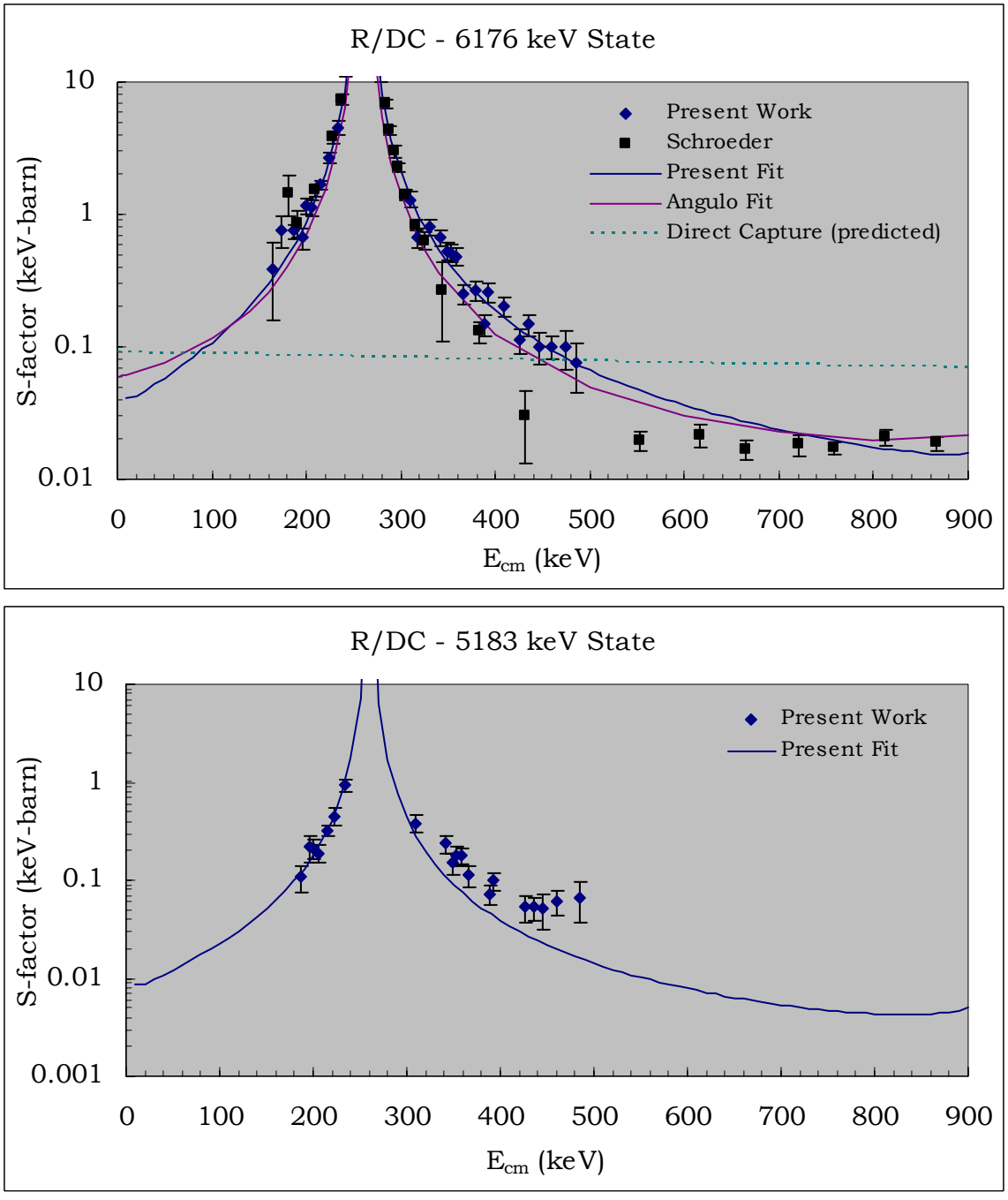

Figure 5-3: S-factor for the 5183 and 6176 keV transitions

5.1.4. The Ground State Transition

The ground state transition has the most complex structure with five possible contributions: direct capture, a possible sub-threshold resonance at -504 keV and resonances at 259, 987, and 2187 keV. Furthermore, its large C^2S value implies a direct capture contribution which, by itself, would be far above the observed data. There are two possible explanations. First, strong interference is possible between the direct capture and each of the four resonances. Interference can considerably reduce the direct capture contribution. Second, the complex reaction mechanism of this state may push the limits of the direct and resonance capture model rending the fits inaccurate. Further complicating the extrapolation, the three resonances at -504, 987, and 2187 keV may also interfere with each other. Keeping all possible interference terms, the angle integrated ground state S-factor contains nine terms:

$$\begin{aligned} S_{tot}(E) = {} & S_{dc}(E) + S_{-504}(E) + S_{259}(E) + S_{987}(E) + S_{2187}(E) + \\ & \pm 2 \cdot \sqrt{S_{dc}(E) \cdot S_{-504}(E)} \cdot \cos\left[\delta_{dc} - \delta_{-504}\right] \\ & \pm 2 \cdot \sqrt{S_{dc}(E) \cdot S_{259}(E)} \cdot \cos\left[\delta_{dc} - \delta_{259}\right] \\ & \pm 2 \cdot \sqrt{S_{dc}(E) \cdot S_{987}(E)} \cdot \cos\left[\delta_{dc} - \delta_{987}\right] \\ & \pm 2 \cdot \sqrt{S_{dc}(E) \cdot S_{2187}(E)} \cdot \cos\left[\delta_{dc} - \delta_{2187}\right] \\ & \pm 2 \cdot \sqrt{S_{-504}(E) \cdot S_{987}(E)} \cdot \cos\left[\delta_{-504} - \delta_{987}\right] \\ & \pm 2 \cdot \sqrt{S_{-504}(E) \cdot S_{2187}(E)} \cdot \cos\left[\delta_{-504} - \delta_{2187}\right] \\ & \pm 2 \cdot \sqrt{S_{987}(E) \cdot S_{2187}(E)} \cdot \cos\left[\delta_{987} - \delta_{2187}\right] \end{aligned}$$

Equation 5-4

There are five normalization parameters in the above expression: C^2S_{gs} and four resonance strengths. There are an additional seven arbitrary signs. We varied the signs of the interference terms in order to best reproduce the shape of the observed data. Even with five parameters, we found no satisfactory fit. The direct capture contribution is simply too large to be consistent with data on both sides of the 259 keV resonance. However, without a significant direct capture contribution in the region 500 keV to 900 keV the data of Schröder et al. are not reproduced. We conclude that for this transition the direct and resonance capture theory is not sufficient. Despite the fact that we found no convincing fit over the entire energy range where data exist, in the region below 400 keV, the data are relatively well described by

the 259 keV resonance alone. Since the Gamow window resides below 259 keV for main sequence environments, the lack of understanding the higher energy data should not effect the nuclear reaction rates below 10^8 K.

We fit the experimental data below 400 keV assuming only a 259 keV resonance contribution. The fit results are not as convincing as the previous fits with a normalized chi-square of 4.06. This results from the fact that we are simplifying the reaction mechanism considerably. They serve only as estimates and, as a result, I do not quote an error. This is not problematic because, even if our $S_{g.s.}(0)$ value is increased by a factor of 10, it would only compose approximately 1 percent of the $S_{tot}(0)$. Our data restrict the ground state transition to a small contribution of the total S-factor.

Our result differs significantly from that of Schröder et al. and Angulo et al.. As discussed in chapter 2, the Schröder et al. extrapolation is no longer valid. The present fit and that of Angulo et al. demonstrate the fundamental problem of nuclear astrophysics: the low energy data agree well with *both* fits but the fits diverge below the lowest energy data. Even though there is a factor of 40 difference in the S(0) values, the ground state contributes only a few percent to the total S-factor in either case.

Parameter	Experimental	Fit
C^2S	1.6(3)	0
Γ_γ (μeV)	42 (3)	57
$\chi_\nu^2 = 4.06$		

Table 5-3: Fit results for the ground state transition

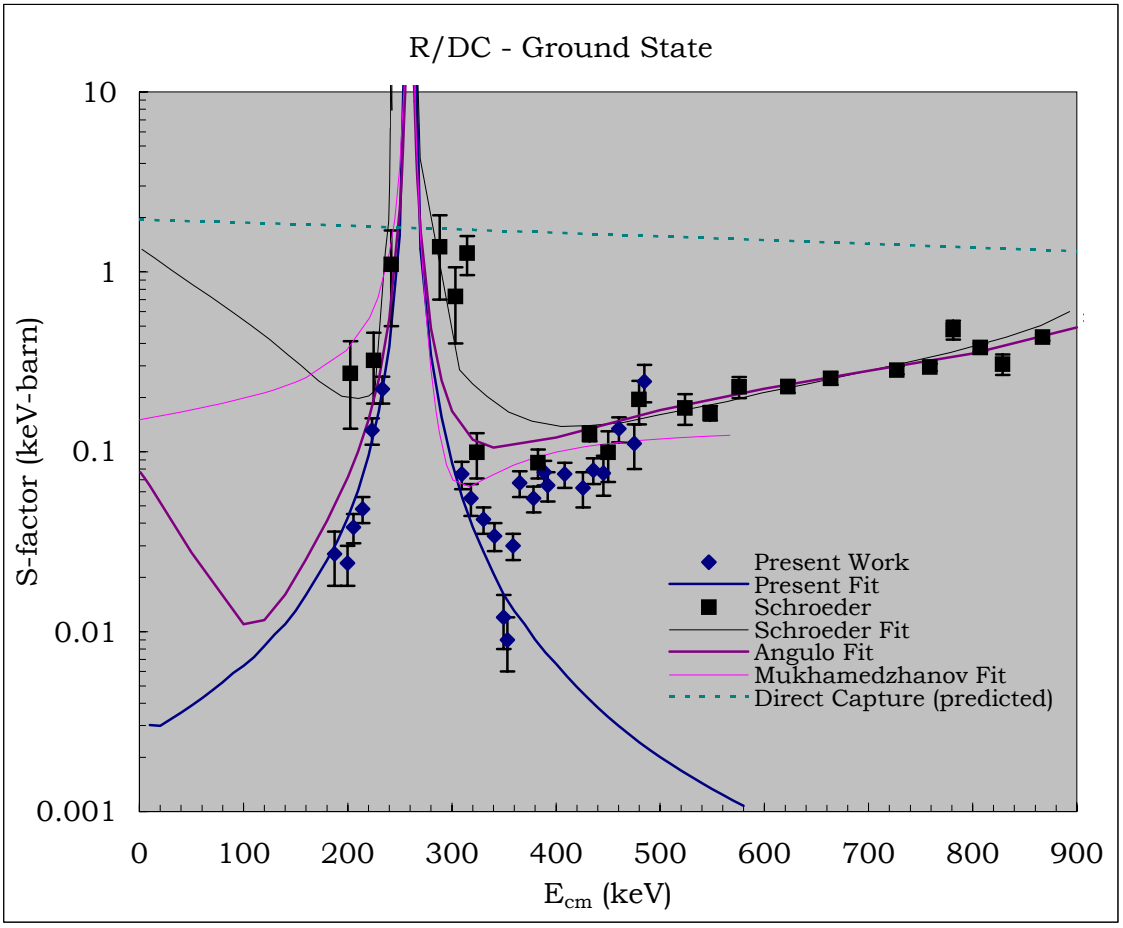

Figure 5-4: S-factor for the ground state transition

The new data are better able to constrain the fits. Although there is significant discrepancy between the present and Angulo et al. fits, neither one contributes significantly to the total S-factor.

5.1.5. The 5241, 6859 and 7276 Transitions

The experimental data indicate that the low energy S-factors for the 5241, 6859 and 7276 keV transitions are (almost) exclusively direct capture. Primarily because of their high spins ($5/2^+$, $5/2^+$, $7/2^+$) they are not measurable branches in the decay of any low energy resonances and have small direct capture contributions. This makes them difficult to detect and we have little new data. In spite of this, we can estimate their contribution to the total S-factor. Since there were not enough data to constrain a fit, we simply calculated their direct capture contributions using spectroscopic factors from Bertone et al..

Both the 6859 and 7276 transitions almost exclusively proceed through the 5241 keV state

(they have 100 and 96 percent branches). Measuring the 5241 keV γ-ray yield is therefore a measure of the total contribution from all three states. The new data are consistent with the calculations.

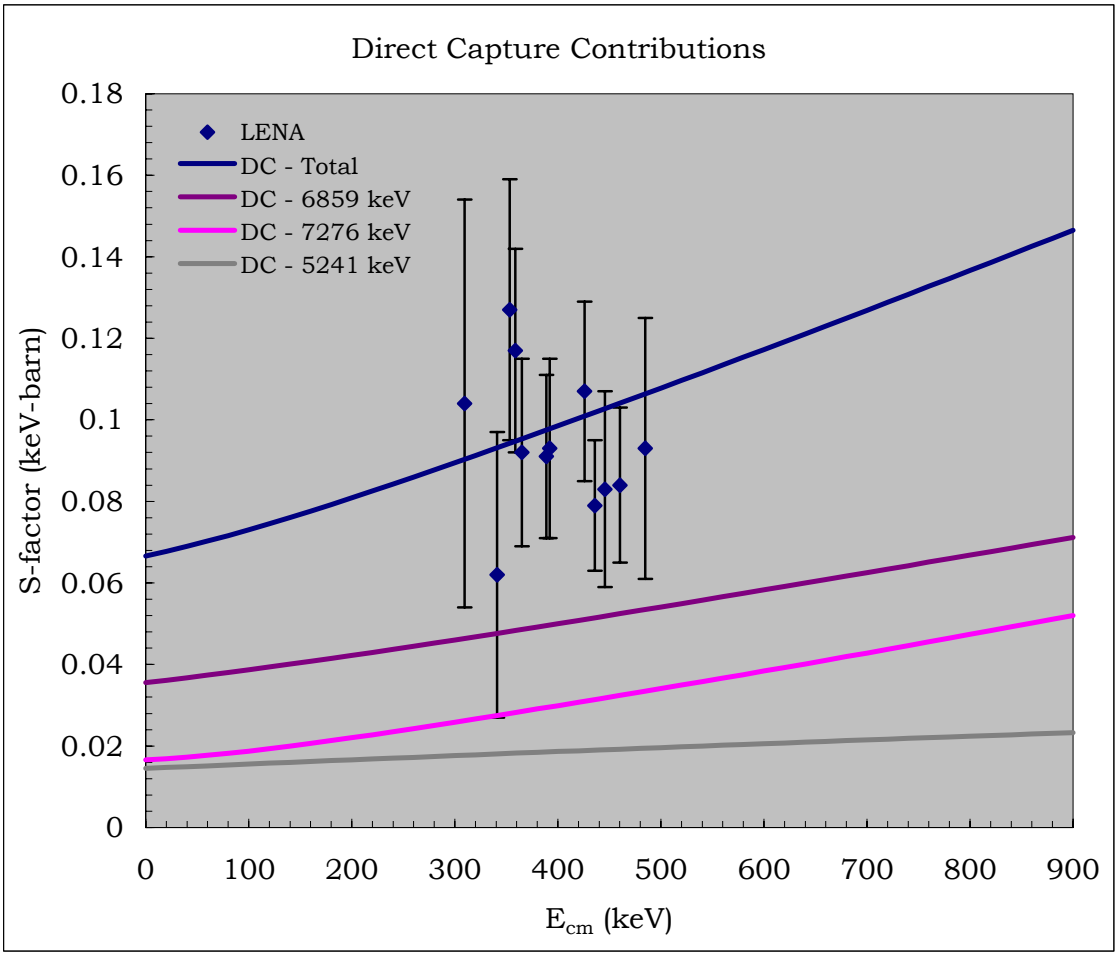

Figure 5-5: Direct capture contribution from the 5241, 6859 and 7656 keV transitions

5.1.6. The Total S-factor

On the whole, our new S-factor data are for the most part consistent with Schröder et al. but show less scatter. Most importantly, these data extend to significantly lower energies. This is especially true in the ground state where the present data points extend almost 100 keV lower in energy. This neglects Schröder et al.'s three lowest ground states data points, which had very large error bars. Our results are significantly lower in this region.

The total S-factor is calculated from the incoherent sum of the individual transitions. Our

total S-factor is significantly below the results of Lamb and Hester and we assume the normalization of their data is in error. Figure 5-6 compares the total S-factor results with previous studies. Note that the points only extend down to 153 keV where all major transitions could be measured, even though we measured individual transitions below this energy. Thus there are constraints on the curve that are not apparent in the figure.

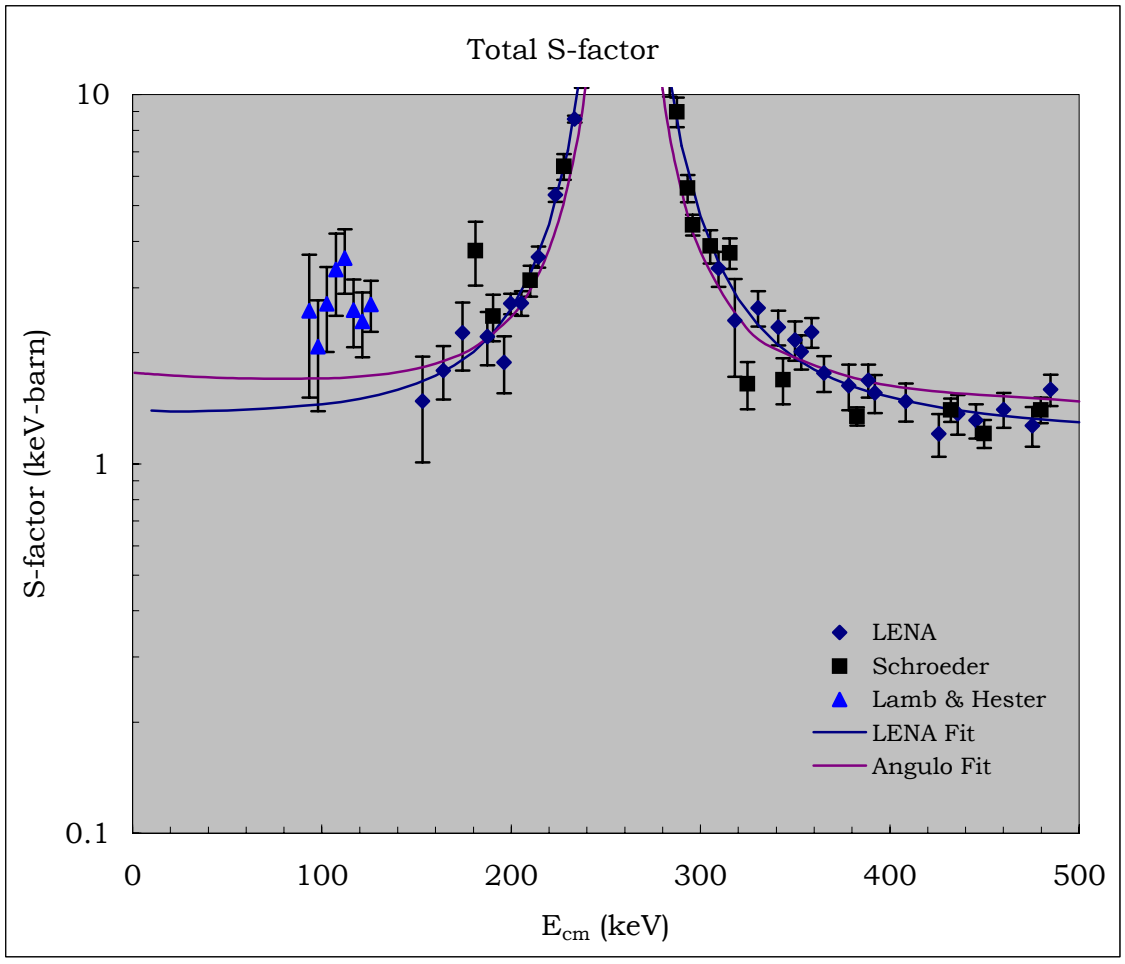

Figure 5-6: Total S-factor results

Since the S-factor is generally flat in the low energy region, stellar modelers frequently assume a constant S-factor equal to the $S_{tot}(0)$ value. Table 5-4 lists S(0) for each transition. Our extrapolations are significantly lower than those of both Angulo et al. and Schröder et al.. The present ground state data, which precludes a large sub-threshold contribution, lowers their large ground state contribution from 1.55 keV·barn to 0.0023 keV·barn. This itself accounts for about a 50% reduction in $S_{tot}(0)$. Our ground state analysis is consistent with the lower

limit of the Angulo et al. extrapolation. However, their value for capture into the 6793 keV state is approximately 25% larger than our low energy data suggest. Since the 6793 keV state is the dominant transition, this is a significant deviation. Our total S-factor value has a 12% uncertainty; this is comparable to uncertainties quoted by Angulo et al. but smaller than the 17% reported by Schröder et al.. In addition, Adelberger et al. suggested the uncertainties quoted by Schröder et al. were significantly underestimated. They estimated an $S_{tot}(0)$ between 1.9 and 3.9 keV·barn from the Schröder et al. data. Our result reduces this range considerably.

It is important to note that the quoted uncertainty of 12% on $S_{tot}(0)$ results from the statistical constraint on the fit by our data. Absolute cross section measurements are prone to systematic errors in charge collection, detection efficiency and target composition. We strove to minimize any systematic errors, but it is possible that an overall normalization error, systematic to our setup, is present in the data. We estimate this systematic error to have a maximum of 10%.

S(0) Values [keV-barn]			
Transiton	Present	[Ang01]	[Sch87]
R/DC → G.S.	0.0023	0.08 (9)	1.55 (34)
R/DC → 5183 keV	0.011 (5)	-	0.014 (4)
R/DC → 5241 keV	0.015 (3)	-	0.018 (3)
R/DC → 6176 keV	0.042 (8)	0.06 (2)	0.14 (5)
R/DC → 6793 keV	1.26 (19)	1.63 (17)	1.41 (2)
R/DC → 6859 keV	0.036 (8)	-	0.042 (1)
R/DC → 7276 keV	0.017 (4)	-	0.022 (1)
Total	1.39 (17)	1.77 (20)	3.20 (54)

Table 5-4: S(0) values

5.2 Reaction Rates

Most stellar model calculations still use the results of Schröder et al., as recommended by the NACRE compilation [Ang99]. Since our $S_{tot}(0)$ value is 43% of the value used in their calculation, our new reaction rates differs significantly at temperatures below 10^8 K. In addition, the rates suggested by Angulo et al. are twice the NACRE value just above 10^8 K where the 259 keV resonance dominates. At higher energies (E >250 keV), the well

understood resonances dominate the reaction rate and we believe the rates suggested by Angulo et al. are incorrect. The new S-factor results therefore agree with the NACRE values in this energy regime. For lower energies, relevant to main sequence hydrogen burning, the new reaction rates are significantly lower. Table 5-5 lists the reaction rates calculated from our S-factor extrapolations.

Temperature (T_6)	Reaction Rate ($N_A\langle\sigma v\rangle$)		Ratio
	Present	NACRE	Pres./NACRE
8	5.7E-25	1.0E-24	0.55
9	9.8E-24	1.8E-23	0.55
10	1.1E-22	2.1E-22	0.54
11	9.6E-22	1.8E-21	0.54
12	6.4E-21	1.2E-20	0.54
13	3.5E-20	6.4E-20	0.54
14	1.6E-19	3.0E-19	0.54
15	6.5E-19	1.2E-18	0.54
16	2.3E-18	4.2E-18	0.54
18	2.2E-17	4.0E-17	0.54
20	1.5E-16	2.8E-16	0.54
25	7.1E-15	1.3E-14	0.54
30	1.4E-13	2.5E-13	0.55
40	9.9E-12	1.8E-11	0.55
50	2.1E-10	3.7E-10	0.56
60	2.1E-09	3.7E-09	0.57
70	1.3E-08	2.3E-08	0.58
80	6.1E-08	1.0E-07	0.59
90	2.2E-07	3.7E-07	0.60
100	6.8E-07	1.1E-06	0.61

Table 5-5: Reaction rates

5.3 Implications

The new $^{14}N(p,\gamma)^{15}O$ reaction rate has a significant impact on hydrogen burning. Since our reaction rate is approximately half of the previously recommended value, it is tempting to assume that hydrogen burning in massive stars will last twice as long as previously thought. This logic is flawed. The consequences of a lower reaction rate are not necessarily obvious or intuitive because of the strong interdependence of stellar model parameters. For example, a

slower reaction rate may result in less energy production, which could allow the core to contract. The core might then become denser and hotter than previously, which would increase the reaction rate, and cancel the effects of a lower S-factor.

In spite of this, a few general implications are clear. First, a slower $^{14}N(p,\gamma)^{15}O$ reaction rate means a slower CN cycle. This increases the temperature where the CN cycle overtakes the proton-proton chain in energy production. The shift is approximately 6% from 17 to $18 \cdot 10^6$ K.

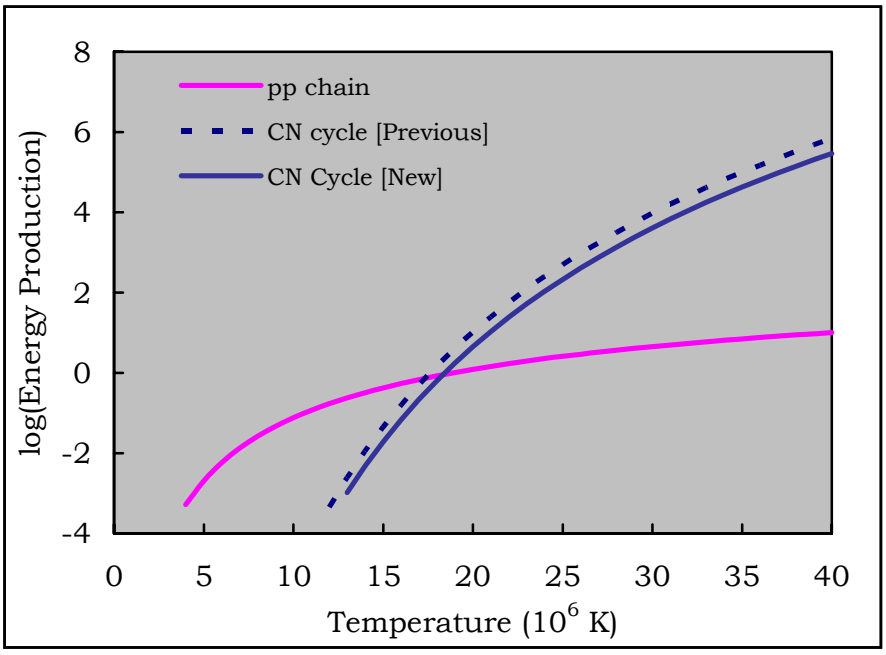

Figure 5-7: New rate of CN cycle energy production

Secondly, stars that produce most of their energy via the CN cycle will experience a longer main-sequence lifetime despite an increase in core temperature and density. This implies that for a star of a particular age the main sequence turn-off (MSTO) shifts to higher temperatures. This effect will be greatest in stars of relatively young clusters where the MSTO point presently resides in massive stars. In the oldest globular clusters, stars in the vicinity of one solar mass reside at the MSTO. At these masses, the CN cycle produces a small fraction of the total luminosity for most of the main-sequence lifetime. Nevertheless, as the star evolves on the main-sequence, the core temperature rises as helium is produced in the core. During this time

period, the CN cycle becomes important and a lower rate significantly alters the star's evolutionary timescale. This effect can be clearly seen by simulating the evolution of a star typically found at the MSTO in an old cluster. For a $0.8 \cdot M_{sun}$ star, with low metallicity ($10^{-2} \cdot Z_{solar}$), a simulation reveals that the lower $S_{tot}(0)$ value increases the MSTO age by approximately 0.8 Gy [Cha03].

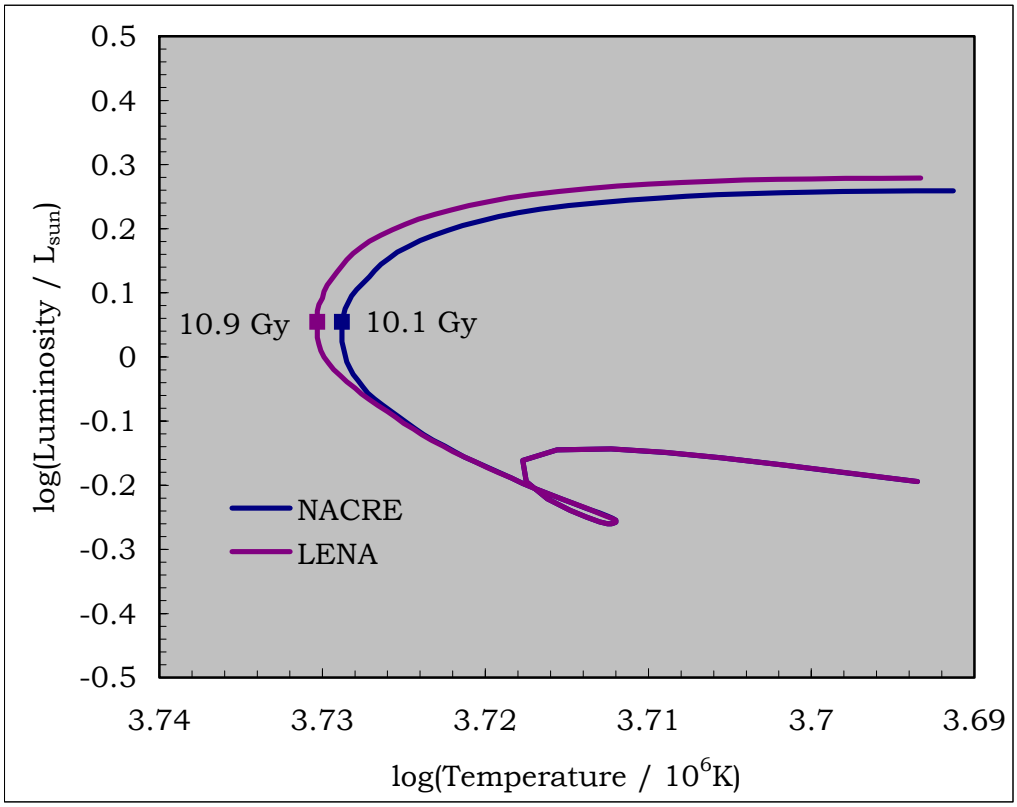

Figure 5-8: Evolutionary track of a $0.8 \cdot M_{sun}$ star

The metallicity assumed here was $0.01 \cdot Z_{sun}$ which is typical of a star near the MSTO in an old cluster. Note that the evolutionary tracks are indistinguishable until the star approaches the MSTO. At this point, hotter core temperatures make the CN cycle an important contribution to energy production.

This example illustrates the main-sequence evolution of an individual star. In dating globular cluster stars, evolutionary tracks for thousands of stars must be evolved. Modelers use Monte Carlo simulations to vary the relevant parameters in order to determine a best fit isochrone for an individual globular cluster. These calculations are numerically intensive and

were not repeated here. Simulations previously calculated by Chaboyer et al. highlight seven crucial parameters that significantly effect globular cluster ages at the bounds of their present uncertainties [Chb96]. The top four in order of importance are the oxygen abundance [O/Fe], mixing length, primordial helium abundance and $^{14}N(p,\gamma)^{15}O$ reaction rate.

These models use the results and uncertainties quoted by Schröder et al.. Chaboyer et al. estimated that a 2σ change in those values results in a 3% change in the globular cluster age. Our new $S_{tot}(0)$ value is 3.3σ lower and in turn increases the mean age of the 17 oldest globular clusters from 12.4 to 13.6 billion years. Since the main goal in dating the oldest clusters is to establish a lower limit on the age of the Universe, the 95% confidence limit is more relevant because of the presence of possible systematic errors present. This lower limit for the ages of globular clusters increases from 10.2 to 10.8 Gyr. For the age of the Universe, the formation time of the oldest clusters must be added. Estimates of formation time vary between 1 and 2 Gyr but a conservative lower limit is 0.8 Gyr [Kra03]. This estimate is largely independent of cosmological model. This puts the lower limit (95% confidence level) for the age Universe at approximately 11.6 Gyr.

Various cosmological models exist and their age predictions vary widely but there are four standard parameters that define the geometry of the Universe. These include the fraction of energy contained in matter (Ω_m) and in vacuum energy (Ω_Λ) *today*, the dark energy equation of state parameter (w) and the present rate of expansion as measured by the Hubble constant (H_o). The age of the Universe at any time (τ_o), with a redshift (z_o), is [Kra03]:

$$\tau_o = \frac{1}{H_o}\int_{z_o}^{\infty} \frac{1}{(1+z)\cdot\sqrt{\Omega_m\cdot(1+z)^3+\Omega_\Lambda\cdot(1+z)^{3(1+w)}}}\,dz \qquad \text{Equation 5-5}$$

The best constrained parameter is the present expansion of the Universe, and the latest Hubble Key Project estimate for H_o is 71(7) $km\cdot s^{-1}\cdot Mpc^{-1}$ [Fre00]. Presently, the other three parameters are less constrained. To produce an accelerating Universe, w must be < -0.3 which is supported by supernovae observation [Fre00]. Furthermore, the Wilkinson Microwave Anisotropy Probe (WMAP) concludes w is less than -0.78 at the 95% confidence level [Spe03]. Recent analyses of type Ia supernovae suggest that $\Omega_\Lambda = 0.7$ [Pen99] and most cosmological

models assume the further constraint of a flat Universe: $\Omega_m + \Omega_\Lambda = 1$. This is also supported by WMAP which suggests that the total critical matter density is 1.02(2).

The most important impact of new globular cluster age estimates is to further constrain these parameters. The historically preferred cosmological model assumed a flat Universe with $\Omega_m=1$. This predicts a present day age of 9.3 Gy; assuming a 2σ error on the Hubble constant the age rises to 11.6 Gy. Both of these possibilities are ruled out at the 95% confidence level by the new lower limit from globular clusters[24]. This is a profound conclusion that strongly supports the presence of a non-zero cosmological constant. Although this is not a novel conclusion, it is entirely independent from other evidence.

With the present uncertainties in globular cluster age dating, the constraints on other models are not as stringent. For a model supported by the supernovae analysis, with $\Omega_\Lambda = 0.7$ and the present Hubble constant, w must be less than -0.75 at the 90% confidence level. If one only assumes a flat Universe and the present Hubble constant, the two dimensional parameter space of w and Ω_m can be partitioned into regions compatible with the present globular cluster age limits [Kra03].

[24] i.e. if the values were not rounded.

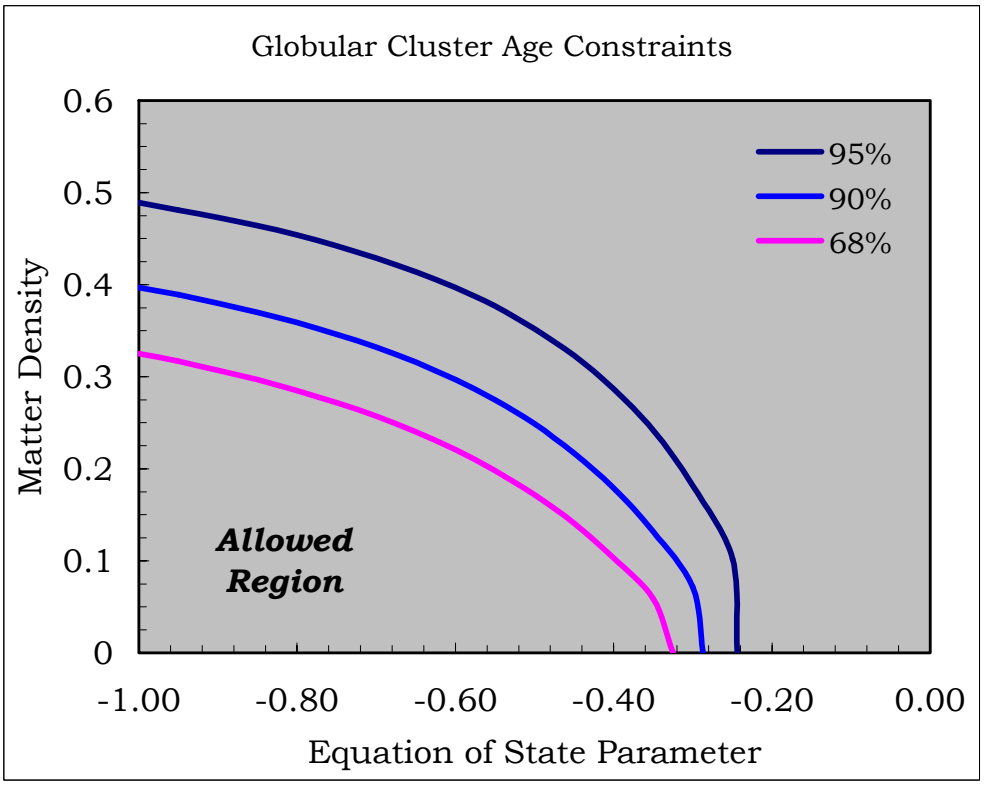

Figure 5-9: Cosmological parameter constraints

Figure adapted from [Kra03] but calculated with the new $^{14}N(p,\gamma)^{15}O$ reaction rates. The allowed region is a significantly smaller parameter space.

5.4 Conclusions

We measured the $^{14}N(p,\gamma)^{15}O$ S-factor for all states that contribute significantly in the low energy region. The new data extend to lower energies than any previous work that measured individual transitions. Our experimental data are largely consistent with past measurements. In contrast, by extending the experimental data to lower energies, we reached significantly different conclusions about the cross section at astrophysical energies.

Our new result gives a $S_{tot}(0)$ value that is 43% of the previously accepted value. This change is more than a 3σ lower from the NACRE recommended value. The lower value almost entirely results from new constraints placed on the ground state extrapolation. Our data support a minimal contribution from direct capture and the -504 keV sub-threshold resonance at low energies in the ground state transition. At the time of this writing, there are new experiments being performed by at least two groups (LENA and LUNA) that will push measurements to even lower energies. However, these experiments are designed to measure the *total* S-factor and the results here will continue to help provide a consistency check for any new data.

For most main-sequence stars, the S-factor is approximately constant and equal to $S_{tot}(0)$. This implies that the $^{14}N(p,\gamma)^{15}O$ reaction rate is reduced by 43%. In turn, our new reaction rate significantly slows the rate of core hydrogen burning in massive main sequence stars (although not by 43%). Hydrogen shell burning in smaller stars moving off the main-sequence is also slower than previously thought. The main-sequence track of a $0.8 \cdot M_{sun}$ star demonstrated one consequence of this new rate.

In the case of the oldest globular clusters, their age estimates increase by approximately 1.2 Gy. With the increased lower limit on the age of the Universe proposed here, a flat, matter dominated Universe is almost certainly ruled out. Consequently, our results provide stronger evidence for a large cosmological constant than previous age estimates.

REFERENCES

[Adl98] E. Adelberger et al., Reviews of Modern Physics, **70**, 1267 (1998).

[AjS81] F. Ajzenberg-Selove, Nuclear Physics, **A360**, 1 (1981).

[AjS91] F. Ajzenberg-Selove, Nuclear Physics, **A523**, 1 (1991).

[Ang99] C. Angulo et al., Nuclear Physics, **A656**, 3 (1999).

[Ang01] C. Angulo and P. Descouvemont, Nuclear Physics, **A690**, 755 (2001).

[Bec82] H. Becker et al., Zeitschrift für Physik A – Atoms and Nuclei, **305**, 319 (1982).

[Bec95] H. Becker et al., Zeitschrift für Physik A – Atoms and Nuclei, **351**, 453 (1995).

[Ber01] P. Bertone et al., Physical Review Letters, **87**, 15 (2001).

[Ber02] P. Bertone and A. Champagne, Physical Review, **C66**, 804 (2002).

[Bet38] H. Bethe, Physical Review, **55**, 434 (1939).

[Bev92] P. Bevington, Data Reduction and Error Analysis for the Physical Sciences, McGraw-Hill, 1992.

[Bis77] M. Bister, A. Anttila, and J Keinonen, Physical Review, **C16**, 1303 (1977).

[Bur57] E. Burdbidge, G. Burbidge, W. Fowler, F. Hoyle, Reviews of Modern Physics, **29**, 547 (1957).

[Cha03] A. Champange, private communication, (2003).

[Chb96] B. Chaboyer et al., Science, **271**, 957 (1996).

[Cla83] D.D. Clayton, Principles of Stellar Evolution and Nucleosynthesis, University of Chicago Press, 1983.

[Dal91] G. B. Dalrymple, The Age of the Earth, Stanford University Press, 1991.

[Deb88] K. Debertin and R. Helmer, Gamma- and X-ray Sprectroscopy with Semiconductor Detectors, North Holland, 1988.

[Dun51] D. Duncan and J. Perry, Physical Review, **82**, 809 (1971).

[Fer65] A. Ferguson, Angular Correlation Methods In Gamma-ray Spectroscopy, North-Holland Amsterdam, 1965.

[Fre00] W. Freedman, Physics Reports, **333**, 13 (2000).

[Fre02] R. Freedman and W. Kaufmann III, Universe, W. Freeman and Company, 2002.

[Gra97] R. Gratton et al., Astrophysical Journal, **491**, 749 (1997).

[Gov59] H. Gove, Nuclear Reactions 1, edited by P. Endt and M. Demeur (1959).

[Han99] M. Hannam and W. Thompson, Nuclear Instruments and Methods, **A431**, 239 (1999).

[Has94] C. Hansen and S. Kawaler, Stellar Interiors, Springer, 1994.

[Jen50] B. Jennings, K. Sun, and H. Leiter, Physical Review, **80**, 109 (1950).

[Kei79] J. Keinonen and A. Anttila, Nuclear Instruments and Methods, **160**, 211 (1979).

[Kim03] I. Kim, C. Park, and H. Choi, Applied Radiation and Isotopes, **58**, 227 (2003).

[Kra00] L. Krauss, Physics Reports, **333**, 33 (2000).

[Kra03] L. Krauss and B. Chaboyer, Science, **299**, 65 (2003).

[Lam57] W. Lamb and R. Hester, Physical Review, **108**, 1304 (1957).

[Lan58] A. Lane and R. Thomas, Reviews of Modern Physics **30**, 257 (1958).

[Lon03] R. Longland, private communication, 2003.

[Muk03] A. Mukhamedzhanov et al., submitted for publication, (2003).

[Nel01] S. Nelson et al., Bulletin of the American Physical Society, **46**, 64 (2001).

[Pen99] C. Pennypacker et al., Astrophysical Journal, **517**, 565 (1999).

[Pix57] R. Pixley, thesis, California Institute of Technology, (1957).

[Pow98] D. Powell et al., Nuclear Physics, **A644**, 263, (1998).

[Rol73] C. Rolfs, Nuclear Physics, **A217**, 29 (1973).

[Rol74] C. Rolfs and R. Azuma, Nuclear Physics, **A227**, 291 (1974).

[Rol88] C. Rolfs and W. Rodney, Cauldrons in the Cosmos, University of Chicago Press, 1988.

[Ros67] H. Rose and D. Brink, Reviews of Modern Physics, **39**, 306 (1967).

[Row02] C. Rowland et al., Nuclear Instruments and Methods, **A480**, 610 (2002).

[Sch87] U. Schröder et al., Nuclear Physics, **A467**, 240 (1987).

[Seu87] S. Seuthe et a., Nuclear Instruments and Methods, **A260**, 33 (1987).

[Sha54] W. Sharp et al., The Quantum Theory of Angular Momentum, Atomic Energy of Canada Limited, AECL-97 (Unpublished), 1954.

[Spe03] D. Spergel et al., submitted to the Astrophysical Journal, 2003.

[Tom63] T. Tombrello and P.Parker, Physical Review, **131**, 2582 (1963).

[Tho03] W. Thompson and C. Iliadis, private communication, 2003.

[Uhr85] M. Uhrmacher et al., Nuclear Instruments and Methods, **B9**, 234 (1985).

[Zie00] J. Ziegler and J. Biersack, program SRIM2000, 2000 (unpublished).